Alma Mater Studiorum - Università di Bologna

Scuola di Scienze
Dipartimento di Fisica e Astronomia
Corso di Laurea Magistrale in Astrofisica e Cosmologia

A LOFAR view of three HETDEX galaxy clusters: radio halos and their connection with X-ray emitting thermal gas

Tesi di Laurea Magistrale

Presentata da:
Cristina Nanci

Relatore:
Prof. Daniele Dallacasa

Co-relatori:
Dott. Gianfranco Brunetti
Dott. Andrea Botteon

Sessione III
Anno Accademico 2018-2019

This Thesis work was done as part of the research activity of the Istituto di Radioastronomia - Istituto Nazionale di Astrofisica (INAF) in Bologna.

Contents

Abstract **1**

Sommario **3**

1 Galaxy clusters **5**
1.1 Components of galaxy clusters . . . 5
1.1.1 Galaxies . . . 5
1.1.2 Intra-cluster medium . . . 8
1.1.3 Dark matter . . . 12
1.2 Mass estimation . . . 12
1.3 Scaling relations . . . 13
1.4 Formation and evolution . . . 15
1.5 Cool-core and merging clusters . . . 16
1.5.1 Cool-core clusters . . . 17
1.5.2 Merging clusters . . . 17

2 Non-thermal emission from galaxy clusters **19**
2.1 Radio Galaxies . . . 24
2.2 Diffuse radio emission from galaxy clusters . . . 25
2.2.1 Radio Halos . . . 25
2.2.2 Radio Relics . . . 30
2.2.3 Mini halos . . . 32
2.3 The importance of low frequency radio observation . . . 33

3 The LOFAR era **37**
3.1 The LOw-Frequency ARray . . . 37
3.1.1 System overview . . . 37
3.2 The LOFAR Two-metre Sky Survey . . . 40

4 Data analysis **45**
4.1 LOFAR data . . . 45
4.2 VLA data . . . 51
4.3 Chandra data . . . 52

5 Targets selection and analysis of radio and X-ray observations **55**
5.1 Targets selection . . . 55
5.2 Abell 1550 . . . 56
5.2.1 Radio data analysis . . . 57
5.2.2 X-ray data analysis . . . 62
5.3 RXC J1115.2+5320 . . . 64
5.3.1 Radio analysis . . . 65

5.3.2 X-ray analysis . . . 67
5.4 Abell 1622 . . . 68
5.4.1 Radio analysis . . . 69
5.4.2 X-ray analysis . . . 69

6 Connection between thermal and non-thermal plasma in galaxy clusters 75
6.1 Point to Point analysis . . . 75
6.2 Cluster dynamical state-RH connection . . . 80
6.2.1 Morphological parameters . . . 80
6.2.2 RH scaling relations . . . 81
6.3 The head-tail confinement . . . 84

7 Conclusions 89

Bibliography 91

Abstract

A growing number of galaxy clusters are found to host large-scale synchrotron emission in the form of radio halos. These sources provide the evidence of non-thermal components, consisting of relativistic particles and magnetic fields, permeating the whole volume of the galaxy clusters. According to the currently accepted scenario the emitting particles are (re-)accelerated in the cluster magnetic fields during cluster merger events. One of the most important evidence supporting this scenario is the fact that indeed radio halo are typically found in dynamically active systems.

The study of the connection between the cluster dynamics and the properties of radio halos is one of the most important approaches to constrain the origin and evolution of relativistic particles in galaxy clusters. This is the approach that we follow in the Thesis. Furthermore we use low-frequency data from the new generation radio telescope LOFAR. These observations have a much better sensitivity to the cluster-scale radio emission than other existing radio interferometers, and allow to enter uncharted territories in this research area.

More specifically, in this Thesis, we analyzed radio and X-ray data of three SZ-selected galaxy clusters: Abell 1550, RXC J1115.2+5320 and Abell 1622. These are part of the HETDEX field in the LOFAR LoTSS survey at 144 MHz. The last two targets were never studied in the radio band. Abell 1550 was already studied using observations at 1.4 GHz (Govoni et al. 2012) and was already known to host a radio halo. By combining VLA and LOFAR data we measured a very steep spectrum of the radio halo supporting turbulent re-acceleration for the radio emitting electrons. We discovered a radio halo in RXC J1115.2+5320, while no diffuse emission is detected in Abell 1622 by our LOFAR observations. For Abell 1622, that is the smaller cluster in our sample, we derived a upper limit to its flux density and radio luminosity and demonstrate that the cluster is underluminous in radio. We suggest that this is due to the smaller energy budget available to particles re-acceleration in less massive systems like Abell 1622.

We studied the connection between thermal (X-rays) and non-thermal (radio) properties in our clusters. Specifically we:

- explore the dynamics of our targets measuring dynamical parameters;
- investigate on the behaviour of these clusters in the correlations between radio luminosity and mass (or X-ray luminosity);
- derive point-to-point radio brightness - X-ray brightness correlations for the radio halos in Abell 1550 and RXC J1115.2+5320.

All these findings are discussed in the context of current theoretical models.

Finally we discover a long head tail radio galaxy in Abell 1622 and discuss the interplay between the relativistic plasma and the surrounding intra-cluster medium.

The Thesis is organised in the following Chapters:

- In Chapter 1 we discuss the thermal properties and the formation/evolution of galaxy clusters;

- In Chapter 2 we illustrate the properties of non-thermal emission from galaxy clusters highlighting the importance of its study in the low-frequencies of the radio band;
- In Chapter 3 we present the new generation interferometer with which the observations analysed in this Thesis work have been performed;
- Chapter 4 describes the procedures followed in the radio and X-ray data analysis;
- In Chapter 5 we present the targets and the results of the procedures outlined in the previous Chapter;
- In Chapter 6 we explore the connection between thermal and non-thermal emission in our clusters and discuss the findings in the light of the other results found in the literature;
- Chapter 7 summarizes the main results of the Thesis work.

Sommario

Un numero sempre crescente di ammassi di galassie mostra emissione di sincrotrone diffusa sotto forma di aloni radio. Queste sorgenti testimoniano la presenza di componenti non-termiche di particelle relativistiche e campi magnetici all'interno degli ammassi di galassie. Secondo lo scenario attualmente più accreditato, le particelle emittenti sono (ri-)accelerate dai campi magnetici interni all'ammasso durante gli eventi di merger tra ammassi. Una delle prove fondamentali a supporto di questo scenario è il fatto che gli aloni radio si osservano tipicamente in sistemi dinamicamente attivi. Lo studio della connessione tra la dinamica dell'ammasso e le proprietà degli aloni radio è uno degli approcci più importanti per vincolare i modelli sull'origine e l'evoluzione delle particelle relativistiche negli ammassi di galassie. Questo è anche l'approccio che seguiamo in questa Tesi. Inoltre analizziamo i dati a bassa frequenza ottenuti dal radio telescopio di nuova generazione LOFAR. Queste osservazioni hanno il vantaggio di essere attualmente le più sensibili alle scale dell'emissione radio degli ammassi rispetto agli altri interferometri esistenti e consentono quindi di entrare in territori ancora inesplorati in quest'area di ricerca.

In particolare, abbiamo analizzato i dati in banda radio e X di tre ammassi di galassie selezionati dal catalogo Planck-SZ e osservati all'interno dell'HETDEX field della survey LoTSS condotta a 144 MHz: Abell 1550, RXC J1115.2+5320 e Abell 1622. Gli ultimi due target non sono mai stati studiati nella banda radio fino ad ora. Abell 1550 era già stato studiato usando osservazioni a 1.4 GHz (Govoni et al. 2012) ed era già noto ospitare un alone radio al suo interno. Dalla combinazione dei dati VLA e LOFAR abbiamo trovato che l'alone è caratterizzato da uno spettro molto ripido, tale risultato supporta l'ipotesi di accelerazione turbolenta degli elettroni radio-emittenti. Abbiamo scoperto un alone radio in RXC J1115.2+5320, mentre nessuna emissione diffusa è stata rilevata in Abell 1622 dalle nostre osservazioni LOFAR. Per Abell 1622, l'ammasso più piccolo del nostro campione, abbiamo derivato un limite superiore per la sua potenza radio scoprendo che l'ammasso risulta sotto-luminoso in banda radio. Suggeriamo che questo sia dovuto al minore budget energetico disponibile per la ri-accelerazione delle particelle nei sistemi meno massivi come Abell 1622.

Abbiamo studiato la connessione tra le proprietà termiche (X) e non-termiche (radio) nei nostri ammassi. Nello specifico:

- determiniamo lo stato dinamico dei nostri target misurando i parametri dinamici;
- indaghiamo sul comportamento di questi ammassi nelle correlazioni tra luminosità radio e massa (o luminosità X);
- deriviamo le correlazioni point-to-point tra la luminosità radio e X per gli aloni radio in Abell 1550 e RXC J1115.2+5320.

Tutti questi risultati sono discussi nel contesto degli attuali modelli teorici.

Infine abbiamo scoperto una radio galassia di tipo long head tail in Abell 1622, ne discutiamo l'interazione tra il plasma relativistico e il mezzo intra-cluster circostante.

La Tesi è organizzata nei seguenti Capitoli:

- Nel Capitolo 1 discutiamo le proprietà termiche e la formazione/evoluzione degli ammassi di galassie;
- Nel Capitolo 2 illustriamo le proprietà dell'emissione non-termica dagli ammassi di galassie evidenziando l'importanza del suo studio nella banda radio a basse frequenze;
- Nel Capitolo 3 presentiamo l'interferometro di nuova generazione con cui le osservazioni analizzate in questo lavoro di Tesi sono state condotte;
- Il Capitolo 4 descrive le procedure seguite nell'analisi dei dati X e radio;
- Nel Capitolo 5 presentiamo i target e i risultati delle procedure delineate nel Capitolo precedente;
- Nel Capitolo 6 descriviamo i metodi di indagine sulla connessione tra il gas termico e le componenti non termiche negli ammassi di galassie e discutiamo i risultati ottenuti per i nostri target;
- Il Capitolo 7 riassume i risultati principali di questo lavoro di Tesi.

Chapter 1

Galaxy clusters

Clusters of galaxies (GCs) are regions of matter overdensity in the intersections of the filamentary structure of the *cosmic web*, that is the way in which matter in Universe is organized (Figure 1.1). The typical scales on which GCs extend within the cosmic network are of the order of 1-3 Mpc. With such dimensions and masses of 10^{14} to above 10^{15} $M_{\odot}$, GCs are the largest virialised objects in the present Universe.

GCs host from hundreds to thousands of galaxies, which however represent only $\sim 5\%$ of the total mass. The main component ($\sim 80\%$) is the dark matter (DM), followed by the Intra-Cluster Medium (ICM, $\sim 15\%$), that is a tenuous and hot thermal gas which permeates the whole cluster volume (e.g. Sarazin 1986 for a review).

According to the current hierarchical model, the cosmic structures proceed to form via matter aggregation under the action of the gravitational force. The final large systems of galaxies, gas and dark matter bounded together are the result of consecutive minor and major mergers between smaller objects, like groups, galaxies and small clusters. In this so-called *bottom-up* scenario, GCs represent an unique tool to constrain the cosmological models (e.g. Borgani & Kravtsov 2011). They are also extraordinary astrophysical laboratories to study the interplay between the ICM and the galaxies, and the feedback mechanisms that regulate the evolution of the ICM and of AGN. Finally the study of the interplay of the cluster dynamics (and evolution) with the properties of the ICM and of the non-thermal components (magnetic fields and relativistic plasma) in GCs provides fundamental inputs on the way in which energy flows from large (cosmological) scales to smaller (astrophysical plasma) scales.

1.1 Components of galaxy clusters

Observing GCs at different wavelengths reveals the properties of their different components (Figure 1.2). Because of their galaxies component, GCs have been initially identified in the optical band. GCs were indeed first classified in a wide catalog created by George Abell in 1958 who inspected a photographic survey made with the Schmidt telescope at Mount Palomar in the 1950s. Due to its temperature ($T \sim 10^7 - 10^8$ K) and density ($n_{gas} \sim 10^{-4} - 10^{-2}\,\mathrm{cm}^{-3}$), the ICM emits in the X-rays via thermal bremsstrahlung radiation. For this reason GCs are bright X-ray sources. However the most significant component of the cluster, constituted by DM, can be studied only by its gravitational effect.

1.1.1 Galaxies

Galaxies and stars within them are mostly studied through optical and infrared (IR) observations. Galaxies spectra is made up of a continuum component, due to the black body radiation

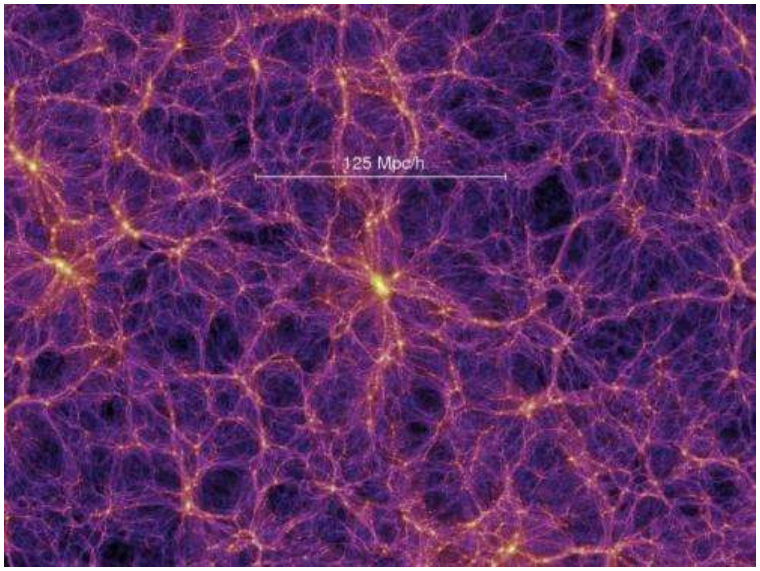

Figure 1.1: Frame of the cosmic web as simulated by the Millenium Simulation (Springel et al. 2005). The zoom of the density field is taken at z=0 (t=13.6 Gyr).

and radiative recombination processes, and emission lines, produced via radiative decay processes. From the emission lines it is possible to derive the redshifts of the hosting structure and to measure the dispersion of galaxies radial velocity, σ_v. Being determined by whole cluster dynamics, the velocity dispersion gives an estimate of the time needed to cross it, t_{cross}:

$$t_{cross} = \frac{D}{\sigma_v}$$

where D is the cluster dimension. With typical values of $\sigma_v \sim 1000\,\mathrm{km/s}$ and $D \sim$ Mpc, the crossing time is of the order of 1 Gyr, resulting significantly shorter than a Hubble time ($t_H \sim$ 13.7 Gyr). This is a proof that GCs had enough time to reach a dynamically relaxed state.

At the center of rich GCs it is often found a supergiant elliptical galaxy which represent the brightest galaxy of the cluster (BCG). These kind of objects are among the most luminous galaxies in the Universe. Some BCGs show features of ongoing star formation (e.g. inferred from IR observations by O'Dea et al. 2008) and they host radio-loud active galactic nucleus (AGN) more frequently than galaxies of similar stellar masses (Best et al. 2007).

Most of BCGs correspond to the *central dominant* galaxy (cD), a special class of galaxies characterized by the presence of two or more nuclei in the core and a diffuse low-surface brightness stellar envelope extended up to several hundred of kpc around the nucleus (Oemler 1973). All the BCGs properties are due to the complex mechanisms involved in their formation and evolution, which differ from the one of the ordinary elliptical galaxies (De Lucia & Blaizot 2007).

BCGs are indeed the result of the combination of dynamical processes (Lin & Mohr 2004): (1) *galactic cannibalism*, in which cluster galaxies move toward the cluster center because of dynamical friction, they merge and grow in mass and luminosity encompassing other incoming galaxies and smaller bodies (Ostriker & Hausman 1977) and (2) stripping of stars from galaxies which occurs in *galaxy harassment*, the phenomenon of high speed encounters between cluster substructures (Moore et al. 1996): stripped stars are likely embedded in the cD halo.

In general galaxies in the clusters interact with the ICM and this affects their evolution and properties. The interplay between spiral galaxies and the GC environment and dynamical state is reflected in the inter-stellar medium (ISM) morphology and in the high star formation rates. Especially those galaxies moving near the central (and denser) parts of the cluster are affected

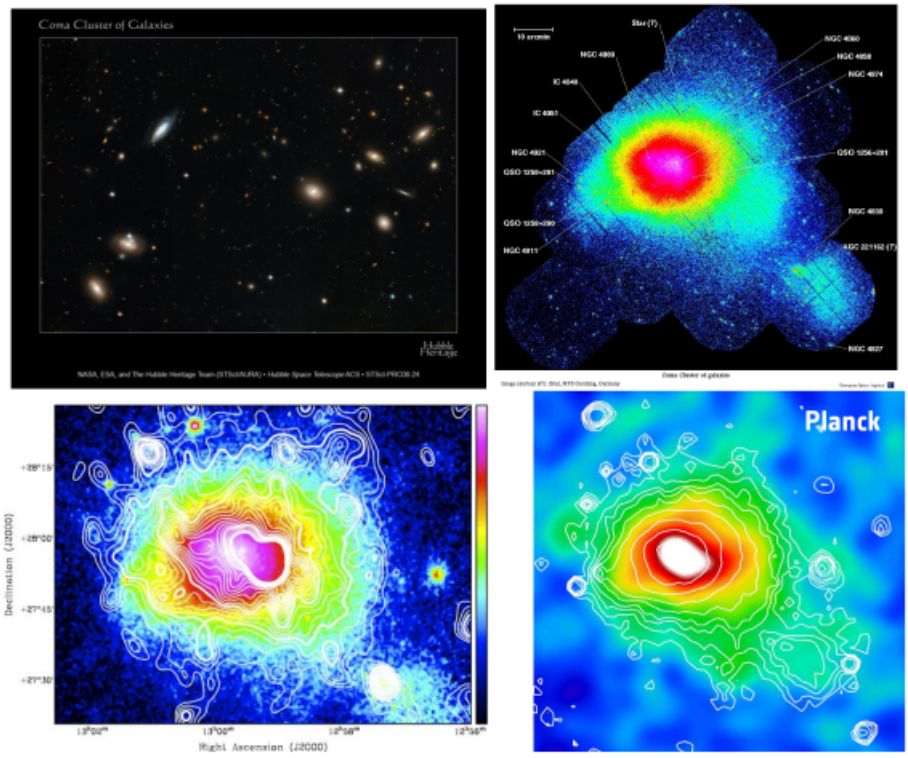

Figure 1.2: Multi-frequency view of Coma cluster. *Top left*: Optical image from of the galaxies within the cluster (from Hubble space telescope, HST). *Top right*: X-ray emission from thermal ICM (Briel et al. 2001). *Bottom left*: Radio contours (352 MHz band) of the diffuse emission over-plotted on the X-ray image (Shea Brown & Lawrence Rudnick 2011). *Bottom right*: X-ray contours overlaid on the SZ signal (Planck Collaboration et al. 2011).

by gas deficiency in the disks due to the ICM dynamical effects on the ISM (ram-pressure stripping, *strangulation*, *evaporation*, see Mihos 2004 for a review). Evidences are seen through HI observations (Davies & Lewis 1973),

These dynamic processes in act in central region of clusters are reflected in the way in which different galaxies type are found, depending on the density of the environment. A close correlation is observed between the cluster projected density and the fraction of early-type (ellipticals, E and lenticulars, S0) and late-type (spirals, S, and irregulars, I) galaxies. As shown in Figure 1.3, the fraction of E and S0 galaxies increases with projected density, while an opposite behavior is observed in the fraction of S and I galaxies which decreases with density.

In GCs, the brightness is dominated by early-type galaxies showing an intrinsic difference from the galaxy population observed in the field. Within GC, the late-type galaxies are more numerous, but fainter, while the early-type galaxies are less abundant, but brighter (Sarazin 1986).

Galaxies luminosity function

A reliable approximation of the galaxy luminosity distribution inside the cluster has been proposed by Schechter 1976. The function provides the number of galaxies per unit volume $\varphi(L)dL$ with luminosity between L and $L + dL$:

$$\varphi(L)dL = \varphi^*(L/L^*)^{-\alpha} \exp(L/L^*)d(L/L^*)$$

where φ^* is the normalization (a galaxy number in unit volume); α is the dimensionless

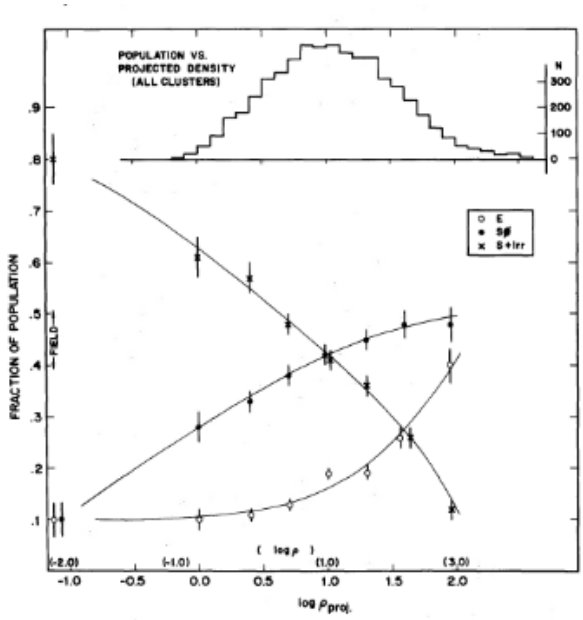

Figure 1.3: Correlation between cluster projected density, in unit of galaxies Mpc^{-2}, and the different galaxies type (Dressler 1980).

parameter which determines the slope of the power-law in the range of $L \ll L^*$; and L^* is the characteristic luminosity, which can be equivalently expressed with the characteristic absolute magnitude. The luminosity function shows an exponential cut-off for $L > L^*$. The values of φ^*, L^* and α, are determined from observations. The Schechter analytic expression for the galaxy luminosity function well reproduces observational data.

1.1.2 Intra-cluster medium

About 75% of the baryonic matter in GCs is in the form of an hot, optically thin, ionized plasma: the intra-cluster medium. With typical mean density of $\sim 10^{-2} - 10^{-4}$ cm^{-3} and temperature of $\sim 10^7 - 10^8$ K ($\sim$ 1-10 keV), the ICM emits mainly via bremsstrahlung in the X-ray band. Since clusters reach X-ray luminosities up to $\sim 10^{44} - 10^{45}$ erg/s thanks to their ICM content, one of the most direct and simple way to detect GCs is carrying out X-ray surveys.

Due to the free-free emission mechanism, an ion of charge Z in a plasma with an electron temperature T_e, radiates a total monochromatic power per unit volume given by (Rybicki & Lightman 1986):

$$\varepsilon_\nu \equiv \frac{dL}{dV\,d\nu} \propto Z^2 n_e n_i G_{ff}(Z, T_e, \nu) T_e^{-1/2} \exp(-h\nu/k_B T_e) \tag{1.1}$$

where n_e and n_i are the number density of electrons and ions, respectively, and $G_{ff} \propto \ln(k_B T_e/h\nu)$, the Gaunt factor, provides corrections related to quantum effects; k_B is the Boltzmann constant and h is the Planck constant. The spectrum normalization gives a measure of n_e, while from the exponential cut-off can be inferred the ICM temperature.

Coulomb collisions between electrons and protons in the ICM occur on time-scale of $\sim$ Myr, due to their mean free path in a medium with such temperature and density. This time-scale is lower than the age of the plasma, therefore the particles can reach the kinetic equilibrium and the ICM temperature can be referred as a global value in common between ions and electrons, $T_e = T_i = T$.

According to the hypothesis of dynamical equilibrium, the cluster gravitational potential acts simultaneously on both ICM and galaxies, entailing that the same dynamics characterizes the two components. This implies that the kinetic energy of galaxies is similar to the gas thermal energy, i.e.:

$$k_B T \sim \mu m_p \sigma_v^2 \tag{1.2}$$

where m_p is the proton mass and μ is the *mean molecular weight* ($\mu \sim 0.6$ in the ICM). Over the years, estimation of the temperature through X-ray observations and optical measures of the velocity dispersion, well tested the σ-T relation (Girardi et al. 1996), ensuring that the scenario of dynamical equilibrium is a good assumption for the ICM.

As a further consequence, the spatial distribution of gas follows a profile similar to that of galaxies. It was investigated by Cavaliere & Fusco-Femiano 1976 who assumed both gas and galaxies in isothermal and in hydrostatic equilibrium under the gravitational potential Φ.

The condition of hydrostatic equilibrium implies a balance between pressure gradients and gravity:

$$\bigtriangledown p = -\rho \bigtriangledown \Phi \tag{1.3}$$

where p and ρ are pressure and density of the medium, respectively. In the ICM gas, these quantities are linked by the equation of state for ideal gas, $p_{gas} = \rho_{gas} k_B T / \mu m_p$. The thermal equilibrium hypothesis implies that the temperature is constant. Assuming a spherically symmetric and locally homogeneous distribution, the Eq. (1.3) referred to the gas can be expressed as:

$$\frac{d \ln \rho_{gas}}{dr} = -\frac{\mu m_p}{k_B T} \frac{d\Phi}{dr}.$$

Similarly the galaxies distribution is obtained by replacing $k_B T / \mu m_p$ with σ_v^2 and assuming that this is isotropic:

$$\frac{d \ln \rho_{gal}}{dr} = -\frac{1}{\sigma_v^2} \frac{d\Phi}{dr}.$$

The relation between gas and galaxies distribution can be derived from above equations:

$$\frac{d \ln \rho_{gas}}{dr} = -\frac{\mu m_p \sigma_v^2}{k_B T} \frac{d \ln \rho_{gal}}{dr} \Rightarrow \rho_{gas} \propto \rho_{gal}^{\beta} \tag{1.4}$$

where the β parameter represents the ratio of the specific kinetic energy of galaxies and the specific thermal energy of gas

$$\beta \equiv \frac{\mu m_p \sigma_v^2}{kT}.$$

Adopting the King approximation to the isothermal sphere (King 1962) for the galaxies distribution and following Eq. (1.4), the density profiles are:

$$\rho_{gal}(r) = \rho_{gal,0} \left[1 + \left(\frac{r}{r_c} \right)^2 \right]^{-3/2};$$

$$\rho_{gas}(r) = \rho_{gas,0} \left[1 + \left(\frac{r}{r_c} \right)^2 \right]^{-3\beta/2} \tag{1.5}$$

where $\rho_{gas,0}$ and $\rho_{gal,0}$ are the central densities and r_c measures the radius within which the density is half that central one. The gas density distribution defined is the so-called *β-model* and it is adopted to fit the X-ray surface brightness, described in the form:

$$I(r) = I_0 \left[1 + \left(\frac{r}{r_c}\right)^2\right]^{1/2-3\beta}.$$

The distribution of the gas can be inferred directly from the X-ray imaging. Assuming a spherical shape of the cluster, the X-ray surface brightness at frequency ν at projected radius b is:

$$\Sigma_\nu(b) = 2\int_{b^2}^{\infty} \frac{\varepsilon_\nu(r)dr^2}{\sqrt{r^2 - b^2}}. \tag{1.6}$$

Due to the symmetry of the problem, it is possible to Abel-invert the Eq. (1.6) and get the emissivity along r at frequency ν:

$$\varepsilon_\nu(r) = -\frac{1}{2\pi r}\frac{d}{dr}\int_{b^2}^{\infty} \frac{\Sigma_\nu(b)dr^2}{\sqrt{r^2 - b^2}}.$$

As seen above, $\varepsilon_\nu \propto n_e n_i \sim n_e^2$ (the plasma is neutral then $n_e \sim n_i$[1].) so the electron density can be deduced.

The value of β, estimated from the surface brightness fitting, is ~ 0.65 (C. Jones & Forman 1984) but this results inconsistent with the hypothesis of the Eq. (1.2), instead confirmed by X-ray and optical spectroscopic measurements of gas temperature and velocity dispersion. This discrepancy is due to the oversimplified assumptions underlying the β-model interpretation. Moreover, although the β-model is commonly used (Vikhlinin et al. 1999), a large fraction of the GC population in the Universe show cool-cores that form due to the enhanced radiative losses in the ICM in the center (see Section 1.5.1).

Through the X-ray spectral analysis it is possible to infer the chemical composition of the ICM gas. This reveals that the heavy elements fraction is a third of the solar one. Spectral lines of highly ionized metals, such as Fe, C, O, Ne, Si, S, have been detected in the ICM. Such significant abundances indicate a galactic origin of the elements, since the amount is too high to derive from a primordial gas. The typical metallicity profile has a peak in central regions and becomes constant in the outer regions, reaching a mean value of 0.3-0.4 solar abundance (see Mernier et al. 2018 for a review).

Sunyaev-Zel'dovich effect in the ICM plasma

The ICM can be detected also via the Sunyaev-Zel'dovich effect (SZE). The hot ICM electrons population interacts via inverse Compton (IC) scattering with the cosmic microwave background (CMB) photon field, permeating the clusters volume. The CMB emission represents the first light coming from early Universe since it was produced in the last scattering between matter and radiation (Penzias & Wilson 1965) and its signal is detected everywhere in the sky.

The interaction between CMB and ICM particles causes a distortion of the CMB spectrum, known as *Sunyaev-Zel'dovich effect* (SZE) (Sunyaev & Zeldovich 1972).

Since matter and radiation were in thermal equilibrium at the moment of the last scattering, the CMB is represented by a black-body spectrum with intensity:

[1]The accurate calculation, taking into account the mass fraction of hydrogen, helium, and metals and each different contribution to the pressure, gives $n_e \sim 1.2 n_i$

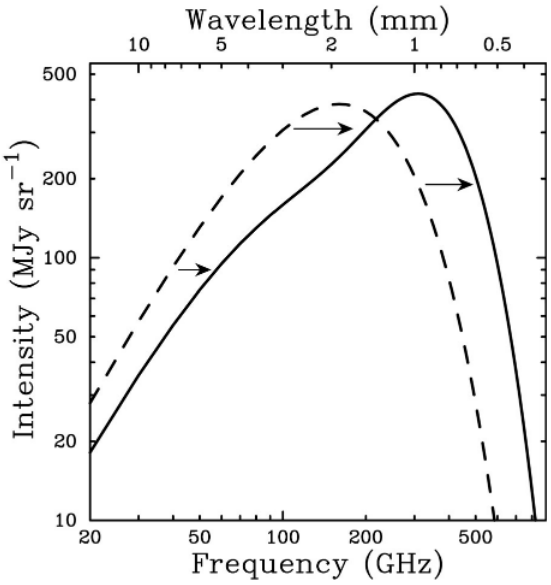

Figure 1.4: The CMB spectrum (dashed line) distorted by SZE (solid line). The distortion is emphatized: the observed effect is actual much smaller (Carlstrom et al. 2002). The SZE is detectable at frequencies ~ 218 GHz (~ 1.4 mm) in the millimeter band.

$$I_\nu = \frac{2h\nu^3}{c^2}\left[\exp\left(\frac{h\nu}{k_B T_{CMB}}\right) - 1\right]^{-1}$$

where $T_{CMB} = 2.725(1+z)$ K. In the interactions between CMB photons and ICM energetic electrons, the latter transfer energy to the cold photons, which consequently result more energetic and therefore blue-shifted. Hence, the SZE is seen as a small spectral distortion of the CMB radiation around 218 GHz: at lower frequencies the CMB intensity decreases due to the lack of weak photons that gained energy and populate the spectrum at higher frequencies. The total effect is shown in Figure 1.4.

The collisions with the hot thermal distribution of ICM electron, lead to a small change in CMB intensity:

$$\frac{\Delta I_{SZ}}{I_0} \propto y_e$$

where $I_0 = 2(k_B T_{CMB})^3/(hc)^2$ is the intensity unaltered by the effect and y_e is the Comptonization parameter, defined as:

$$y_e \propto \int n_e T_e dl$$

in which n_e and T_e are the density distribution and temperature of the electrons along the line-of-sight, respectively. In other terms, the y_e-parameter is a measure of the integrated electron pressure of the ICM along the line-of-sight. It depends only on physical characteristic of the plasma hence it does not decline with redshift. This remarkable feature of the SZE makes it a powerful tool to explore the high-redshift Universe. In the last few years increasingly improved measurements of SZE have given rise to ample catalogues of GCs, for example performed with the Atacama Cosmology Telescope (Hasselfield et al. 2013), and with the South Pole Telescope (Reichardt et al. 2013). In this Thesis it is discussed the study on three GCs selected from the Planck Collaboration survey (Planck Collaboration et al. 2014).

1.1.3 Dark matter

The measurements of GCs dynamical mass show a mass-to-light ratio (M/L) around 100 - 400, revealing that the largest amount of matter in GCs does not interact electromagnetically but it is in the form of dark matter. Non-baryonic matter content is indirectly inferred trough studies on the dynamics of galaxies and the lensing effect, mentioned later in this Chapter.

Baryonic matter in GCs is then surrounded by a DM envelope: the DM halo. The density profile widely adopted for these objects has a universal form, independent on the halo mass and on the cosmological framework:

$$\rho_{DM}(r) = \rho_{crit} \frac{\delta_c}{(r/r_s)(1 + r/r_s^2)}$$

where r_s and δ_c are characteristic scale radius and dimensionless density, which vary from halo to halo, and $\rho_{crit} = 3H^2/8\pi G$, is the critical density of the Universe, H is the Hubble constant. This so-called NFW profile have been derived by Navarro et al. 1997, by means of N-body simulations.

1.2 Mass estimation

GCs mass represents the key parameter to study how cosmic structures formed and evolved in the Universe. To find an unbiased estimation for this crucial parameter is not trivial and different independent methods can be used.

The historical and simplest one, designed by Zwicky 1937, is based on the assumption that the structure is in dynamical equilibrium so the virial theorem can be applied. It predicts that kinetic (T) and gravitational potential (U) energies are in equilibrium according to $2T + U = 0$. The dynamics of galaxies within the cluster are used to traces the potential well, the kinetic energy is:

$$T = \frac{1}{2} M_{tot} \sigma_v^2$$

where σ_v is the virial velocity dispersion of galaxies and M_{tot} the cluster total mass. The gravitational potential energy is given by:

$$U = -\frac{G M_{tot}^2}{r_g}$$

in which r_g is the gravitational radius, determined as:

$$r_g = 2 \left(\sum_i m_i \right)^2 \left(\sum_{i \neq j} \frac{m_i m_j}{r_{ij}} \right)^{-1}$$

where m_i is the mass of the i-th galaxy and r_{ij} is the separation between two galaxies. Therefore the total cluster mass is:

$$M_{tot} = \frac{r_g \sigma_r^2}{G}$$

derived by assuming spherical symmetry and an isotropic velocity distribution. The latter condition implies that $\sigma_v = 3\sigma_r$, where σ_r is the radial contribution to the velocity dispersion and it is inferred by observations.

The cluster total mass can be also measured by X-ray emission from the ICM. Under the hypothesis of hydrostatic equilibrium of Eq. (1.3) and spherical symmetry, it is:

$$\frac{dp}{dr} = -\rho_{gas}\frac{GM(r)}{r^2}$$

where $M(r)$ is the mass contained within the radius r. Using the equation of state of ideal gas, the mass is given by:

$$M(r) = -\frac{k_B T_{gas} r}{\mu m_p G}\left(\frac{d\ln\rho_{gas}}{d\ln r} + \frac{d\ln T_{gas}}{d\ln r}\right).$$

Consequently the mass can be measured by inferring the density profile and the temperature from X-ray observations analysis. For the gas density profile is commonly adopted a β-model, Eq. (1.5). The temperature profile can be built with performing the spectral analysis at different annuli and taking a temperature value for each of these. Alternatively the expression can be solved under the approximation of an isothermal gas.

Because of their huge mass, GCs act as gravitational lens, bending the light incoming from sources near or behind them. This effect, known as *gravitational lensing*, is one of the predictions of the theory of general relativity and is due to the influence of cluster gravitational field on the surrounding radiation. The effect impacts in different ways according to the geometry between the lensed object, the cluster and the observer. It can therefore be distinguished in *strong* or *weak* lensing, depending on the degree of deformation observed in the lensed source.

The objects seen through the lenses may show ring-shaped or arc-shaped morphologies and the study of these structures provides the third method to deduce the cluster mass and its distribution whitin the cluster volume (Bartelmann 2003). This approach is unrelated from assumptions of virial or hydrostatic equilibrium, which are often failing in merger systems, however it is challenging because of the difficulties in the detection of sources affected by lensing. Also, since the lensing effect include the total mass along the line of sight, some assumptions on the cluster shape must be introduced in order to deproject the lensing maps, leading then to further uncertainties in the mass estimation.

1.3 Scaling relations

As it will be outlined in the next section, the growth of cosmological structures occurs in a *self-similar* way since they are originated from scale-free density fluctuations (Kaiser 1986), and the phenomenon of gas accretion is driven by the gravity action only. In turn, since gravity does not have preferred scales, GCs of different masses and sizes are expected to be scaled version of each other. As a probe of this, scaling relations are found between the global properties of GCs, including temperature and mass.

The scaling relation between the cluster temperature T and mass M can be derived starting from the virial equilibrium, $3kT/2\mu m_p = GM/R$:

$$M \propto T^{3/2} \tag{1.7}$$

where M is the virial mass and it is defined as the mass contained in the virial radius R within which the mean density is equal to the virial *overdensity* (δ) times the critical density of the Universe, ρ_{crit}.

The integration over the cluster volume V of the ICM emissivity (1.1), gives the X-ray luminosity of the gas. It results then $\propto \rho^2 \Lambda V$, where ρ is the average gas density. The cooling function Λ for a gas cooling via bremsstrahlung mechanism is $\propto T^{1/2}$, so the X-luminosity becomes $L_X \propto \rho T^{1/2} M$. For the Eq. (1.7) this leads to the $L_X - T$ relation:

$$L_X \propto T^2. \tag{1.8}$$

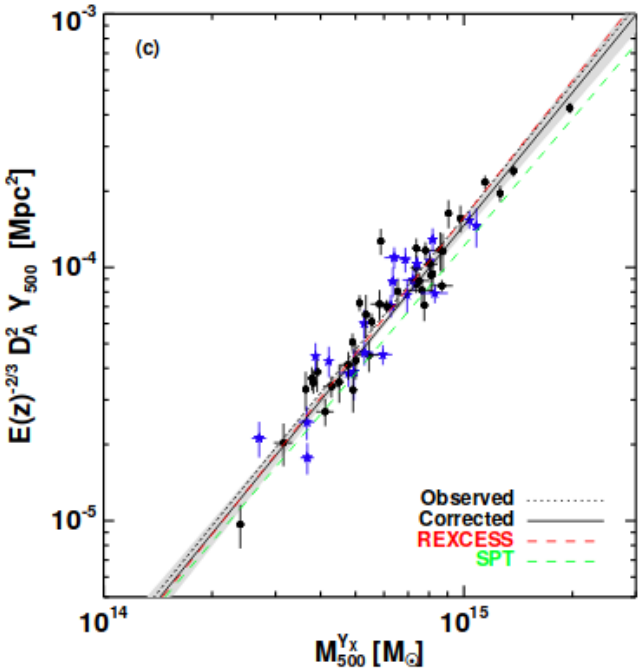

Figure 1.5: $Y_{500} - M_{500}$ scaling relation of the clusters sample from the Planck-XMM-Newton archive (Planck Collaboration et al. 2011).

The combination of the Eq. (1.7) and the Eq. (1.8) gives the scaling relation between the total mass and the luminosity of the cluster:

$$M \propto L_X^{3/4}. \tag{1.9}$$

Remarkably, the mass can be related to the *integrated y-parameter* of the SZE. This parameter represents a measure of the SZE flux (i.e. the CMB intensity drop caused by the effect, see Section 1.1.2) and it is define as:

$$Y = \int_\Omega y d\Omega \propto \frac{1}{D_A^2} \int_0^\infty dl \int_A n_e T dA$$

where Ω is the solid angle subtended by the cluster, A is its area in the sky plane and D_A its angular distance. Assumed isothermal conditions, it follows:

$$Y D_A^2 \propto T \int n_e dV = MT$$

and finally, according to Eq. (1.8) and the Eq. (1.9):

$$Y D_A^2 \propto M^{5/3}.$$

The cluster scaling relations as predicted from the theory, are observed in the X-ray and SZE measurements. For example in Figure 1.6 and Figure 1.5 are shown results from different studies on $L_X - T_X$, $M - T_X$ and $Y D_A^2 - M$ scaling relations.

Once calibrated with observations and simulations, these relations give a substantial support in testing the cosmological models, since they provide a proxy for the GCs total mass. Moreover they are an immediate alternative for the mass estimation compared to the not trivial method seen before (virial, hydrostatic, lensing).

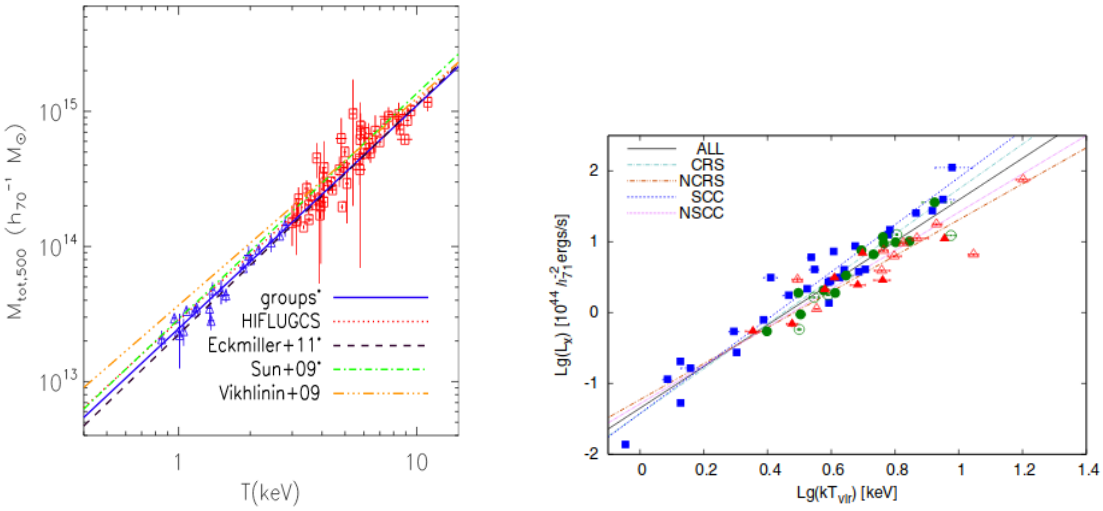

(a) (b)

Figure 1.6: Scaling relations tested on different samples of GCs. *Left*: $T_X - M_{500}$ relation from the works of Lovisari et al. 2015. *Right*: $L_X - T_X$ relation in clusters with different levels of cooling at their center. The symbols indicates the dynamical states (Mittal et al. 2011).

1.4 Formation and evolution

The cosmic structures originate from matter aggregation in a hierarchical process dominated by gravitational instability. The existence of such instabilities is inferred from observations of the anisotropies in the CMB radiation. The cosmic background density (or temperature) map is uniform in all directions in the Universe up to 1 part in 10^5.

Smaller-scale objects were formed from the growth and the collapse of the initial perturbations. Then bigger structures arose from mergers between earlier bodies, following the gravitational potential of DM halos that, in turn, collapsed before the baryonic matter. In this context, large scale structures can be seen as enormous DM halos in the center of which are assembled luminous substructures: the GCs. In these systems the equilibrium had been reached: the gravitational collapse stops since the centrifugal force balances the gravitational force.

The fluctuations in density, $\delta\rho$, which perturbed the initial homogeneous and isotropic fluid composing the Universe, can be defined as:

$$\delta = \frac{\rho - \bar{\rho}}{\bar{\rho}} = \frac{\delta\rho}{\rho}$$

where ρ is the density in a given location and $\bar{\rho}$ is the mean density of the Universe. Their width provides a distinction between two possible approaches in the formation of structures, the linear theory and the non-linear theory. The evolution of the perturbations occurs in the linear regime if $\delta \ll 1$. In this case, the solution is found by the Jeans theory. The behavior of a self-gravitating fluid is described by the continuity, the Euler and the Poisson equations. The fluid is defined by its pressure p, its density ρ, and the gravitational potential, ϕ, and the equations solutions are found by adding to the unperturbed, uniform and static fluid parameters, their perturbations $\delta\rho$, δv and so on (e.g. Coles & Lucchin 1995).

It is defined the Jeans wavelength, λ_j, that is the scale at which the pressure force balances the self-gravitating force. If the length-scale of the fluctuations is greater than λ_j the collapse occurs and the perturbation grows exponentially. If the length-scale is less than λ_j the perturbation propagates in the form of a wave.

The linear scenario predicts that perturbations undergo to a self-similar growth with time, that is $\delta_i \rightarrow \delta_i \delta_+(t)$ where the solution $\delta_+(t)$ does not depend on the scale of the perturbation, k. Then the evolution occurs equivalently in all scales. The analytical solution has been obtained in the simplest cases.

The phase of the non-linear ($\delta \gg 1$) growth of density perturbations requires the use of numerical simulations. Currently, it is preferred to use the linear theory solution to set the initial condition in the N-body numerical simulation in which a cubic volume (which represents the Universe) is modeled with a high number of gravitational-interacting particles. The cosmological simulations are powerful tools to investigate the observed scaling relations in GCs (described in Section 1.3). The simulated properties are compared with the observed clusters properties allowing to constrain the physics to be included in simulations (Borgani et al. 2004). Some of the largest simulations carried out are the Millennium simulation (Springel et al. 2005, Figure 1.1) followed by the Millennium-II, (Boylan-Kolchin et al. 2009) and the Millennium-XXL (Borgani et al. 2004), and the Illustris simulation (Vogelsberger et al. 2014).

Since the first structures formed when any physical privileged scale did not exist and the power-law function well represent a scale-free spectrum; the initial density perturbation spectrum is described by:

$$P(k) = Ak^s \tag{1.10}$$

where k is the characteristic scale of the perturbation, A is the normalization of the spectrum and s is the spectral index of the power-law. Assuming a Gaussian statistics for the mass distribution in the Universe, and defining a function $\hat{W}(kR)$ which filters the contributions of $P(k)$ for the different k and comoving scale R, it can be defined the mass variance:

$$\sigma_M^2 = \frac{1}{(2\pi)^3} \int P(k) \hat{W} dk$$

which, taking a spectrum defined in the Eq. (1.10), becomes:

$$\sigma_M^2 \propto \delta_+^2(t) k^{s+3}.$$

Knowing that $k \propto 1/R$ and $M \propto R^3$, the latter can be express in terms of mass:

$$\sigma_M^2 \propto \delta_+^2(t) R^{-(s+3)} \propto \delta_+^2(t) M^{-\frac{s+3}{3}}.$$

This defines the characteristic mass, M_*, reached which the perturbation enters in the non-linear regime. This occurs when $\delta \sim 1$ and then $\sigma_M^2 \propto \delta_+(t) \sim 1$:

$$M_* \propto \delta_+(t)^{\frac{6}{s+3}}.$$

The δ depends on the cosmological model adopted. The mass of forming structures is related to the other derivable quantities (dimension R, density ρ, and so on) providing relations observable in GCs, i.e. the largest non-linear structures formed. In this context, they play a key role for the studies of cosmological models.

1.5 Cool-core and merging clusters

Clusters dynamics affects the thermodynamics of the ICM and its properties. In general we can distinguish two classes of GCs: *cool-core* and *non-cool-core*. Cool-core clusters show a strong peak of X-ray emission in the central regions and a drop in the temperature profile toward the center. These clusters have a relaxed dynamical state although some of them show evidences

for minor mergers. Non cool-core clusters do not have a central X-ray peak and are typically merging systems.

1.5.1 Cool-core clusters

The energy loss via radiative processes in a plasma is summarized with $\varepsilon = \Lambda(T) n_e n_i$, where $\Lambda(T)$ is the *cooling function* (Sutherland & Dopita 1993), it varies with the temperature of the medium, depending on the dominant process in act. The plasma losses energy radiatively over a characteristic time scale estimated as:

$$t_{cool} = \frac{5}{2} \frac{(n_e + n_i) k_B T}{n_e n_i \Lambda(T)}.$$

If the thermal bremsstrahlung is the dominant ongoing process, as in the ICM plasma (see Section 1.1.2), t_{cool} is (Sarazin 1986):

$$t_{cool} \sim 8.5 \times 10^{10} \left[\frac{n_e}{10^{-3}\,\mathrm{cm}^{-3}} \right]^{-1} \left[\frac{T}{10^8\,\mathrm{K}} \right]^{-1/2} [\mathrm{yr}]. \tag{1.11}$$

Therefore the *cooling time* results longer than the Hubble time, t_H. This is true in almost all the cluster volume, but in the central regions where the density grows up significantly, the cooling time becomes comparable or shorter than the age of the Universe and the decrease of temperature is appreciable.

According to the Eq. (1.11), if the gas density increases, the radiative cooling processes are more and more efficient, the cooling time-scale can therefore become comparable or minor than the Hubble time. The consequent drop in temperature, observed in the central regions of clusters, necessary lead to an additional increase of density in order to maintain the balance between colder and hotter gas pressures. The growth of density occurs with the so-called *cooling flow*: external matter streams continuously towards the center (Fabian 1994). The matter accretion necessary to explain the cooling must be observed in a significant increase of star formation in the central region of clusters and in several characteristic lines of the iron-group elements. Observations in the last decade showed that the expected cooling flow rates are overestimated, rising the so-called *cooling flow problem* (see Peterson & Fabian 2006 for a review). To date, the debate on a possible justification to the cooling slowing down, finds a solution in the *AGN feedback* phenomenon. According to this model, the AGN powered by the accretion of cold gas in the GCs central regions, provides the radiative and mechanic energy necessary to heat the gas and then to quench the cooling. Several observational evidences strongly support this hypothesis, such as regions of X-ray surface brightness depression, known as *X-cavities*, which spatially match the lobes (or radio bubbles) injected in the ICM from the central AGN (McNamara & Nulsen 2007, Gitti et al. 2012).

1.5.2 Merging clusters

As described above, consecutive mergers occur in the GCs formation process. Such events dissipate a total gravitational energy of $10^{63} - 10^{64}$ ergs on a $\sim$ Gyr time-scale, thus representing the most energetic phenomenon since the Big Bang.

As a consequence, the cluster characteristics are considerably modified and reflect the dynamical state of the system (Markevitch et al. 1999). Studies on merger geometry and kinematic can be carried out from observations, mostly in X-ray band.

Considering the case of two sub-clusters with masses M_1 and M_2, located at an initial distance d_0, where they are at rest, they approach each other with a relative velocity of (Sarazin 2002):

$$v_i = 2930 \left(\frac{M_1 + M_2}{10^{15}\,\mathrm{M}_\odot}\right)^{1/2} \left(\frac{d}{1\,\mathrm{Mpc}}\right)^{1/2} \left[\frac{1 - \frac{d}{d_0}}{1 - \left(\frac{b}{d_0}\right)^2}\right]^{1/2} \quad [\mathrm{km/s}]$$

where b is the impact parameter and d is the distance of the clusters after the collision. This implies that sub-clusters move with supersonic relative speed and, consequently, large scale shock waves with moderate Mach numbers originate in the encounter. It is verified in the central region of clusters by numerical simulations and semi-analytic models (Gabici & Blasi 2003, Pfrommer et al. 2006). The outskirts seems to experience shocks with higher Mach numbers, likely due to cold gas infalling from external regions (Ryu et al. 2003, Vazza et al. 2009). The Mach number of the shock is defined as:

$$\mathcal{M} = v_i / c_s$$

where $c_s = (\partial p / \partial \rho)^{1/2}$ is the speed of sound in the medium in which the shock propagates. An adiabatic perturbation is characterized by $p \propto \rho^\Gamma$, where Γ is the adiabatic index, then the speed of sound becomes:

$$c_s = \sqrt{\frac{\Gamma k_b T}{\mu m_p}}.$$

By means of the Rankine-Hugoniot jump conditions it is possible to relate the quantities characterizing the gas upstream and downstream of the shock (see e.g. Landau & Lifshit's 1959). In particular, in the case of a monoatomic gas ($\Gamma = 5/3$) the jump conditions of temperature and density of the medium are in the form:

$$\frac{T_d}{T_u} = \frac{5\mathcal{M}_{kT}^4 + 14\mathcal{M}_{kT}^2 - 3}{16\mathcal{M}_{kT}^2}$$

$$\frac{\rho_d}{\rho_u} = \frac{4\mathcal{M}_\rho^2}{\mathcal{M}_\rho^2 + 3}$$

where the subscripts u and d indicate the quantities upstream and downstream. Then by analyzing the X-ray images and spectra, the Mach number can be inferred from fitting the above formulas to temperature and density profiles deduced across the shock region. Also the X-ray surface brightness jumps provide the measure of the Mach number. The X-rays observations can be used indeed to localize and investigate the shock front (e.g. Markevitch & Vikhlinin 2007 for review).

In addition large scale turbulence motions are induced from the energy released (Cassano & Brunetti 2005). Several dynamical processes are involved in such motions, they are studied quite accurately by numerical simulations (Vazza et al. 2006; Dolag et al. 2005; Vazza et al. 2018; Miniati 2014). However the direct observation of turbulence requires highly performing instruments. The Doppler broadening by turbulence motions was measured in the Perseus cluster thanks to the superb spectral resolution of the Hitomi satellite (Hitomi Collaboration et al. 2016). Unfortunately, the satellite was active for just one month after its lunch on March 2016. The direct detection in Perseus cluster is however a starting point for deeper studies on turbulence motions in merging cluster and it provides an observational support to numerical simulations (Mohapatra & Sharma 2019).

Most importantly for the context of this Thesis, the complex processes triggered during cluster merger may lead to the acceleration of CR in the ICM. These are responsible of the large scale synchrotron emission observed in GCs, discussed in detail in the next Chapter.

Chapter 2

Non-thermal emission from galaxy clusters

Cluster-scale synchrotron radiation is detected from a growing number of GCs proving the presence of non-thermal components in form of relativistic electrons and magnetic fields, mixed with X-ray emitting gas. This diffuse emission is spread over the cluster volume and it has not obvious optical identification. At the same time GCs host radio galaxies that, contrary to the diffuse emission, are related to discrete sources which can be observed in other wavelengths.

The presence of non-thermal plasma mixed with the thermal ICM raises questions on its origin and on its link with the microphysics of ICM. It is then important to constrain the physical mechanisms that are able to accelerate particles and to amplify the magnetic fields in GCs.

In this Chapter we describe the properties of the radio emission from GCs, with a special focus on the radio halos, the main topics of this Thesis work.

Synchrotron emission and energy losses of relativistic electrons

In this part we briefly summarize the main properties of the synchrotron emission mechanism and the electrons energy losses in the ICM. These information will be used in the following of the Chapter.

Relativistic charged particles, spiraling in a magnetic field emit synchrotron radiation. The emitting particles are not in thermal equilibrium then the synchrotron emission is a non-thermal phenomenon. The synchrotron power emitted in the frequency unit, obtained from the Fourier analysis of the signal, is a continuum function with a peak correspondent to the *characteristic frequency*:

$$\nu_s \propto (B \sin\theta)\varepsilon^2 \propto B\gamma^2 \tag{2.1}$$

where θ is the *pitch angle* between electron velocity and the magnetic field direction, B is the magnetic field strength and γ is the Lorentz factor. Depending on the magnetic field strength and the relativistic particle energy, synchrotron emission can be observed in a large frequencies domain, from radio up to X-ray. In GCs the typical value of the magnetic field is $B \sim 1\mu$ G and radiation detected at 100 MHz, is produced by relativistic electrons with $\gamma \sim 5000$.

The power per unit frequency emitted by an electron of Lorentz factor γ and pitch angle θ is given by (Rybicki & Lightman 1986):

$$P_s(\nu) = \frac{\sqrt{3}e^3 B \sin\theta}{m_e c^2} F(\nu/\nu_c) \tag{2.2}$$

$$F(\nu/\nu_c) \equiv \frac{\nu}{\nu_c}\int_{\nu/\nu_c}^{\infty} K_{5/3}(y)dy$$

$$\nu_c \equiv \frac{3}{2}\nu_s \sin\theta$$

where $K_{5/3}(y)$ is the modified Bessel function of order 5/3. By integrating the Eq. (2.2), the specific emissivity is:

$$S(\nu) \propto \int_{\gamma_{min}}^{\gamma_{max}} P_s(\nu,\gamma,\theta)N(\gamma)d\gamma \tag{2.3}$$

Assumed a power law energy distribution for the emitting electron population:

$$N(\gamma) = K\gamma^{-\delta}, \;\; \gamma_{min} < \gamma < \gamma_{max}$$

the synchrotron total intensity spectrum is given by:

$$S(\nu) \propto \nu^{-\alpha}$$

for $\nu \ll \nu_{max}$, $\alpha = (\delta - 1)/2$ is the radio spectral index. The total electron population spectrum can be seen as a superposition of the single particles emission, which radiate typically at their own characteristic frequency.

The energy distribution is modified over the electron population lifetime. Energetic particles lose more energy according while the injection of new energetic electrons can repopulate the energy distribution in the high frequencies domain. In addition to the synchrotron emission, relativistic electrons lose energy via IC emission, due to the interactions with CMB cool photons. The characteristic lifetime, t_{rad}, of electrons with energy $\ll 100$ MeV in the ICM, deduced taking into account both synchrotron and IC energy losses, is:

$$t_{rad} = 3.2 \times 10^{10} \frac{B^{1/2}}{B^2 + B_{CMB}^2}[(1+z)\nu]^{-1/2}[\,\mathrm{yr}] \tag{2.4}$$

where $B_{CMB} = 3.25(1+z)^2\,\mu$G is the CMB equivalent magnetic field due to IC process at redshift z, and ν is the observing frequency of the synchrotron radiation produced by these electrons (expressed in MHz).

As a consequence of Eq. (2.4), the high-energy particles age faster than the low-energy ones, the power-law spectrum becomes steeper beyond a *break* or *cutoff frequency*, ν_b. The break position provides then a method to infer the radiative age of the emitting particles.

For electrons with energies < 100 MeV in the ICM, the energy losses are dominated by Coulomb collisions (Sarazin 1999):

$$\frac{d\varepsilon}{dt} \propto n_{th}\left[1 + \frac{\ln(\gamma/n_{th})}{75}\right]$$

where n_{th} is the number density of the thermal protons in units of cm^{-3} and γ is the Lorentz factor. The combination of radiative and Coulomb losses gives a lifetime of relativistic electrons in the ICM of (Brunetti & Jones 2014):

$$\tau_e \sim 4\times\left\{\frac{1}{3}\left(\frac{\gamma}{300}\right)\left[\left(\frac{B_{[\mu\mathrm{G}]}}{3.2}\right)^2 + (1+z)^4\right] + \left(\frac{n_{th}}{10^{-3}}\right)\left(\frac{\gamma}{300}\right)^{-1}\left[1.2 + \frac{1}{75}\ln\left(\frac{\gamma/300}{n_{th}/10^{-3}}\right)\right]\right\}^{-1}[\,\mathrm{Gyr}] \tag{2.5}$$

that has a maximum at:

$$\gamma \sim \sqrt{\frac{3n_3}{\beta_L}}$$

where n_3 is the number density of the thermal medium in units of $10^{-3}\,\mathrm{cm}^{-}3$, and $\beta_L = (B_{[\mu\mathrm{G}]}/3.2)^2 + (1+z)^4$. Th particles lifetime is shown in Figure 2.1.

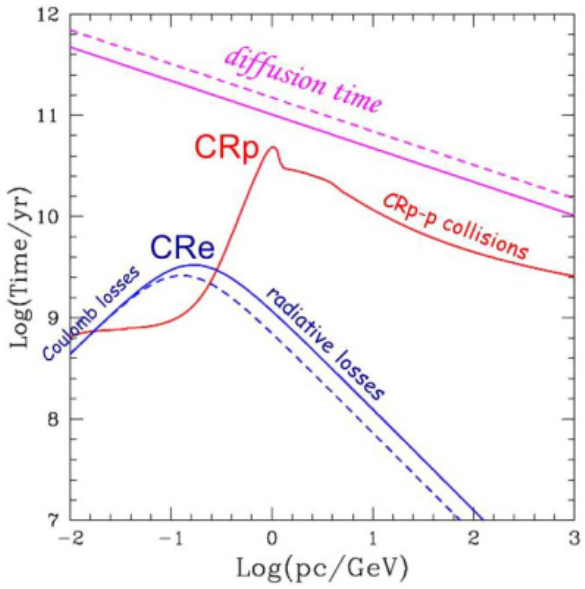

Figure 2.1: The lifetime of CRp (red line) and CRe (blue line) in the ICM at z=0, compared with the CR diffusion time on Mpc scales (magenta line). The most relevant channels of particles energy losses are indicated. The solid lines represent the lifetimes for a magnetic field of 1 μG and the dashed lines for a magnetic field of 3 μG. From Brunetti & Jones 2014.

Radio source energy budget

Here we summarize the main concepts of energy budget of relativistic plasma. The total energy of a synchrotron radio source is due to relativistic particles (electrons and protons) and magnetic field energy contributions:

$$U_{tot} = U_{el} + U_{pr} + U_M$$

The protons contribution to the total energy is assumed proportional to the electrons energy: $U_{pr} = kU_{el}$, since their emission is not detected, there is no information about their energy.

The energy provided by the magnetic field within a volume V is:

$$U_M = \frac{B^2}{8\pi}\phi V$$

where ϕ is the fraction of the volume effectively occupied by the magnetic field. Both components, electrons and magnetic fields, contribute to the synchrotron luminosity, L_{syn}:

$$L_{syn} = V \times \int_{\varepsilon_{min}}^{\varepsilon_{max}} P_s(\nu) N(\varepsilon) d\varepsilon$$

that in the case of a power-low particle energy distribution is:

$$L_{syn} \propto (B \sin\theta)^2 V N_0 \int_{\varepsilon_{min}}^{\varepsilon_{max}} \varepsilon^{-\delta+2} d\varepsilon$$

The electron total energy in the interval between ε_{min} and ε_{max} is:

$$U_{el} = V \times \int_{\varepsilon_{min}}^{\varepsilon_{max}} N(\varepsilon)\varepsilon d\varepsilon = VN_0 \int_{\varepsilon_{min}}^{\varepsilon_{max}} \varepsilon^{-\delta+1} d\varepsilon$$

It can be then described as a L_{syn} function, by eliminating VN_0:

$$U_{el} = c_{12}(\alpha, \nu_{min}, \nu_{max}) L_{syn} B^{-3/2}$$

where, following the Eq. (2.1), the energies ε_{min} and ε_{max} are expressed in terms of ν_{min} and ν_{max}. Finally the total energy becomes:

$$U_{tot} = (1+k) c_{12} L_{syn} B^{-3/2} + \frac{B^2}{8\pi}\phi V \tag{2.6}$$

Assuming the condition of minimum energy, it can be inferred how the energy is distributed between particles and magnetic field. The total energy reaches a minimum (shown in Figure 2.2) when the two components contributions are approximately equal:

$$U_B = \frac{3}{4}(1+k) U_{el}$$

The Eq. (2.6) in its minimum results:

$$U_{tot}(min) = c_{13} \left(\frac{3}{4\pi}\right)^{3/7} (1+k)^{4/7} L_{syn}^{4/7} \phi^{3/7} V^{3/7}$$

and then the minimum energy density is:

$$u_{min} = \frac{U_{tot}(min)}{\phi V} = c_{13} \left(\frac{3}{4\pi}\right)^{3/7} (1+k)^{4/7} L_{syn}^{4/7} \phi^{-4/7} V^{-4/7} \tag{2.7}$$

The constants c_{12} and $c_{13} = 0.921 c_{12}^{4/7}$ depend on the spectral index α and on the particles energy range. They have been calculated by Pacholczyk 1970. An useful expression of the Eq. (2.7) in terms of observed quantities is derived assuming $\phi = 1$ and including the k-correction:

$$u_{min}\left[\frac{\text{erg}}{\text{cm}^3}\right] = \xi(\alpha, \nu_1, \nu_2)(1+k)^{4/7}(1+z)^{(12+4\alpha)/7}(\nu_{0[\text{MHz}]})^{4\alpha/7}(I_{0_{[\frac{mJy}{arcsec^2}]}})^{4/7}(d_{[\text{Mpc}]})^{-4/7}$$

where z is the redshift; ν_0 is the observation frequency; d is the source depth and I_0 is its brightness measured at ν_0 and inferred from the radio image. The constant $\xi(\alpha, \nu_{min}, \nu_{max})$ can be found in Govoni & Feretti 2004.

The magnetic field in the equipartition condition is:

$$B_{eq} = \left(\frac{24\pi}{7} u_{min}\right)^{1/2} \tag{2.8}$$

It provides a commonly adopted approach to estimate the magnetic field strength within a synchrotron source. Nevertheless this method is still rather uncertain because of the lack of details about the filling factor ϕ, together with the inadequate knowledge on the ratio between protons and electrons energy, k. The latter value is related to the poorly known processes which originate relativistic particles. Moreover the source extension along the line of sight, d, must be assumed. Usually, the value of ϕ is set equal to 1, that of k equal to 1 or 0.

The Eq. (2.8) is obtained following the Pacholczyk 1970 argument. According to this, the synchrotron radio luminosity is evaluated in the 10 MHz and 100 GHz frequency range, impling

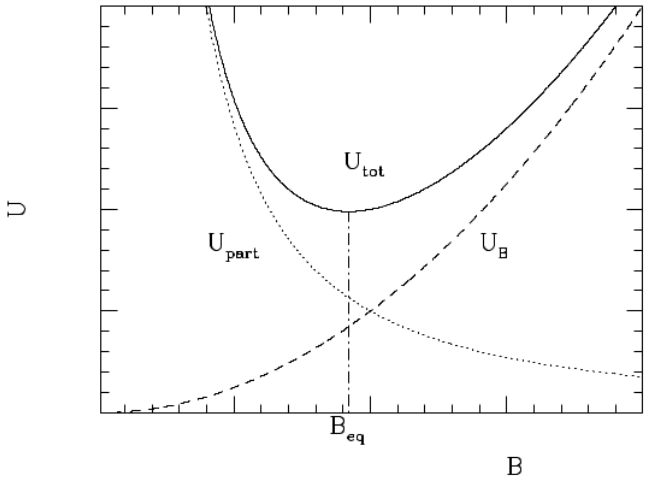

Figure 2.2: Representation (in arbitrary units) of the total energy, U_{tot}, within a synchrotron source (Govoni & Feretti 2004). It is due to contributions of magnetic field energy, U_M, and relativistic particles energy, $U_{el} + U_{pr}$.

constrains on the emitting particles energies. As pointed out by Brunetti et al. 1997, it does not exist any physical explanation that justifies the absence of lower energies electrons. Moreover the synchrotron radiation frequency depends simultaneously from both magnetic field strength and particles energy. Consequently, by fixing the frequency range, different values of B_{eq} determine the energy range of the emitting electrons.

To avoide these biases, Brunetti et al. 1997 proposed the "revised" method to derive the minimum energy conditions. The low-frequency cutoff in the synchrotron spectrum is replaced by a low-energy cut-off in the electron energy distribution. It leads to an energy ratio between particles and magnetic field of:

$$\frac{U_{el}}{U_B} = \frac{2}{1+\alpha}$$

resulting in a perfect energy equipartition condition if $\alpha = 1$. Following this approach, the magnetic field B'_{eq}, expressed in terms of the one obtained in the "classical" method, is (for $\alpha > 0.5$):

$$B'_{eq} \sim 1.1 \gamma_{min}^{\frac{1-2\alpha}{3+\alpha}} B_{eq}^{\frac{7}{2(3+\alpha)}} [\mathrm{G}]$$

where the particles energy, indicated by the Lorentz factor γ, is assumed to be $\gamma_{min} \ll \gamma_{max}$.

One of the main issues of the equipartition argument is whether equipartition between relativistic particles and magnetic fields can be reached in a physical system. The two components exchange energy via a number of mechanisms, including wave-particles coupling (Melrose 1980). However equipartition takes time and in general particles have mechanisms of energy losses that may be faster than the mechanisms of dissipation of magnetic field (or vice versa). Radio galaxies have dynamical lifetimes that are similar to the lifetime of relativistic electrons, in this case equipartition is possible in principle and indeed it has been measured in several cases (Hardcastle et al. 2002). For this reason in Chapter 6 we will use equipartition formulae in the case of the head tail radio galaxy in Abell 1622 cluster. In general equipartition is more difficult to understand in clusters scale radio sources, radio halos, relics and mini halos (described in the next Sections). In these cases the dynamical lifetime of the radio sources and the magnetic field

dissipation time-scale in the ICM are much longer than the lifetime of relativistic electrons and for these reasons in the clusters studied in this Thesis we will not apply equipartition.

2.1 Radio Galaxies

GCs host radio galaxies. Relativistic particles and magnetic fields in radio galaxy are generated near the supermassive black hole of the central AGN and/or along relativistic jets and hot spots (G. Miley 1980).

Radio galaxy morphology is characterized by extended or compact shapes and a wide range of sizes, from few pc to Mpc-scale. They exhibit an optical counterparts, generally a giant elliptical galaxy. Collimated jets transport radiation, particles and magnetic field, outwards from center. The interaction between jets and the external medium can produce the hotspots, regions where the plasma is re-accelarated by the shock wave produced in the encounter. The particles population ages in the lobes, extended structures surrounded the hotspots. Radio emission from these sources is typically described by a flat spectrum ($\alpha \sim 0$) in the compact, central region, which steepens towards jets and hotspots ($\alpha \sim 0.5 - 0.7$). The oldest emitting particles of the lobes has $\alpha > 1$.

Based on the morphology and radio power, Fanaroff & Riley 1974 classified radio glaxies in the two Fanaroff-Riley classes: the FRIs (Figure 2.3a) are the weakest radio galaxies: the major part of the emission comes from the nucleus, lobes are not well defined and there are no hotspots; the FRIIs (Figure 2.3b) are the strongest radio galaxies: the emission is dominated by lobes and hotspots, jets are more collimated than in the FRIs. Radio galaxies with a 1.4 GHz band luminosity of $L_{1.4\,\mathrm{GHz}} \leq 10^{25}\,\mathrm{WHz}^{-1}$ are typically FRIs, while those with higher luminosity are classified as FRIIs.

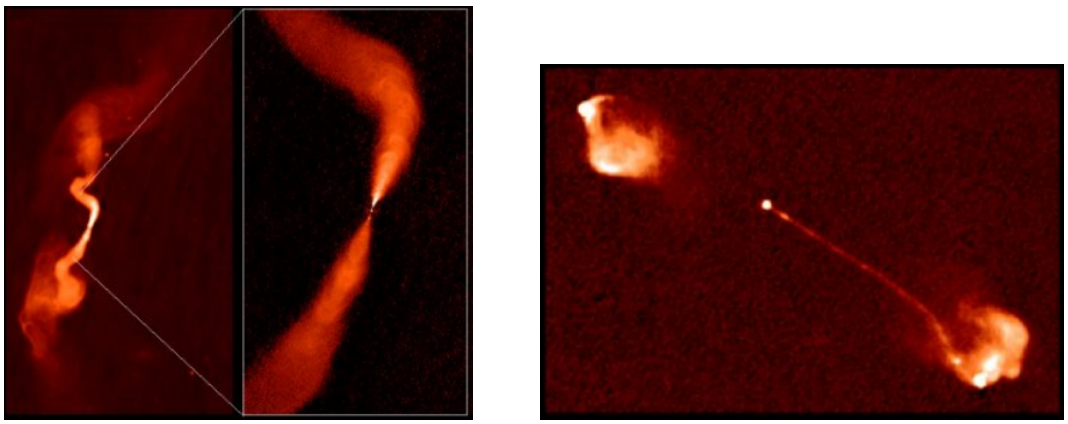

(a) (b)

Figure 2.3: VLA radio images of (a) FRI radio galaxy 3C31 and (b) FRII radio galaxy 3C175.

Although there is still some debate, it is currently thought that FRIs are found in GCs, while FRIIs are commonly isolated or located in low-density environment, such as groups.

Interestingly the interaction between relativistic plasma and the ICM affects the morphology of radio galaxies. Thus their morphology is also a probe of the external medium and of feedback mechanisms that operate in GCs. In rich GCs, radio galaxies typically present asymmetric morphology, with bent jets, due to the interplay with the dense ICM (e.g. Owen et al. 1985). On the basis of the angle between the two jets, they are classified as *wide-angle tails* (WATs), with jets weakly deflected (Figure 2.4a), and *narrow-angle tails* (NATs), also known as *head-tail* (HTs), with tightly packed jets (G. K. Miley et al. 1972, Figure 2.4b). Such differences in morphology are in part result of the different speeds with which the galaxies hosting WATs and

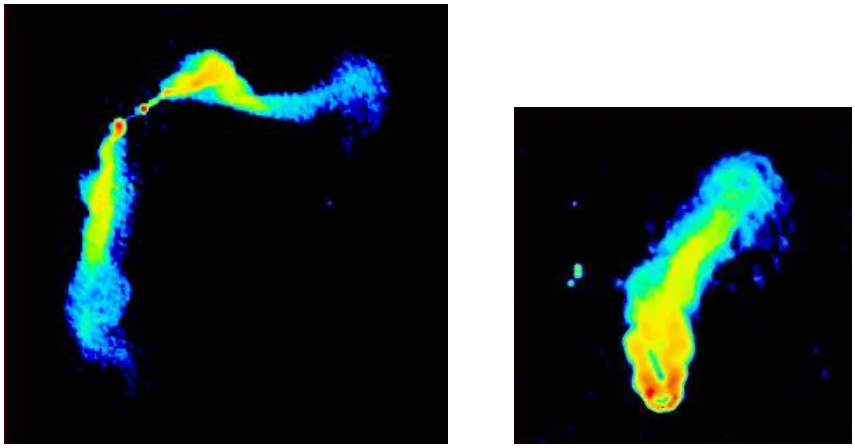

(a) (b)

Figure 2.4: VLA radio images of (a) WAT radio galaxy 3C465 and (b) NAT radio galaxy 3C175.

NATs move under the action of the GC potential well (G. Miley 1980). The in-falling galaxies undergo to the "ram-pressure" given by the surrounding ICM: $P_{ram} = \rho_{ICM} v^2$, where v is the velocity of the galaxy respect to the environment and ρ_{ICM} is the density of ICM.

The WAT sources are observed in central region, where the hosting galaxy is almost at rest with a velocity of the order of $100\,\mathrm{kms}^{-1}$ or less. They are usually associated with the cD galaxy of the cluster. On the other hand, the NAT hosting galaxies move with higher velocity ($v \sim 1000\,\mathrm{kms}^{-1}$). Since in some cases the only ram pressure effect fails to explain the WATs and NATs characteristics, it has been more recently proposed additional interpretation which involves ongoing sub-structures mergers (e.g. Bliton et al. 1998; Sakelliou & Merrifield 2000).

Multi-frequency analysis comparing radio to X-ray data are generally carried out to constrain the HTs interplay with thermal ICM. The confinement of the radio source by the external environment can be quantified measuring the thermal pressure, inferred from X-ray analysis, and the non-thermal pressure, derived from radio observations (discussed in Section 6.3). In absence of information about the radiating electrons and magnetic field energy fraction in the radio source, an estimation of the non-thermal pressure is usually obtained by assuming the equipartition condition.

2.2 Diffuse radio emission from galaxy clusters

Diffuse radio emission on 100-1000 kpc scale is observed in a significant fraction of massive GCs. The diffuse radio emission in GCs has low surface brightness ($\sim \mu Jy$ arcsec^{-2} at 1.4 GHz) and steep spectra ($S_\nu \propto \nu^{-\alpha}$, with $\alpha > 1 - 1.3$). Based on their morphology, their location in the cluster, dynamical state of the hosting system (merging or cool-core clusters) and their radio properties, these objects are classified in giant halos, relics and mini halos (e.g. Feretti et al. 2012; van Weeren et al. 2019 for reviews).

2.2.1 Radio Halos

Large scale diffuse emission in the form of radio halos (RHs) is detected in about 30 percent of the massive GCs. These giant structures with typical sizes of 1-2 Mpc are located in the central volume of the cluster and show a quite regular morphology. The radio emission generally follow the thermal gas distribution, as also revealed from the point-to-point correlation between radio and X-ray brightness distributions (Govoni et al. 2001; Rajpurohit et al. 2018), suggesting a

tight connection between the two components.

The prototype of RH emission, Coma C, is fuound at the center of the Coma cluster (Figure 2.5). After the first detection carried out by Large et al. 1959, it have been studied in detail as its closeness (z = 0.0231) makes it the ideal laboratory to explore the RHs properties (Giovannini et al. 1993; Thierbach et al. 2003; S. Brown & L. Rudnick 2011).

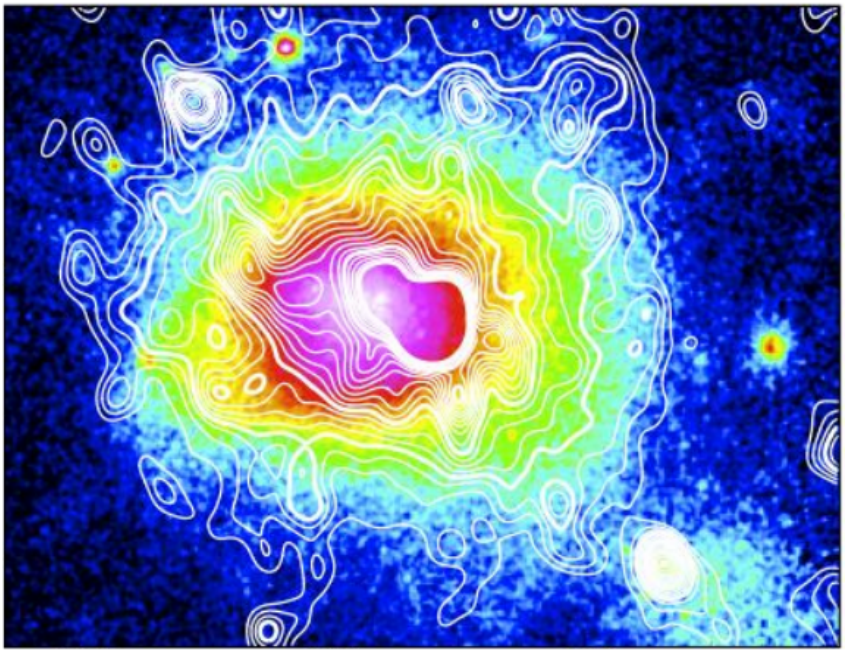

Figure 2.5: RH at the center of Coma cluster (image from S. Brown & L. Rudnick 2011). Radio contours are overlapped to the X-ray emission (colors).

The great majority of RHs have been found in clusters which show complex dynamical properties underlying ongoing mergers (Cassano et al. 2010a; Cuciti et al. 2015); this connection suggest an interplay between mergers and the mechanisms of acceleration of relativistic electrons. RHs are more common in massive GCs with high X-ray luminosity and high ICM temperature (Giovannini et al. 1999; Cassano et al. 2010b, Cuciti et al. 2015); this also suggest a role of the cluster mass and gravitational potential well as reservoir of the energy that is necessary to activate non-thermal phenomena. Their emission is generally unpolarized, except few peculiar cases[1]. The lack of observed polarization is partially due to the beam depolarization[2] suggesting that the emission sites are mixed in the ICM and that magnetic fields are turbulent.

To date, about 65 extended radio sources in GCs are classified as RHs, the most distant of which is in El Gordo observed at z=0.87 (Lindner et al. 2014; Botteon et al. 2016b). The majority of the sources have been historically detected in the NRAO VLA Sky Survey (NVSS, Condon et al. 1998) and the WEsterbork Northern Sky Survey (WENSS, Rengelink et al. 1997). The 1.4 GHz radio luminosity of currently observed RHs spans from 10^{23} to 10^{26} WHz^{-1}. The typical spectral index is $\alpha \sim 1.3$ (Venturi et al. 2013). Since the great majority of radio observations in the past has been carried out at high (GHz) frequencies the measured spectra may be biased and RHs with steeper spectrum may be lost in past observations. In fact RHs with steeper spectrum, with $\alpha \gtrsim 1.6$ (up to $\alpha \sim 2$), do exist (e.g. Wilber et al. 2018; Brunetti et al. 2008; Giovannini et al. 2009 Dallacasa et al. 2009, this case is shown in Figure 2.6) and are called Ultra

[1]Three RHs seems to exhibit an appreciable level of polarization: Abell 2255, MACS J0717.5+3745, and Abell 523 (Govoni et al. 2005;Bonafede et al. 2009; Girardi et al. 2016).

[2]This effect occurs when it is observed an extended source not uniformly polarized and the beam size is larger than the angular scale over which the magnetic field of the source is coherent.

Steep Spectrum Radio Halos (USSRHs). More recently the Giant Metrewave Radio Telescope (GMRT) survey (Venturi et al. 2008; Venturi et al. 2009) and the low frequencies surveys such as the GaLactic and Extragalactic All-Sky MWA Survey (GLEAM, Wayth et al. 2015) and the LOFAR Two-metre Sky Survey (LoTSS, Shimwell et al. 2019 described in the next Chapter) increased the amount of cataloged RHs.

Thanks to the improved observational capabilities at low frequencies with GMRT and now LOFAR, several USSRHs have been discovered in the last years (Macario et al. 2010; Bonafede et al. 2014a; Shimwell et al. 2016; Venturi et al. 2017; Wilber et al. 2018; Savini et al. 2018) suggesting that these RHs are fairly common. The significant spread in the observed spectrum of RHs and the presence of spectral curvature in some cases suggests that these radio sources are generated by electrons with a complex spectrum, possibly with a break in the energy distribution at higher, few GeV, energies (Brunetti & Jones 2014 for a review).

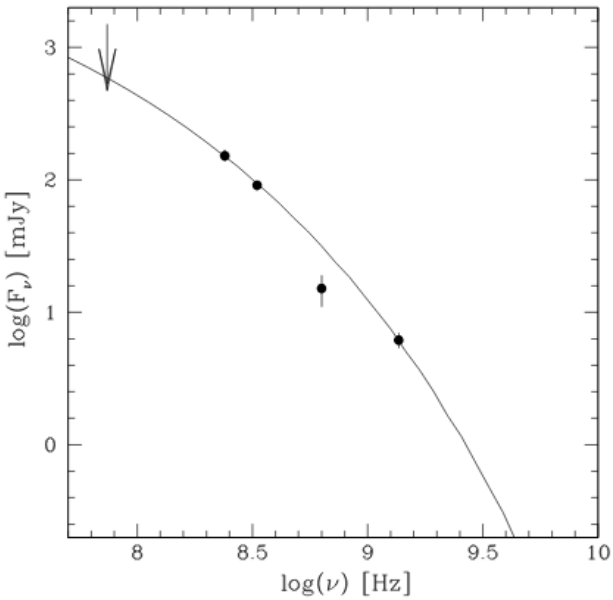

Figure 2.6: Synchrotron spectrum of the RH detected in A521. The spectrum is obtained at 74, 240, 330, 610 MHz by Brunetti et al. 2008 from the GMRT observations, and at 1.4 GHz by Dallacasa et al. 2009 from the VLA follow up.

RHs Origin

The main question in explaining the RHs origin concerns the mechanism which provides a population of relativistic particles which radiates over RHs-scale distances. The emitting particles lifetime is considerably shorter compared to the time-scale on which electrons diffuse on distances $L \sim$ Mpc (Figure 2.1). The first is defined in Eq. (2.4) while the latter is the diffusion time, t_{diff}, and it is:

$$t_{diff} \sim \frac{L^2}{4D}$$

where D is the spacial diffusion coefficient. With typical values of GCs it is of the order of 10^{11} yr thus resulting much longer $t_{rad} \lesssim 10^8$ yr (van Weeren et al. 2019). The idea that particles propagate within the cluster volume after they have been locally accelerated must be replaced by some mechanism acitve on sizes comparable to that of clusters. This fact gives rise to the so-called *slow diffusion problem* (Jaffe 1977). Over the past years two main scenarios have been proposed.

Hadronic model (or secondary model) Inelastic hadronic collisions between ICM thermal protons and CR protons (CRp) generate the energetic radiating particles, i.e. secondary electrons (Dennison 1980; Blasi & Colafrancesco 1999; Pfrommer & Enßlin 2004). Such kind of interactions lead to CRp decay in neutral pions (π_0) which in turn decay in γ-rays and in a cascade of secondary particles (including relativistic electrons, CRe). Thermal protons in ICM are found everywhere in the cluster and, since CRp have a longer radiative life-time respect to the electrons one, even they can spread and accumulate in the cluster (Berezinsky et al. 1997). This would explain why RHs emission spatially matches the ICM morphology.

The strongest observational constrain against this model as the only mechanism involved in the production of energetic particles is given by the current upper limit into the γ-ray emission from GCs, set by Fermi-Large Area Telescope (LAT) observations (Atwood et al. 2009). If the model is correct γ-ray unavoidably must be detected as products of CRp decays (T. E. Jeltema & Profumo 2011; Brunetti et al. 2012; Brunetti et al. 2017; Zandanel & Ando 2014). Furthermore, RHs emission should be observed in any type of clusters because theoretically CRp are stored in both dynamically disturbed and relaxed cluster. Indeed sources of particles injection are common to all GCs, such as radio galaxies, supernovae, galactic winds (Brunetti et al. 2007). As well ICM thermal protons are present in every clusters, irrespective of the dynamical state. Moreover well-known spectrum of Coma cluster with the most recent observations of USS sources, provides a further evidence not in accordance with the model (Brunetti & Jones 2014; van Weeren et al. 2019).

Leptonic model (or re-acceleration model) Particle acceleration is triggered by large scale turbulence dissipated in thermal ICM. This is injected in the plasma as a consequence of merger events that channel a fraction of the kinetic energy into turbulent motions ($\sim 15\% - 20\%$ according to numerical simulations, Vazza et al. 2006). Particles undergo Fermi II mechanisms in which they are accelerated stochastically interacting with magnetic field inhomoginities induced by turbulence. Due to the nature of the process, model requires pre-existing energetic particles, which have to be re-accelerated through Fermi II processes (Brunetti et al. 2001; Petrosian 2001). The seed particles come from AGN outflows, starburst events and galactic winds. The clear correlation between dynamical disturbed structures and RHs occurrence is in agreement with this scenario. The diffusion problem is solved since the mergers involve cluster-scale regions and then particles can be re-accelerated "in-situ" on these scales. Being related to merger events, the RHs emission is not a permanent phenomenon. Its existence lasts as far as the dynamical effect perturbs the gas. Taking into account the time-scale on which turbulence dissipate energy and the cluster crossing time, the predicted RHs lifetime is about 1-2 Gyr, inferred by merger numerical simulations.

The following statistical results corroborate the predictions of this model, which represents the preferred scenario of RH origin to date.

RHs scaling relations

A well-established connection exists between the RHs luminosity at 1.4 GHz and the X-ray luminosity of the ICM in the 0.1-2.4 keV energy range (Feretti 2003; Enßlin & Röttgering 2002; Figure 2.7a). The $P_{1.4\,\mathrm{GHz}} - L_X$ actually reflects the relation between RHs power to the cluster mass. Since the X-ray mass (inferred by X-ray luminosity) can be biased by an eventual cool-core at the cluster center, it is recently preferred to relate the $P_{1.4\,\mathrm{GHz}}$ to the mass measured with the integrated SZE signal. Adopting SZE as mass-proxy reduces the relation scatter (Figure 2.7b). The mass parameter is connected also with RHs occurrence in GCs: it have been observed that RHs detection increase significantly in systems with higher X-ray luminosity (and then mass). Recent study carried out by Cuciti et al. 2015 on a cluster sample with $M > 6 \times 10^{14}\,\mathrm{M}_\odot$,

confirms the mass-RHs occurrence relation: about $\sim 60\% - 80\%$ of halos are found in clusters with $M > 8 \times 10^{14}\,\mathrm{M}_{\odot}$, the fraction become of the order of $\sim 20\% - 30\%$ in lower mass clusters.

The previous relations in combination with the fact that RHs are not common in all clusters support the re-acceleration scenario (Cassano et al. 2007; Cassano et al. 2008). Furthermore, improved instruments with higher sensitivity, are employed in the investigation of large scale diffuse radio sources in GCs. Particularly in the 610 MHz frequency, the GMRT contribution to set deep upper limit in the detectable diffuse emission flux (Venturi et al. 2008), lead to find out a "radio bimodality" of GCs (Brunetti et al. 2009). In the $P_{1.4\,\mathrm{GHz}} - L_X$ diagram, clusters split in two populations: (i) clusters without diffuse radio emission lie below the correlation and (ii) clusters with RHs emission follow the correlation (Figure 2.7a).

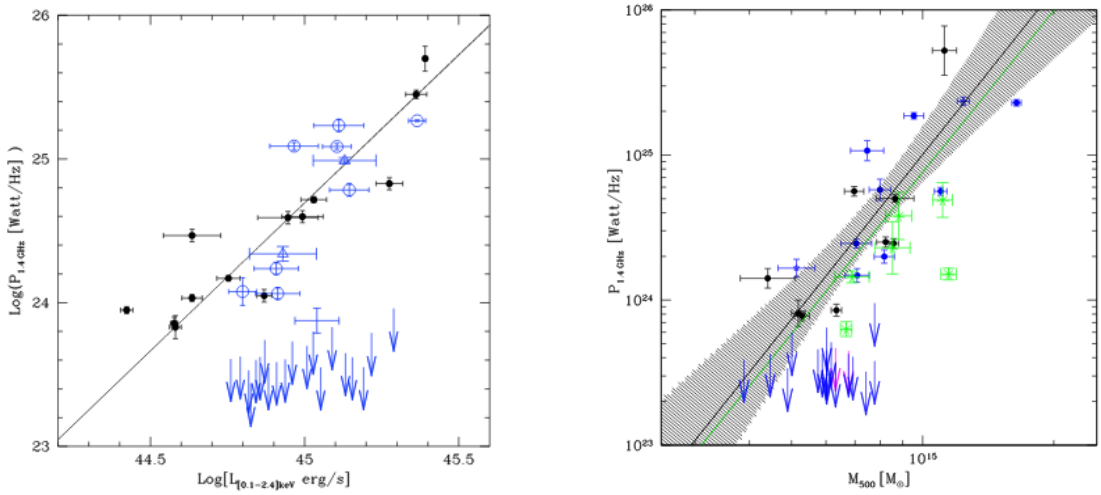

(a) (b)

Figure 2.7: *Left panel*: Distribution in the $P_{1.4\,\mathrm{GHz}} - L_{0.1\text{–}2.4\,\mathrm{keV}}$ diagram of RHs in GCs, sampled with GMRT (blue) and taken from the literature (filled black symbols). The clusters lacking of halos detection are marked with the arrows. These upper limits are set on the basis of GMRT capabilities. The solid line outlines the best fit of the correlation (Brunetti et al. 2009). *Right panel*: Distribution in the $P_{1.4\,\mathrm{GHz}} - M_{500}$ diagram of samples of clusters from GMRT surveys (in blue points and blue and magenta arrows) and RHs from the literature (black points). With green asterisks are marked USSRH. The clusters are part of the Planck SZ (PSZ) cluster catalog (Planck Collaboration et al. 2014), from which are taken mass measures within R_{500}, measured through SZE (Cassano et al. 2013).

Thermal gas and galaxies within unrelaxed cluster exhibit recognizable features of the dynamical activity. Measures of the galaxies velocity distribution in optical band, for example, and characterization of thermal gas morphology, are used to infer the clusters dynamical state (some studies in optical wavelengths are reported in Ferrari et al. 2003 and Boschin et al. 2004, while X-ray studies are Feretti et al. 2000 and D. Buote 2001). Particularly, the estimation of cluster morphological parameters from the X-ray surface brightness, such as the centroid shift, w, and the concentration parameter, c, is commonly adobted. Basically, the w expresses the displacement of the X-ray surface brightness from its peak and c gives the fraction of the X-ray emission in the central region of the cluster respect to the emission from larger size (D. Buote 2001). Other parameters are the dipole power ratios P_1/P_0, P_2/P_0, P_3/P_0. It has been found that the cool-core clusters have low values of w and high values of c while the opposite condition is observed for merging clusters. The link between RHs and the hosting cluster dynamical state is suggest by the fact that in the c-w plane the clusters with halo are found in merging system as shown in Figure 2.8 (Cassano et al. 2010b).

Thus the bimodality separates the different dynamical states of hosting clusters: the ones showing diffuse radio emission are merger systems while those in which halos are absent, are typically relaxed structures. In re-acceleration context, the radio bimodality can be interpreted as a sequences of different phases of the RHs evolution, driven by the progress of the merger in the hosting system. Higher synchrothon emission evolves from higher efficiency in the early stage of the dynamical activity, to lower values, as turbulence proceed to extinguish. In agreement in the course of the merger event, RHs moves from the correlation zone in the diagram to the upper limit region.

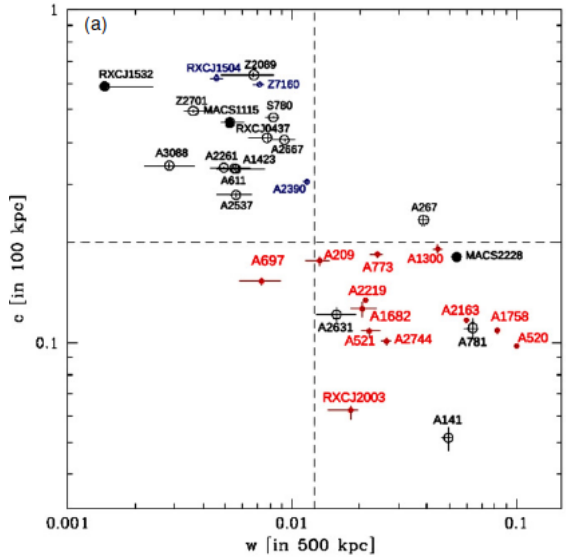

Figure 2.8: Distribution in the c-w plane of a GCs sample selected from the ROSAT-ESO Flux-Limited X-ray (REFLEX; Böhringer et al. 2004) and the extended ROSAT Brightest Cluster Sample (eBCS; Ebeling et al. 1998; Ebeling et al. 2000) catalogs. The radio sampling of the clusters are carried out by the GMRT RH survey (Venturi et al. 2008; Venturi et al. 2009). The symbols mark: RH (red filled dots), no RH (black open dots), MH (blue open dots). The vertical and horizontal dashed lines denote the median value of parameters, c=0.2, w=0.012. The diagram highlights the anti-correlation between the parameters and the clear separation between the radio emitting GCs and the radio quiet ones. The distribution trend evidences that the presence of RHs is connected to a disturbed dynamical state of the hosting cluster (Cassano et al. 2010b).

2.2.2 Radio Relics

Radio relics are diffuse synchrotron sources generally found in the peripheral regions of GCs. They are characterized by arc-shape morphology, extended on Mpc-scale.

Relics show low surface brightness and steep spectrum with average integrated spectral index of $\alpha \sim 1.2 - 1.3$ (Feretti et al. 2012; van Weeren et al. 2019). Opposite to halos, relics are strongly polarized, with linear polarization levels up to the 30% are typically measured. The high polarization in radio relics and their peripheral (Mpc distance) position (where Faraday depolarization is smaller) allows to constrain the magnetic field and its topology (Figure 2.9).

Relics origin is likely due to particles acceleration (Ensslin et al. 1998; Roettiger et al. 1999), or re-acceleration (Markevitch et al. 2005; Kang et al. 2012), triggered by shock waves crossing the ICM. The shocks occur as a consequence of merger phenomenon, the dynamical effects on the plasma depend on the energy involved in the event. The hypotesis that links the relics origin with the accelaration of particles by shocks is well-established (e.g. Brunetti & Jones 2014 for a review). First of all in many cases a shock coincident with the radio relic is found

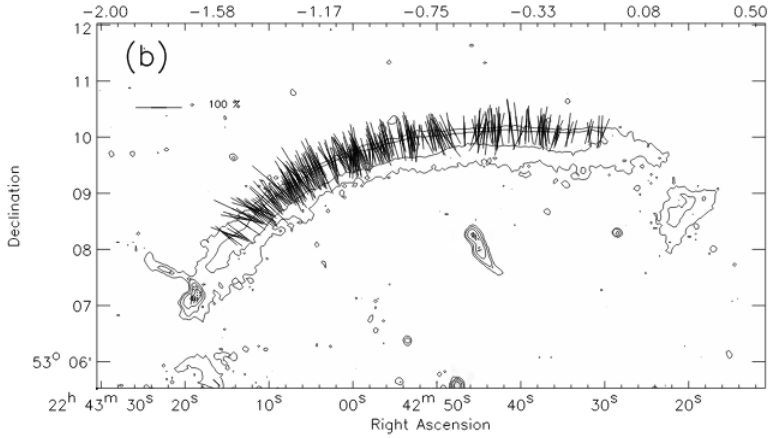

Figure 2.9: Polarization electric field vector map of the northern radio relic in CIZA J2242.8+5301. Radio contours are from the high resolution 610 MHz image obteined with the GMRT (van Weeren et al. 2010).

from X-ray observations (Akamatsu & Kawahara 2013, Botteon et al. 2016a). The magnetic field orientation, inferred from the polarization analysis, results aligned with the relics long axis, suggesting that the magnetic field is compressed by the shock passage in that region. Also, studies on the spectral index show a steepening of the spectrum along the relics minor axis, toward outside of cluster. This suggest that electrons population is accelerated in the shock front, and lose energy downstream. Furthermore, as evidence of the connection with merger shocks, some remarkable systems with double radio relics have been discoverd (i.e. Bagchi et al. 2006). The observation of these arc-like emission, symmetrically located respect to the cluster center, is in accordance with the predictions on merging events inferred from numerical simulations (Roettiger et al. 1997). The prototypical example detected in the cluster A 3667 is shown in Figure 2.10.

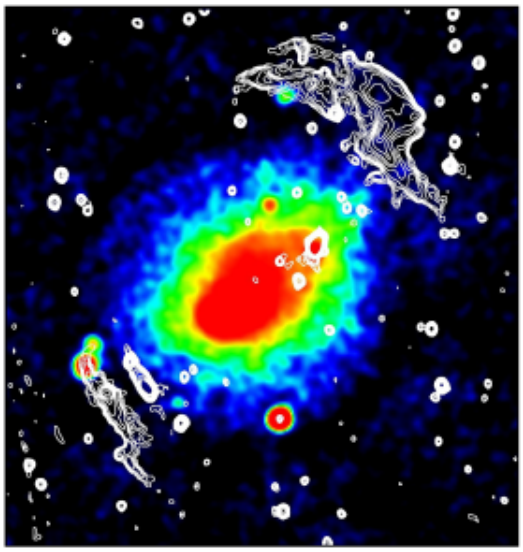

Figure 2.10: The double radio relics (contours) observed in the cluster A 3667 matched with the ICM X-ray emission (colors) (Rottgering et al. 1997).

Unfortunatly, the mechanism of emitting particles acceleration is still unclear. A suitable description is given by the *diffusive shock accelaration* (DSA) theory (e.g. Krymskii 1977; Bell 1978). According to this the acceleration occurs through Fermi I processes. Basically particles

scatter up and downstream the shock front and gain energy in each shock crossing.

However since shocks in cluster mergers are characterized by low Mach numbers, the particles energy spectra predicted by the DSA model are very steep and in tension with observations of the synchrotron spectrum of radio relics (e.g. Brunetti & Jones 2014; van Weeren et al. 2019 for reviews). Then to explain the radio relic emission, the re-acceleration models predict a preexisting population of relativistic electrons lying in clusters that can be efficiently re-accelerated by low Mach number shocks (van Weeren et al. 2017).

As RHs are linked to the hosting GC properties, a correletion between thermal X-ray luminosity and relics radio luminosity have been observed (Feretti et al. 2012). It is likely a consequence of the less-biased scaling relation between cluster mass and radio luminosity, more recently studied (de Gasperin et al. 2014). Even relics morphology and location reflect thermal properties of the gas: the radio relics with larger linear size (LLS) are assosiated with more massive clusters (de Gasperin et al. 2014, Bonafede et al. 2012).

2.2.3 Mini halos

Mini halos (MHs) are another class of diffuse radio sources in GCs. They are similar to giant RHs but extend on smaller scales, 100-500 kpc, and are generally confined to the cores of galaxy clusters. They have radio powers at 1.4 GHz in the range of $10^{23} - 10^{25}\,\mathrm{WHz}^{-1}$ and, as their giant versions, are centrally located, with round-shaped and characterized by steep spectra. The prototype of these sources is detected in the Perseus cluster, shown in Figure 2.11. As the giant halo Coma C, this MHs is well studied due to its vicinity (z = 0.0179).

Observationally MHs are more difficult to study than giant RHs. In several cases the emission of the MHs is not much more extended than the lobes of the central BCG. The detection of diffuse radio emission from MHs is then challenging, as it must be disentangled by the emission from the bubbles (Baum & O'Dea 1991; Mazzotta & Giacintucci 2008). This circumstance requires high resolution images to separate the contributions. Additionally, since MHs are very faint compared to AGN radio emission, observations with high dynamic range are necessary to overcome the gap between the surface brightness levels of the two sources.

Contrary to giant RHs, the MHs are observed exclusively in cool-core clusters which are dynamically relaxed, without any evidences of cluster major mergers (Giacintucci et al. 2017). Further discrepancy is in the synchrotron volume emissivity which is generally higher in MHs (Murgia et al. 2009). These differences suggest that the mechanisms that generate giant RH and MHs are different.

Despite the MHs sizes are smaller than those of giant halos, they are still more extended than the scale covered by the diffusion of relativistic electrons in a radiative lifetime. This excludes the possibility that MHs are generated by relativistic electrons injected from the central AGN. To date the mechanism which supplies synchtrotron emitting CRs on large scale is still rather unclear. The debate is divided on two possible models, basically the same proposed for the RHs origin, i.e. the hadronic or secondary model (Pfrommer & Enßlin 2004), and the turbulence or re-acceleration process (Gitti et al. 2002). According to the latter, in MHs case, the turbulence motions are generated by the cold gas sloshing in the cluster potential well (ZuHone et al. 2013; ZuHone et al. 2013). In fact a connection with cold fronts is verified in a series of studies (i.e. Mazzotta & Giacintucci 2008). Even in the sloshing-driven turbulence scenario a population of seed supra-thermal electrons is requested since the turbulent acceleration is inefficient in extracting electrons directly from the thermal ICM. In this context, the central AGN likely provides the necessary fossil plasma. Contrary to RHs current gamma ray upper limits do not challenge secondary models for MHs (Taylor et al. 2006).

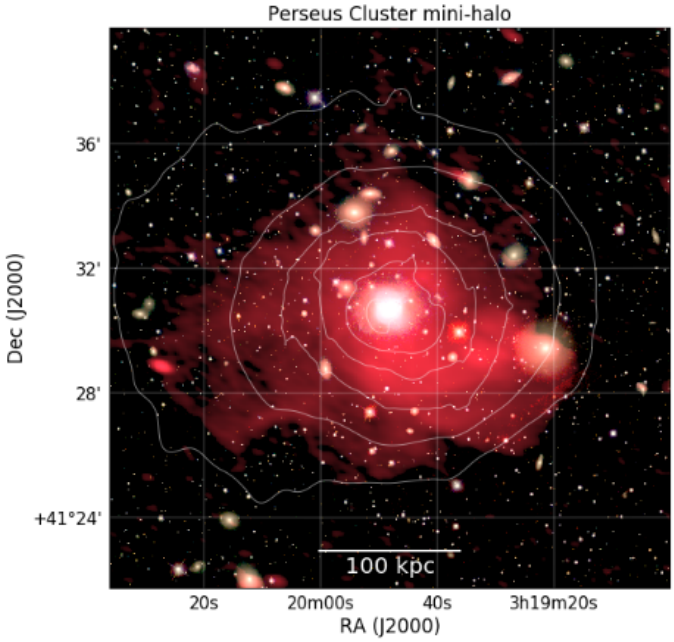

Figure 2.11: Radio diffuse emission (red) of the MH in Perseus cluster superimposed on the SDSS optical image (Abolfathi et al. 2018). White contours delineate the X-ray surface brightness (From van Weeren et al. 2019).

2.3 The importance of low frequency radio observation

All the classes of sources described above are characterized by a steep spectrum being much more luminous at lower frequencies. For this reason deep observations at low frequencies are ideal to unveil the population of these sources.

Enßlin & Röttgering 2002 explored the potential of radio surveys at low frequencies for the study of RHs. They combined the clusters X-ray luminosity functions with the radio luminosity - X-ray Luminosity correlation (see Section 2.2.1) to estimate the radio luminosity function of RHs in the Universe (RHLF). The calculation was carried out assuming that 1/3 of all clusters host a RH with $\alpha = 1$ and, in the simplest case discussed, this fraction is independent on cluster size and redshift. In this way they obtained the RHLF (Figure 2.12a) and, they deduced the correspondent flux density distribution (Figure 2.12b). The latter provided the predictions on the detectable RHs by the new generation of low frequency interferometer like LOw-Frequency ARray (LOFAR), Allen Telescope Array (ATA), Expanded VLA (EVLA), Sky Kilometer Array (SKA), and, at that time already operative, GMRT. With the LOFAR capabilities at 120 MHz it was expected that $\sim 800 - 1200$ RHs would have been uncovered in just one year.

In the last decade several observational evidences provided support to the scenario based on turbulent acceleration (see Section 2.2.1). These models predict a population of USSRH emerging at lower frequencies. In particular, Cassano et al. 2010a obtained RHLFs in different frequencies (Figure 2.13) in order to explore the potential of LOFAR surveys in searching for RHs. One of the main results of the study is the prediction that about 350 RHs would be observable at $z \leq 0.6$ and about 55% of these would exhibit a spectral index > 1.9 in the 250-600 MHz range. Low frequency surveys thus provide crucial test of current models.

In general, low frequencies observations of synchrotron sources provides information on the lowest energy population of emitting particles. These particles have longer lifetimes (see Section 2, Figure 2.1) and thus are probes of the life-cycle of relativistic plasma in the ICM. This life-cycle is still poorly explored and has a potential impact on the mechanisms of feedback in the

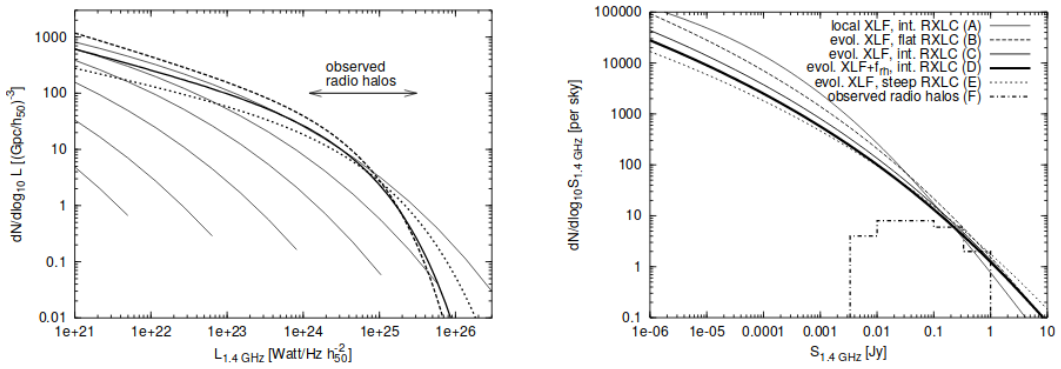

(a) (b)

Figure 2.12: The RHLF and the RHs predicted flux density distribution as derived by Enßlin & Röttgering 2002. *Left:* RHLF. Different lines indicate the assumptions underlying the calculation. The thick lines represent the RHLF obtained with the observed X-ray luminosity function and the fraction of cluster hosting RHs equal to 1/3 (simplest case). The thin solid lines describe the RHLF deduced taking into account the evolution of the cluster X-ray and radio properties with the redshift. *Right*: Flux density distribution. Different lines marks the models of X-ray luminosity function and $P_{1.4\,\mathrm{GHz}} - L_X$ correlation steeps adopted to infer the distribution.

ICM and on the origin of cluster scale radio emission.

Remarkably LOFAR observations have recently discovered a radio galaxy tail with very steep spectrum ($\alpha \sim 4$) in the Abell 1033 cluster (de Gasperin et al. 2017). The tail is invisible at high frequency (Figure 2.14). The analysis of the spectral behavior of the synchrotron emission along the tail has demonstrated that gentle mechanisms of particle acceleration in the tail affect the evolution of particles making their lifetime significantly longer than expected from standard aging arguments. This discovery has the potential of fundamental implications on the life-cycle of relativistic plasma in the ICM .

In conclusion the new instruments operating in the low frequency band are entering an uncharted territory with the potential of a strong impact on our understanding of the physics of radio sources in the ICM. We anticipate that large part large part of this Thesis work involves LOFAR data.

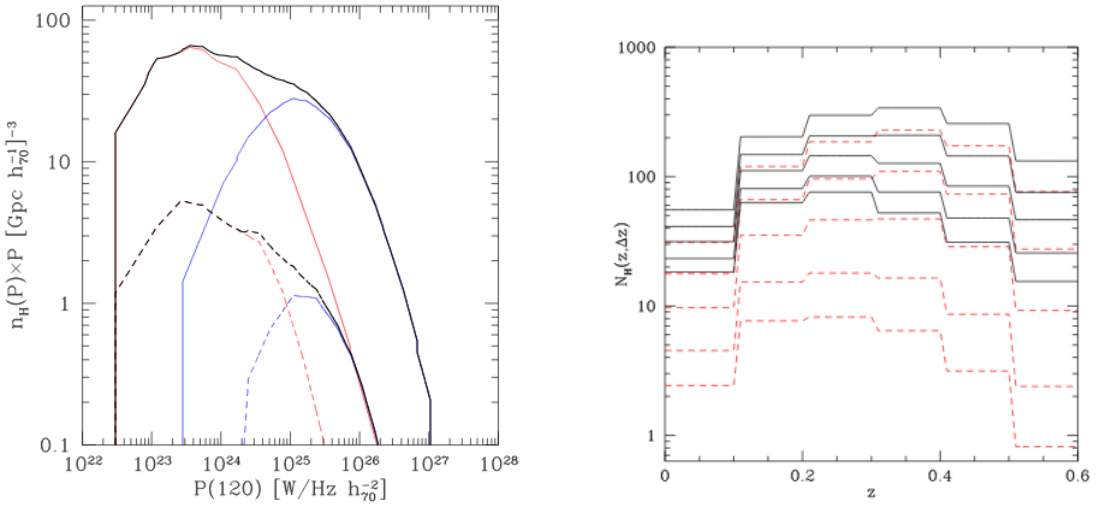

(a) (b)

Figure 2.13: *Left*: The RHLFs at different frequencies and redshift. The dominating solid black line is referred to $\nu = 120$ MHz for clusters at redshift 0-0.1, while the black dashed lines is deduced for cluster redshift of 0.5-0.6. The contribution from halos with $120\,\text{MHz} \leqslant \nu \leqslant 600\,\text{MHz}$ is represented with the red lines and with $\geqslant 600$ MHz with the blue lines. *Right*: Number of RHs as a function of redshift detectable with LOFAR surveys sensitivity. The black lines is referred to the prediction at $\nu \geqslant 120$ MHz and the red lines give the numeber of RHs at $120\,\text{MHz} \leqslant \nu \leqslant 600\,\text{MHz}$ (Cassano et al. 2010a).

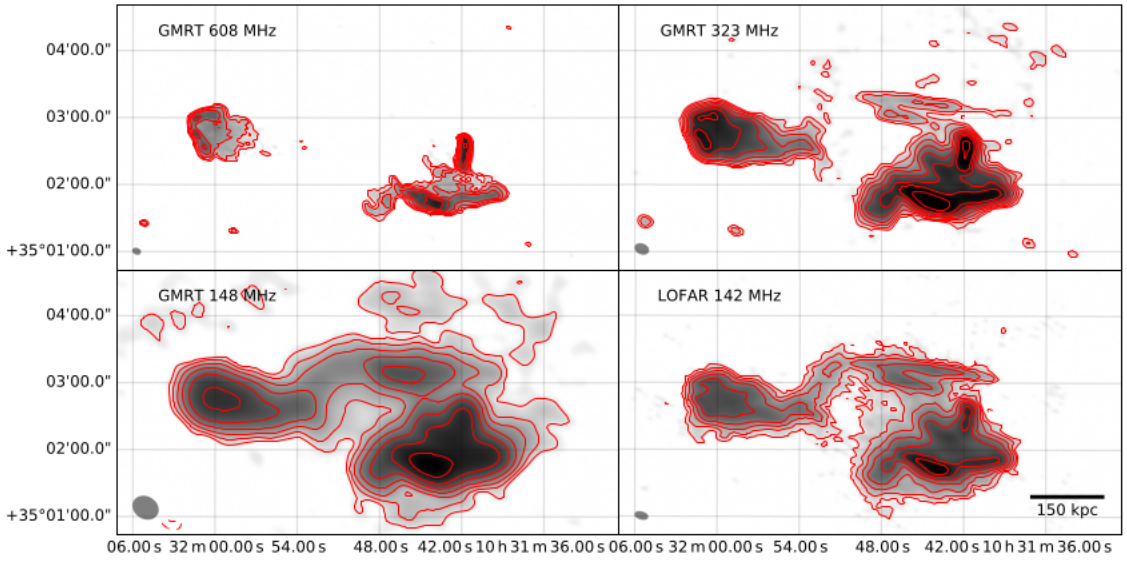

Figure 2.14: The tail of the radio galaxy in A1033 cluster as seen at 608, 323, 148, and 142 MHz. Only at lower frequencies it is detected a peculiar radio emission. Due to the high resolution ($10.3'' \times 4.9''$) LOFAR image at 142 MHz the two trails of the GReET can be separete (de Gasperin et al. 2017).

Chapter 3

The LOFAR era

3.1 The LOw-Frequency ARray

The International LOw-Frequency ARray (LOFAR, van Haarlem et al. 2013) is a new generation radio telescope representing the state-of-art of the highly sensitive low-frequency receivers. The project started thanks to the Netherlands Institute for Radio Astronomy (ASTRON) and currently involves astronomical institutions of several European countries. The array is composed by a large and growing number of stations spread on a wide area across Europe. Working in the 10-240 MHz band, LOFAR provides the opportunity to explore the low-frequency part of the electromagnetic spectrum with an unprecedented sensitivity and angular resolution. Furthermore, due to its remarkable technological network and complex software infrastructure for the data acquisition, transport and analysis, LOFAR is the largest and most important pathfinder of the Sky Kilometer Array (SKA)[1].

The separations between the international LOFAR stations provide very extended baselines which in turn allow to obtain sub-arcsecond resolution over the LOFAR operational frequency band. On the other hand the closer stations give an excellent surface brightness sensitivity and provide shorter baselines that allow the observation of large-scale emission. LOFAR improves the sensitivity and angular resolution of past facilities observing at low radio frequencies by almost 2 orders of magnitude. For this reason LOFAR is expected to open a new observational window of the Universe and promises important discoveries in different areas of astrophysics and cosmology. The main research area for which LOFAR have been designed are summed in the six Key Science Projects (KSPs). These regard: (i) Epoch of reionization, (ii) Cosmic rays, (iii) Solar physics and space weather, (iv) Transients, (v) Cosmic magnetism of the nearby universe and (vi) Surveys for the investigation of different targets. Particularly one of the main goals of the the latter KSP is the study of the diffuse radio emission in GCs. This Thesis is based on LOFAR observations of three clusters using data from the Survey KP.

3.1.1 System overview

At the time of this Thesis writing, LOFAR consists of a network of 51 stations spread in major part in the north of Europe (Figure 3.1). Particularly in Netherlands are located 38 stations. The remaining ones are distributed in Germany (6), the UK (1), France (1), Sweden (1), Poland (3) and Ireland (1), Latvia (1). In the near future they will be added another station in Italy (planned for the 2021).

The stations main properties are summarized in Table 3.1. They are arranged in the array in the following way:

[1] https://www.skatelescope.org/

Figure 3.1: The map of the LOFAR stations distribution over the European continent. They are included the forthcoming station in Italy. (Credit: ASTRON).

- 6 closely situated stations within a diameter of 320 m, the so-called "Superterp", provide the shortest baselines.
- 24 stations inside a radius of 2 km near the town of Exloo, in the Netherlands, form the dense core.
- 14 stations in the Netherlands constitute the remote stations. These follow an approximate logarithmic spiral distribution, reaching 180 km in diameter with center in Exloo.
- 14 international stations are spread over Europe without a planned pattern. Their location is determined by existing facilities and infrastructures.

While the core and the remote stations position in Netherlands have been planned to optimize the uv-coverage for the KSPs success, the international stations position are decided on the basis of accords with the host countries. Then the longest baseline distribution is not specifically designed to maximize the achievable uv-coverage.

Table 3.1: Summary of the LOFAR stations and antennas (from van Haarlem et al. 2013).

Stations configuration	Number of stations	LBA dipoles	HBA tiles	Min. baseline (m)	Max. baseline (km)
Superterp	6	2×48	2×24	68	0.24
NL Core Stations	24	2×48	2×24	68	3.5
NL Remote Stations	15	48	48	68	121
International Stations	13	96	96	68	$\sim 2000^{\uparrow}$

Notes. The 6 Superterp stations are a sub-array of the core stations. $^{\uparrow}$The longest baseline extension will increase due to the additional future station.

The fundamental element of a LOFAR station is the antenna. Each station hosts two types of antenna: the High Band Antennas (HBA, working in the range 110-240 MHz) and the Low

Band Antennas (LBA, working in the range 10-90 MHz). In total about 8.000 elements are disseminated over Europe. Due to this large amount, the antennas are designed to be small and relatively low-cost. The number of antennas in each LOFAR station depends on its configuration (Table 3.1). The different configurations determine the effective area, the full-width half-maximum (FWHM) and the field of view (FoV) of the observation. These parameters vary in each frequency band. Then the configuration adopted for the observation is driven by the project goal. Details on the different configuration can be found in van Haarlem et al. 2013.

Single antenna elements are connected to the electronics via coaxial cables. The electronics is placed in each station within a dedicated cabinet. The hardware for the first data processing performed directly at the station is contained in this cabinet. The signal is digitalized and the datastreams enter the digital electronics section, that is the main responsible for the beam-forming. Further processing is done in the remote station. Once concluded the beam-forming step, the data packets are sent in the wide-area network to the correlator at the Central Processing (CEP), located at the Centre for Information Technology (CIT) of the Groningen University. Here the datastreams are processed resulting in a wide variety of data products.

Low Band Antenna

The lowest frequencies are explored through the LBAs operating between 10 MHz up 90 MHz. Since the strong radio frequency interference (RFI) affects the lowest frequencies and the FM band is near to the highest frequency end, the actual operative range is limited to 30-80 MHz (Figure 3.2, right). A LBA design is relatively simple, sturdy (allowing an operative life time of at least 15 years), and relatively low-cost. It is made by a dipole able to detect two orthogonal linear polarizations. The copper wires which receive each polarization are combined with a low-noise amplifier (LNA) into a molded lid at the top of a PVC pipe. On the other side, the wires are connected to a a metal mesh on the ground (Figure 3.2, left). The antenna structure is elementary as much as performing. The capability of observing all-sky simultaneously allows to a fast production of all-sky images on short time-scales. This properties is particularly significant for the aim of detecting transients and for the study of the large-scale Galactic structure from the Milky Way.

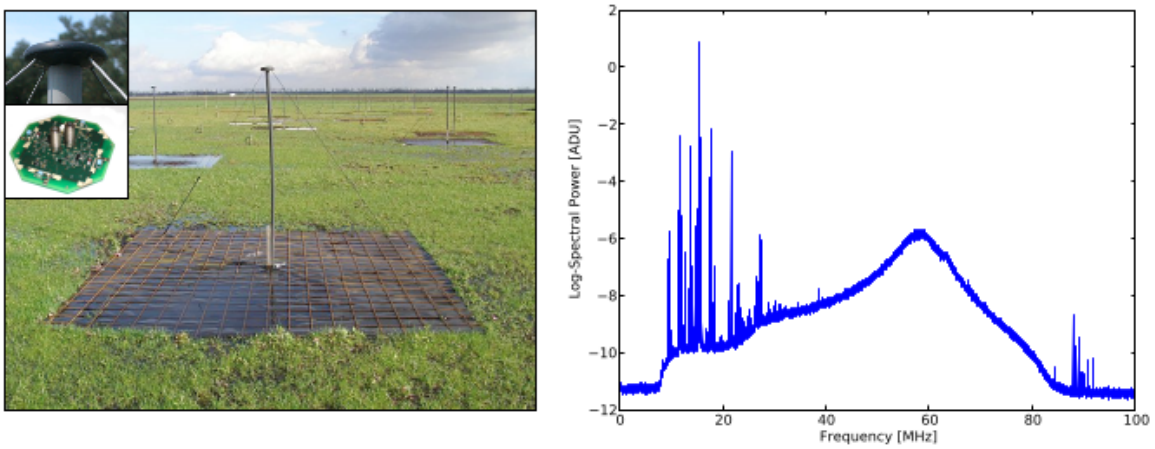

Figure 3.2: *Left*: A LOFAR LBA consisting of the two copper wires, a vertical shaft and a molded head. A zoom of this is shown in the top-left panel together with a wires attachment point. *Right*: The median spectrum averaged on all LBA dipoles in an exemplar station (CS003). They are visible either the RFI in the lowest frequencies (< 30 MHz) and the disturbances of the FM band above 80 MHz. The peak of the dipoles response is near 58 MHz (from van Haarlem et al. 2013).

High Band Antenna

The HBAs work in the range of 110-250 MHz. Due to the strong RFI near the higher-end of the band, the actual operative range is restricted to 110 MHz (Figure 3.3, right). At these higher frequencies, the appropriate design to minimize the contribution of the electronics to the system noise (with a low budget) given a cluster of 16 dual dipole antennas grouped into squares of 4×4 elements, forming a "tile". Tiles have incorporated amplifiers and an analogic beam-former. A single "tile beam" is given by the combination of the signals from each 16 antenna elements in phase for a given direction on the sky. A polystyrene structure supports the aluminum antenna elements within each tile. This is covered by polypropylene foil layers to avoid damages from the weather conditions (Figure 3.3, left).

As in the case of LBAs, the signal collected is transported with coaxial cables to the receiver unit in the electronics cabinet.

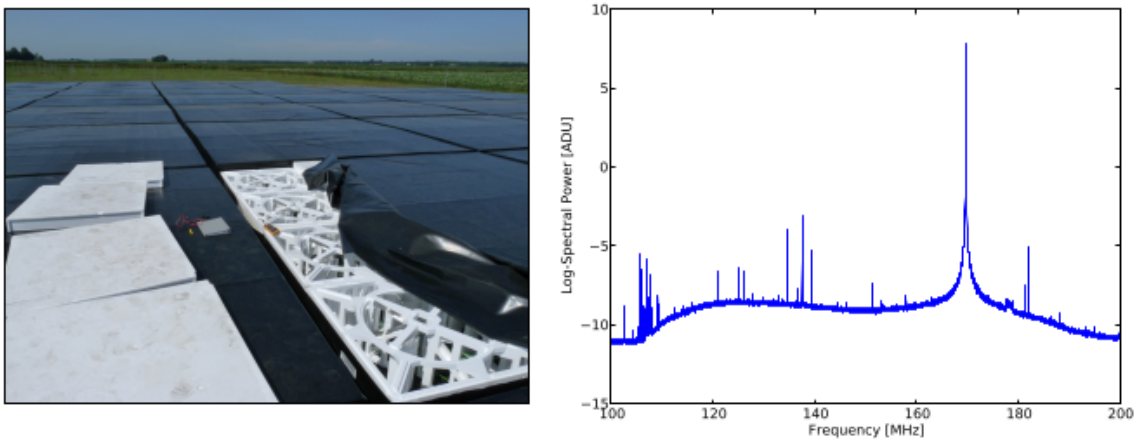

Figure 3.3: *Left*: The close-up of a LOFAR HBA tile. The dipole device and the surrounded structure covered by protective layers have been partially exposed. *Right*: An example of HBA median spectrum averaged for all the HBA tile in a station (CS003). It is affected by several RFI together with a strong peak near 170 MHz due to an emergency pager signal (from van Haarlem et al. 2013).

The data analyzed in this Thesis work are part of the LOFAR Two-metre Sky Survey. These observations use HBA antenna. In the following we describe the main characteristics of the survey.

3.2 The LOFAR Two-metre Sky Survey

The LOFAR Two-metre Sky Survey is the main effort of the Survey KP (Shimwell et al. 2017). It is designed to observe the northern hemisphere in the 120 - 168 MHz range providing a never reached deep view of the radio sky in this spectral range. The LoTSS started on 2014 May 23 within the Hobby-Eberly Telescope Dark Energy Experiment (HETDEX, Hill et al. 2008) Spring Field region ($10^h45^m00^s <$ right ascension $< 15^h30^m00^s$ and $45°00'00'' <$ declination $< 57°00''00''$, shown in Figure 3.4). The region was chosen since it represents a vast and high elevation contiguous area for LOFAR and it matches with the Sloan Digital Sky Survey (SDSS, York et al. 2000) leading to imaging and spectroscopic information.

The survey is still ongoing, and almost 1/2 of the norther sky has been already observed. A first run of analysis has been carried out for the 350 square degrees in 63 pointings of the HETDEX region and the data products for this region have been recently released (Shimwell et al. 2019). That area is just the 2% of the survey total field, however about 325000 new radio sources have been detected in this area.

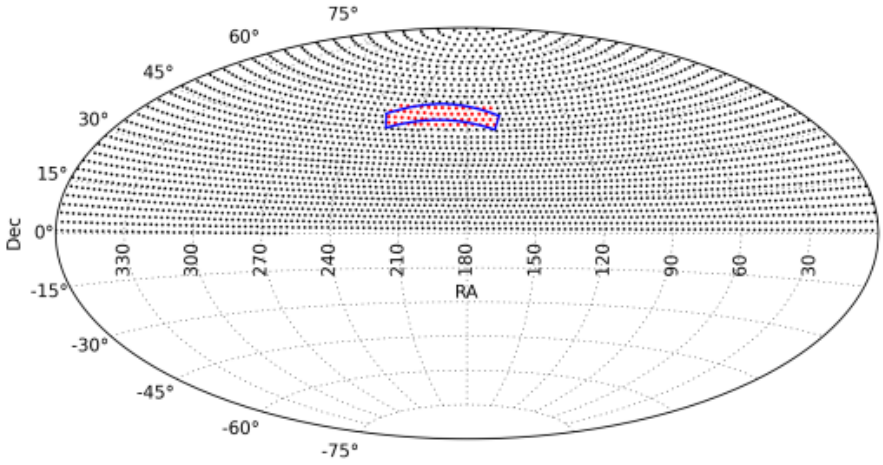

Figure 3.4: LoTSS pointings grid (in black). Highlighted in blue is the region of the HETDEX Spring Field. The red points marks the pointings observed and presented in Shimwell et al. 2017 from which this image is taken.

The LoTSS data are suitable to many area of research in the low frequency radio regime. The main goal of the survey is to investigate the formation and evolution of massive black holes, galaxies and large-scale structures including GCs. These aims are driven by the predictions of precedently studies carried out by Wilman et al. 2008 about radio galaxies; and by Enßlin & Röttgering 2002 and Cassano et al. 2010a about diffuse radio emission in GCs. In this context, in the previous Chapter we outlined the significant progresses which can be carried out on the study of large-scale synchrotron emission in GCs thanks to observation at low frequencies.

In addition to the scientific drivers, the survey probes the highly performing technical LOFAR capabilities. The LoTSS is carried out by the HBA antennas of LOFAR. The primary intents are to realize high-fidelity images with a sensitivity of less than 0.1 $\mathrm{mJy} \cdot \mathrm{beam}^{-1}$ and an angular resolution of $\sim 5''$ at the central frequency of 144 MHz.

Whit these purpose LoTSS will sign a turning point in wide-area surveys (Figure 3.5). It is much deeper than the first HBA LOFAR survey, the Multifrequency Snapshot Sky Survey (MSSS, G. H. Heald et al. 2015) and it exceeds in sensitivity others surveys in the same low-frequency radio band such as, GaLactic and Extragalactic All-sky MWA (GLEAM, Wayth et al. 2015), and the TIFR GMRT Sky Survey alternative data release (TGSS-ADR1, Intema et al. 2017) as shown in Table 3.3. In particular the sensitivity of the survey is less than 5 $\mu\mathrm{Jy} \cdot \mathrm{beam}^{-1}$ at 1.4 GHz considering a spectrum of RH of $\alpha > 1.3$, thus provides most sensitive observations -in the next decade- for the study of RH.

At the time of the preliminary data release (Shimwell et al. 2017) the imaging requirements were not achieved, since only the direction-independent calibration (together with the direction-dependent calibration in the next Chapter) was performed on the data. Then the errors in the beam model and the varying ionospheric distortions were not corrected allowing to reach just 500 $\mu\mathrm{Jy} \cdot \mathrm{beam}^{-1}$ at an angular resolution of $25''$. Instead the first full-quality public data release (Shimwell et al. 2019) provides a sensitivity of less than 100 $\mu\mathrm{Jy} \cdot \mathrm{beam}^{-1}$ thanks to the development of efficient imaging pipelines, totally automated, dedicated to direction-dependent calibration (Figure 3.6).

The amount of sources detected in HETDEX field implies that the source density is about 10 times higher than the most sensitive wide-area radio-continuum surveys performed to date. Williams et al. 2019 and Duncan et al. 2019 provide the optical identification and the photometric redshift estimates of the sources detected in the first data release. The spectroscopic redshifts

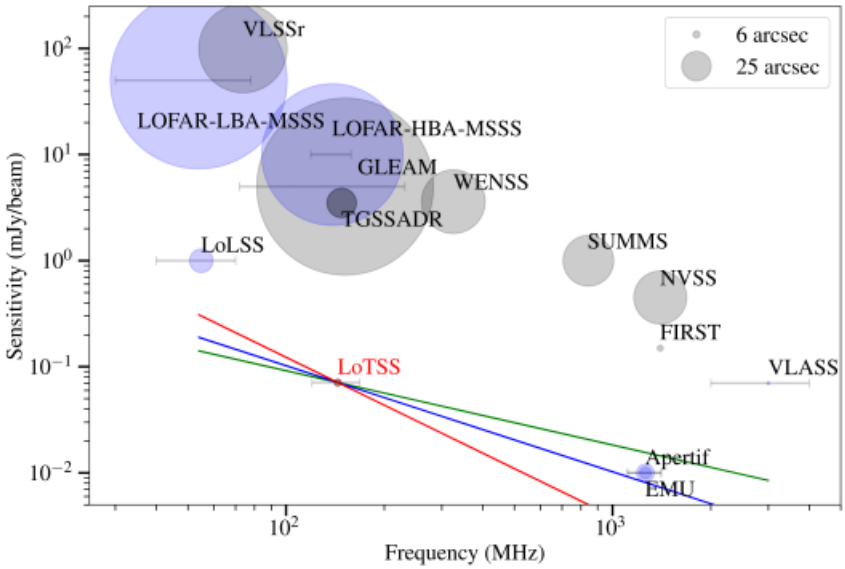

Figure 3.5: The comparison between different complete (grey) and ongoing (blue) radio surveys on the basis of their image rms, frequency and angular resolution (corresponding to the radius of the markers). The lines represent an equivalent sensitivity to LoTSS for compact radio sources with spectral indices of 0.7 (green), 1.0 (blue), and 1.5 (red) (Shimwell et al. 2019).

Table 3.2: Properties of recent wide-area low-frequency surveys (from Shimwell et al. 2017).

Survey	Resolution ($''$)	Noise mJy $\cdot$ beam^{-1}	Frequency (MHz)	Area
VLSSr (Lane et al. 2012)	75	100	73-74.6	$\delta > -30°$
MSSS-LBA (G. H. Heald et al. 2015)	150	50	30-78	$\delta > 0°$
MSSS-HBA (G. H. Heald et al. 2015)	120	10	119-158	$\delta > 0°$
GALEM (Wayth et al. 2015)	150	5	72-231	$\delta > +25°$
TGSS ADR (Intema et al. 2017)	25	3.5	140-156	$\delta > -35°$
LoTSS	5	0.1	120-168	$\delta > 0°$

Notes. The sensitivity and resolution are reference values to make possible a comparison between surveys. Actually these characteristics vary within each survey.

for the LOFAR targets will be possible in the next years with the WEAVE spectrograph (Dalton et al. 2012), part of the WEAVE-LOFAR survey. The latter will allow to obtain spectra of about 10^6 sources observed with LOFAR (Smith et al. 2016).

The parameter of the observations (Table 3.3) are decided taking into account the principal goals of the survey. Amongst the HBA LOFAR possible configurations, the LoTSS utilizes the `HBA_DUAL_INNER` (more informations about LOFAR configurations in van Haarlem et al. 2013). This is chosen in order to preserve a reasonable number of short baselines and to avoid additional calibration problems due to non-uniform beam shapes. The primary beam for this configuration is: $FWHM = 1.02\lambda/D$, where λ is the wavelength of the observation and D is the `HBA_DUAL_INNER` stations diameter that is 30.75 m (van Haarlem et al. 2013). The station beam $FWHM$ is 4.75° at 120 MHz and 3.40° at 168 MHz. On the basis of the experience from the previous interferometeric survey, it has been decided a separation between pointing of $\sim 2.58°$ which provides a nearly uniform sensitivity coverage, a reasonable number of pointings, and a good sampling of the sky area (Shimwell et al. 2017).

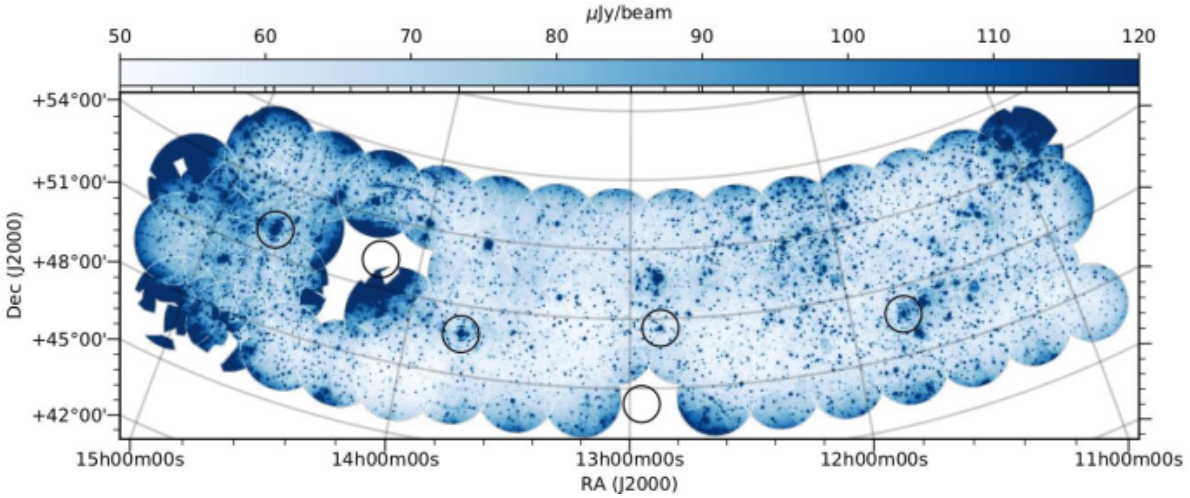

Figure 3.6: Image of the noise in the first LoTSS data release. The median noise level is 71 $\mu\text{Jy} \cdot \text{beam}^{-1}$. Such low noise level can be obtained with the direction-dependent calibration (Shimwell et al. 2019).

Table 3.3: Properties of LoTSS (from Shimwell et al. 2017).

Number of pointings	3170
Separation of pointings	2.58°
Integration time	8h
Frequency range	120-168 MHz
Configuration	`HBA_DUAL_INNER`
Angular resolution	5″
Sensitivity	100 $\mu\text{Jy} \cdot \text{beam}^{-1}$
Time resolution	1 s
Frequency resolution	12.2 kHz

Notes. The sensitivity and resolution are estimations because they vary within the different pointings. The sensitivity may decrease at low declination due to the station beam enlargement.

Chapter 4

Data analysis

This Chapter describes the X-ray and radio data processing that we performed to achieve the final targets images. From these, we inferred some measures in each band, such as flux density and luminosity. Both images and first results will be employed afterward in the multi-frequency analysis (discussed in the next Chapter), to investigate the correlation between the non-thermal emission and the thermal gas dynamical conditions in GCs. Similar processes are adopted for the data reduction of each clusters in both X-ray and radio band. Then we summarize the general steps of the analysis.

4.1 LOFAR data

Data calibration

We briefly delineate the calibration method applied to the LOFAR HBA observations of LoTSS (see previous Chapter) fields. This step was carried out by the LOFAR Surveys KSP Team while reimaging was performed during the Thesis.

The calibration aim is to produce high-fidelity images taking advantage of the high quality of LOFAR data. The procedure consists of two phases: the non-directional calibration and the directional calibration.

First one flagging of bad data due to the RFI in the flux calibrator data takes place. This is done with `AOFlagger` (Offringa et al. 2012). In addition, the contribution of the side lobes due to the bright sources Cassiopeia A and Cygnus A is also subtracted in this step. The influence of these sources becomes significant in the wide field of view (FoV) observation as those carried out by LOFAR. The data are then partially averaged in time and frequency. Complex gains for each antenna stations are obtained through modeling the primary calibrator according to the flux density-scale of Scaife & George H. Heald 2012. Since each remote station is equipped with its clock and all of them are not perfectly synchronized with the clock of the core stations, they have to be re-aligned periodically. This leads to clock offsets, that appears as time-dependent delays in the phase recorder by each station, proportional to the frequency (Figure 4.1a). Moreover, a varying refractive index across incoming signal path introduces a propagation time and direction-dependent delays in the phase, which is inversely proportional to the frequency. At the first order the refractive index depends only on the density of free electrons integrated along the line of sight, called total electron content, TEC (Figure 4.1b). This effect represents one of the most severe challenges of observations with large array. In fact distant stations are affected by different layers of the ionosphere in which the TEC can significantly change. However the two kinds of phase delays can be separated if the full-bandwidth calibration solutions cover a large enough frequency range as in HBA observations. These effects are corrected with the Clock-TEC separation method outlined by van Weeren et al. 2016 with which the effects are handled and

corrected.

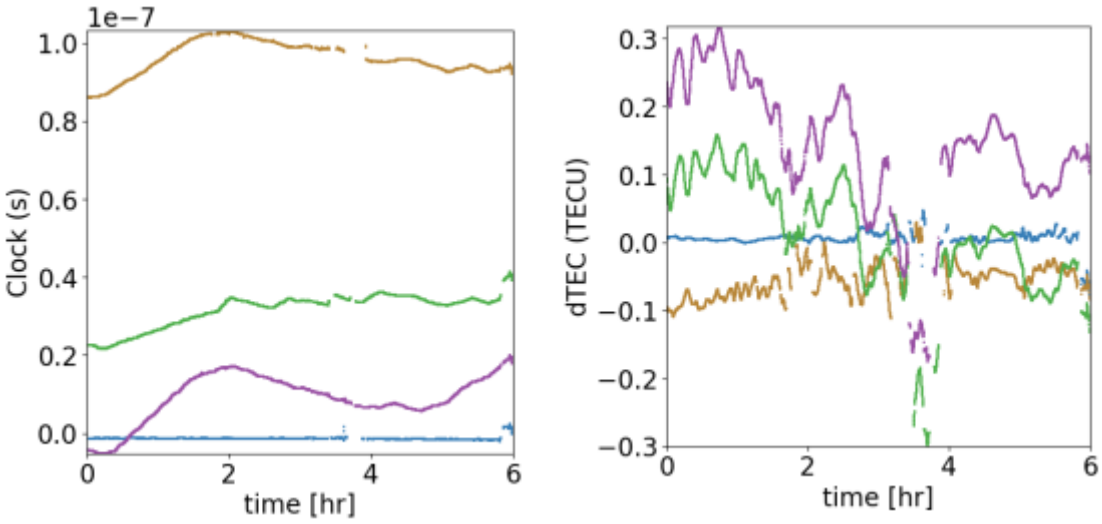

(a) (b)

Figure 4.1: Ionospheric effects on the phases for four stations (RS106, brown; RS508, green; RS509 purple; and CS302, blue): in (a) clock delays and in (b) delays due to TEC along the line of sight. The phases are derived with respect to the core station CS002. The CS302 does not show significant delays and the phase is about zero since all the core stations referred to the same clock. The RS508 and RS509 TEC trends are similar because they are close each other. The TEC unit (TECU) is set to the value typically observed at zenith during the night, that is 10^{16} m^2. The jumps in the data are due to the flagging of time intervals (de Gasperin et al. 2019).

The time-independent amplitude and clock solutions are applied to the target data which were previously flagged as done for the calibrator. Also the target data are averaged in time and frequency. At this point it is implemented a phase calibration using a sky model generated from the sources detected in several surveys (the VLSSr, Lane et al. 2012; the WENSS, Rengelink et al. 1997; and the NVSS Condon et al. 1998). The solutions are provided with a time interval of 32 s. The final step is to identify and remove the time periods in which the target phase solutions show rapid large variations. The phase solutions of each station vary smoothly as a function of time with respect to the closest one. Then if it is found a time interval where the phase solutions compared to the same solutions smoothed in time differ significantly, this time period it is flagged due to the poor ionospheric conditions (Figure 4.2).

Now amplitude and phase self-calibration process on the direction-independent calibrated data is implemented within frequency sub-bands (SBs). The self-calibrated data are then imaged at low and medium resolution in each SBs. The extended and compact sources respectively are detected and then removed from the images. The sources detection is carried out through the software PYthon Blob Detector and Source Finder[1] (`PYBDSF`, Mohan & Rafferty 2015). The tool is able to detect portion of the image in which the signal is higher than a given threshold. The final products of the procedure are new sky models made of the subtracted sources and residual datasets for each SB.

The direction-dependent calibration is now performed to correct the data for direction dependent effects (DDEs): due to the large primary beam of the LOFAR array, beam model errors and ionospheric distortions, variations across the FoV are not negligible. The method adopted consists in the fragmentation of the filed into regions, called “facets”. In each of these, phase and amplitude are calibrated. The calibrators are bright sources lying in the facets. On the

[1]https://www.astron.nl/citt/pybdsf/

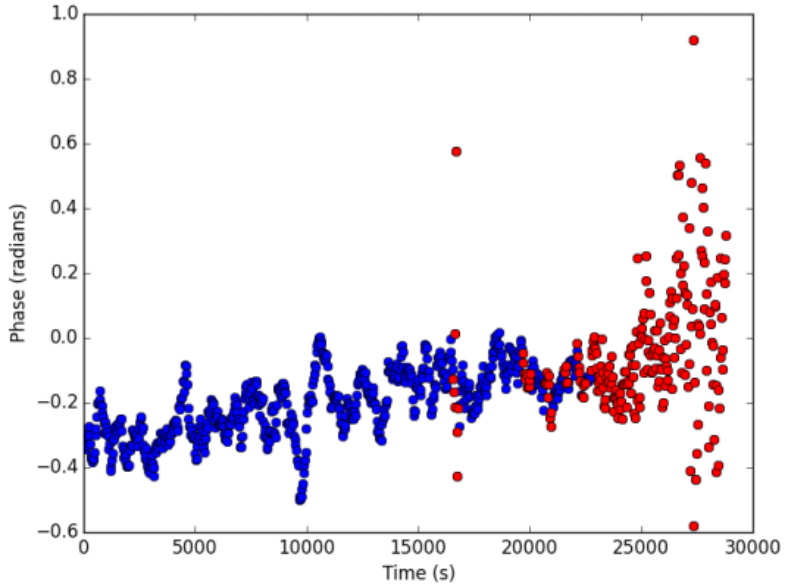

Figure 4.2: The red points show phase solutions for two nearby HBA core stations for an example of LoTSS dataset. The time periods of poor ionospheric conditions which cause the rapid large fluctuations of the phase solutions are flagged (Shimwell et al. 2017).

basis of their positions, the FoV is divided following the Voronoi diagram (Okabe et al. 2000), which allows to achieve gain solutions reasonably corrected for all points within every restricted area of the FoV considered. An example of the facet layout for a small region of the FoV of a LoTSS observation is shown in Figure 4.3.

Each calibrator facet undergoes to self-calibration cycles. The gain solutions found are used to calibrate the fainter sources. The clean components of such sources are added back from the previously created sky models. The subsequent facet is processed as well after that the improved clean components of the previous facet are subtracted from the uv-data. So the gain solutions are found for each facet. The procedure results into a reduction of the noise and it allows to obtain nearly thermal-noise limited images. An example of the improved quality of the images obtained from DDEs correction with direction-dependent calibration is shown in Figure 4.3.

All the previous steps are performed by an automated pipeline designed in order to make the calibration procedure efficient and functional (Shimwell et al. 2019).

Data imaging

The LOFAR data available for this Thesis work were previously calibrated by the LOFAR Surveys KSP Team through the processes outlined above. Starting from the calibrated uv-data, we produced radio images at different angular resolution, to recover both compact and extended sources.

The LOFAR data are imaged with the WSclean Software, an innovative imager implemented to manage the challenging data from new generation interferometers. Basically, the WSclean algorithm is designed to image the visibility data for large areas of the sky. In addition to the multi-scale and multi-frequency deconvolution, it is able to perform the w-stacking tecnique which takes into account the deviation of the array by a perfect plane during the cleaning (see Offringa et al. 2014 for the details of the software).

The goal of this Thesis work is the study of the diffuse large scale emission of the sampled clusters, therefore we created medium and low-resolution ($\sim 15''$ and $\sim 25''$, respectively) images of each of them. The small-scale structures are instead highlighted in high resolution images

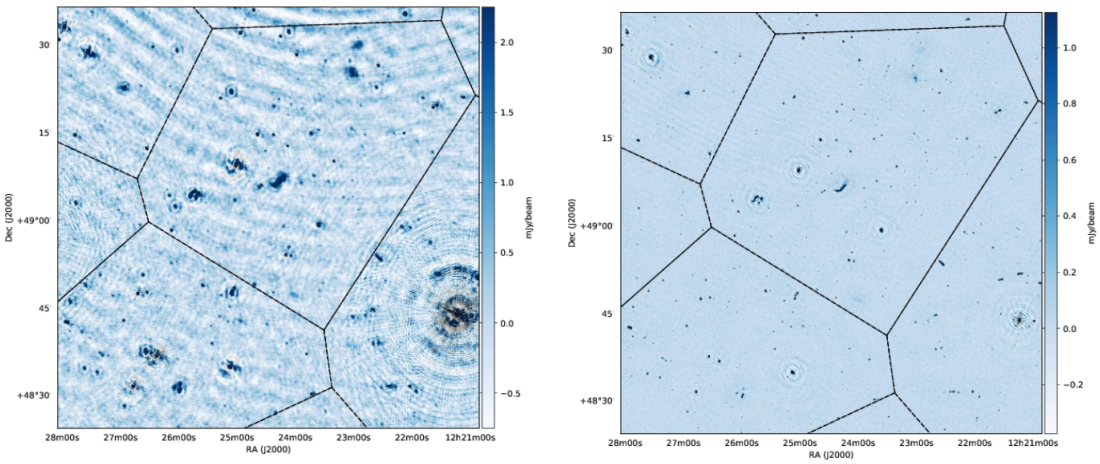

(a) (b)

Figure 4.3: Zoom of few facets of the LoTSS. The comparison of two figures show the effect of direction-dependent correction on the data. The black lines delineate the facets region (Shimwell et al. 2019). *Left*: Only time-independent calibration is applied on the data. *Right*: The same image after the DDEs correction.

($\sim 5''$) to determine the individual sources morphology. Finally, to point out the halo emission, we subtracted the discrete sources from the low resolution maps.

The imaging parameters are:

- The **pixel size** in arcseconds unit and the **image size** in pixel unit. Because of the Nyquist–Shannon sampling theorem, a reasonable part of the signal information is preserved if the main lobe of the beam of the image is sampled with a number of pixels from 3-3.5 to 5. The sizes (in arcseconds unit) of the FoV of interest[2] and the pixel sizes together determine the size of the image.

- The **uv-cut**. The resolution of the image is given by the inverse of the longest baseline of an array while the shortest baseline determine the largest recoverable scale. Using longer baselines allows to achieve high resolution image, but with lower sensitivity. This is the ideal case for the study of compact sources. With shorter baselines it can be detected the large scale diffuse emission. In this case the signal-to-noise ratio increases due to a denser sampling of the uv-plane as can be seen in Figure 4.4. On the other hand, the resolution results lower. In the creation of radio images, we can manipulated these effects by selecting the uv-cut parameter combined with the weights parameters (described above). This has implications on both resolution and sensitivity of the image.

  We set a value of uv-cut of 80λ for each image, ensuring that the large-scale emission (essentially from the Galaxy structures) does not contaminate the images.

- The weighting scheme. The visibilities are weighted in order to fiddle the non-uniform sampling of the uv-plane. In Figure 4.4 it can be appreciated the poorer sampling of the uv-plane from the remote stations of LOFAR. The **robust parameter** can be set adopting the so-call Briggs weighting scheme to give different weights to the baselines of

[2]The dataset are extracted from the HETDEX field of the LoTSS. The pointings dedicated to each cluster encompass an area of the order of degrees. Since the clusters cover a smaller area in the sky, the data for the imaging are reduced to a region which includes the cluster extension. We ran the imaging of the data within this area. The sources outside have been subtracted.

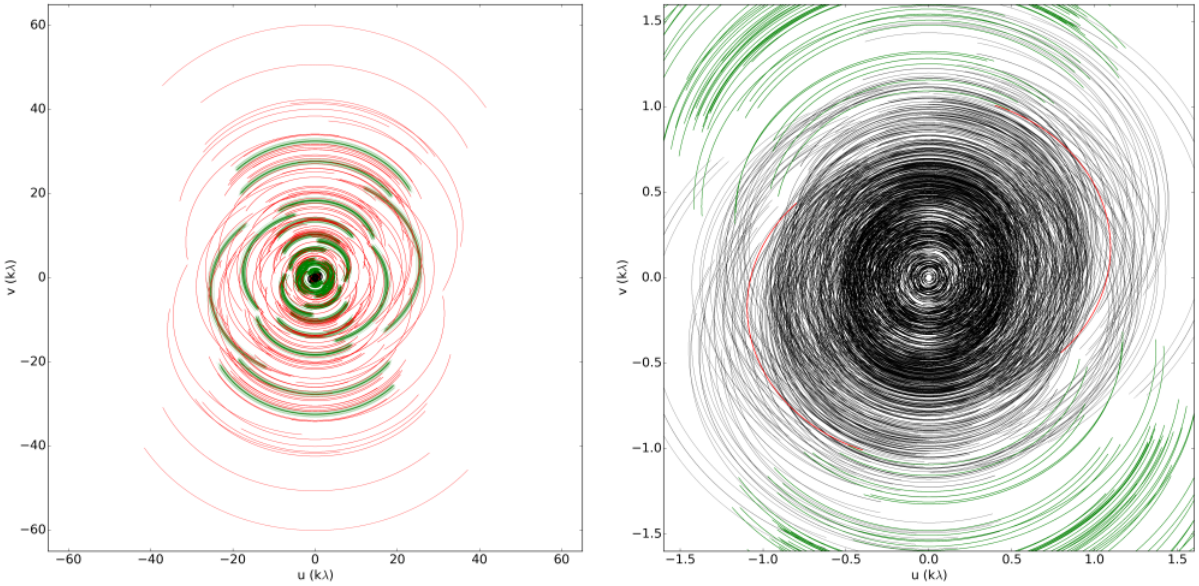

Figure 4.4: The typical uv-plane coverage of an 8h LoTSS observation excluding the international stations: in (a) it is shown the full uv-coverage while in (b) it is a zoom in the core. The different point colors marks the staton which recovers those uv-data (black for core stations, red for remote stations and green for a combination of the two). In (b) the denser uv-coverage allows a deep surface brightness sensitivity (Shimwell et al. 2017).

the interferometer and thus achieve different resolutions. The visibilities collected by the longer baselines are overweighted in order to take into account their lower density, and this leads to an increase of the resolution. Also the **uv-tapering** is fixed in the low resolution images to shape the dirty beam with a Gaussian function of a selected FWHM. This improves the sensitivity of the diffuse emission imaging process but reduces the resolution of the images.

We obtained the most suitable combination of these parameters to our aims after running WSclean several times. In each step, a new image is produced considering the previous output after have properly adjusted the parameters. An example for one of the targets is shown in Figure 4.5.

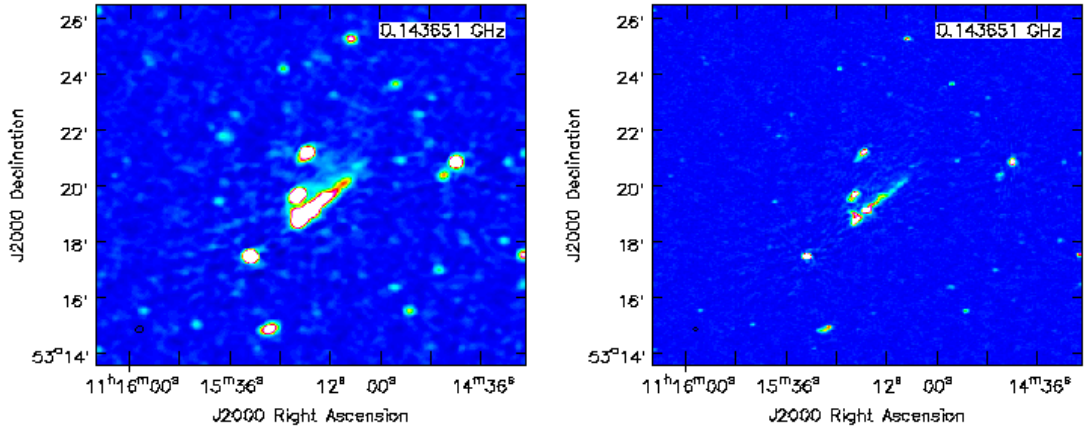

Figure 4.5: Two intermediate outputs of the imaging procedure of the RXC J1115.2+5320 cluster. The different combinations of parameters gives resolutions of $17'' \times 14''$ (on the left) and $8'' \times 5''$ (on the right).

In order to obtain high quality images, clean components were searched inside source masks provided as input to WScalen. In order to produce these masks, the sources are detected with the PYbdsm software in the image that we previously created without any box constrain. Once regions are acquired, they are stored in a mask. We manually edited masks to add eventually discrete sources undetected by PYbdsm. The manual inspection is performed using the viewer of the Common Astronomy Software Applications[3] (CASA).

In the two low resolution final images, we executed a subtraction of the discrete sources that allows to better characterize the diffuse radio emission from the ICM. The procedure consists of the following steps:

1. A very high resolution image is produced to detect the points source (Figure 4.6). It is produced excluding the baseline shorter than 3000-5000λ (depending on the case), sensitive to the diffuse emission and using, in particular, the information of the longest spacings corresponding to small angular sizes, namely to sources unresolved or marginally resolved with a beam of about $5''$.

   This is created by setting the clean algorithm with the uv-cut parameter to operate with the visibilities of longer baseline and then to exclude those of the diffuse emission. As done before, a first time the clean algorithm runs on the whole image and a second time it is employed a mask created with PYbdsm to clean only within boxes.

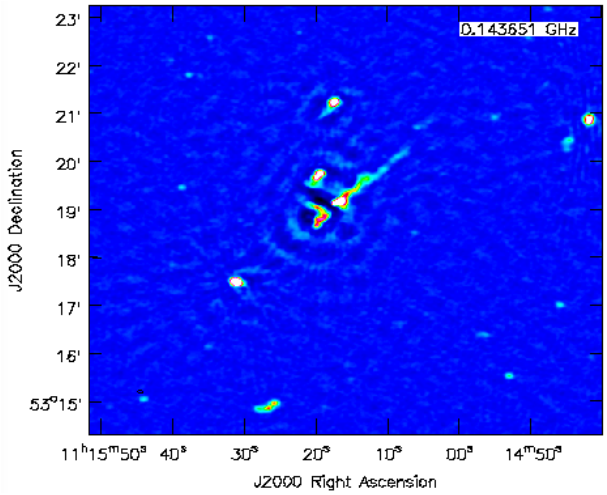

Figure 4.6: The high resolution image of the RXC J1115.2+5320 cluster realized to subtract the discrete sources visibilities from the dataset. The image has a resolution of $7'' \times 4''$ and it is obtained with an uv-cut of 5000kλ which corresponds to a largest recoverable scale of $41'$ ($\sim$ 240 kpc at the cluster redshift).

2. A column of the clean components stored in the model of the previous image is added in the original observations datasets. This is done with the `predict` option in WSclean, which allows to write in the `MODEL_DATA` column to an observation file.

3. Finally, the `DATA` column of the observation files is replaced with the `DATA-MODEL_DATA` column. The update of a data column (and the subtraction between visibilities) are allowed by the `taql` task.

4. The subtracted dataset are suitable to produce images containing the diffuse emission from RH only.

An example of the sources subtraction one of the targets is shown in Figure 4.7.

[3]https://casa.nrao.edu/

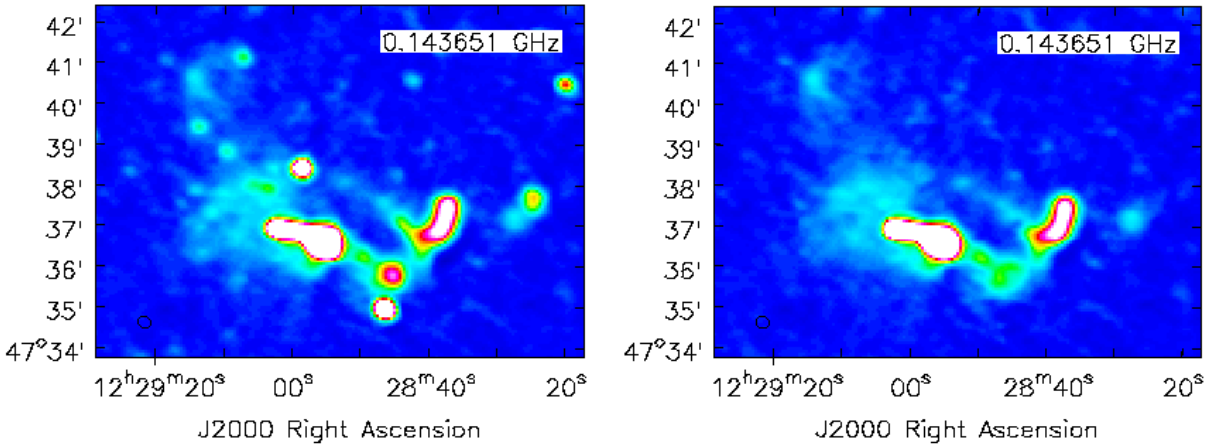

Figure 4.7: Abell 1550: on the left the sources are not subtracted, on the right the image is produced with the sources-subtracted dataset.

4.2 VLA data

The VLA data have been processed using the NRAO Astronomical Image Processing System[4] (AIPS)software. The pointings dedicated to the target together with those of the primary and secondary calibrators are selected and downloaded from the multi-sources dataset In the VLA data archive[5]. The data reduction consists of two phases: the a-priori calibration and the self-calibration. Once these are completed the imaging can be performed to realize the final radio images.

The a-priori calibration begins with the flagging of calibrators and target bad uv-data. This is interactively done through the tasks `WIPER`, `TVFLG` and `UVFLG`. Then, from the known flux density of the primary calibrator set with `SETJY`, the task `VLACALIB` measures the correction for all the antennas and the amplitude gain for both calibrators. Since the secondary calibrator flux density is unknown, the gains are found for a simulated flux density of 1 Jy and then a proportion is done through the task `GETJY` to found the proper value. The corrections are applied to calibrators and to the target with `CLCAL`.

At this point the a-priori calibration is completed and we split the calibrated uv-data of the target into a new uv-file. The radio images in AIPS are produced with the task `IMAGR`, which executes the clean algorithm. Also for VLA data imaging we set the proper fundamental parameters. After the first clean cycle, the self-calibration can be performed. In the a-priori calibration, only the phase-variations on time-scales of the order of the interval between two scans of the secondary calibrators are considered. That phase-solutions found and applied to uv-data, represent a first order approximation of the necessary corrections. In the self-calibration, the phase-solutions are calculated on the model given by the image produced by each clean cycle and are computed on the shorter time scale possible (allowed by the signal-to-noise ratio). Then a new image is produced with the task `IMAGR`. This procedure is performed iteratively, each times the self-calibration adopts as model the output of the previous clean cycle. When the data are self-calibrated the final imaging can be executed. Often, more than a single observation is available in the archive. It is possible than, combine them all in order to get a better image. The task used for the combination of the uv-data is `DBCON`.

In order to highlight the diffuse halo emission we subtract discrete sources to the dataset. Following the same procedure outlined for the LOFAR data, we produced an initial high reso-

[4]http://www.aips.nrao.edu/index.shtml
[5]https://archive.nrao.edu/archive/advquery.jsp

lution image which detects the compact sources by setting the suitable uv-range. In our case we used the same uv-range adopted for the LOFAR data. We carried out imaging and self-calibration routines, employing again the `IMAGR` and `CALIB` tasks. The clean components are collected within boxes defined interactively in the cleaning. Once the high resolution image has been created, its model, which contains the clean components of the discrete sources, was subtracted from the original dataset, and then the cleaning algorithm was run again to produce the final images with enhanced sensitivity to the extended emission.

Radio data analysis

The final images of the targets have been analyzed by means of the CASA viewer. We measured the σ_{rms}[6] of the images and determine the flux density, S_ν, of the RHs in a region within $3\sigma_{rms}$ contours. The area in which the RH emission is covered by central bright sources is initially excluded in the total flux density measure. The signal lost from these regions is calculated assuming the mean flux density measured from the diffuse emission. These flux density is rescaled to the missed area. This is added to the initial uncontaminated measure. The error on S_ν is given by:

$$\Delta S_\nu = \sqrt{(\sigma_{rms} \times N_{beam})^2 + (\sigma_{cal} \times S_\nu)^2} \tag{4.1}$$

where N_{beam} is the number of beams of the diffuse emission and σ_{cal} derives from the errors in the calibration procedure.

In order to examine the radio/X-ray connection in the clusters, if any data are available for 1.4 GHz frequency range, we get the flux density in this band from that at 144 MHz with:

$$S_{\nu_1} = S_{\nu_2} \left(\frac{\nu_1}{\nu_2} \right)^{-\alpha}.$$

If not observations exist at 1.4 GHz we assume a typical spectral index value for radio halos to compute the expected flux density at higher frequency. Finally the radio power at 1.4 GHz is given by:

$$P_{1.4\,\mathrm{GHz}} = 4\pi S_{1.4\,\mathrm{GHz}} D_L^2 (1+z)^{\alpha-1}$$

where D_L is the luminosity distance of the source, calculated according to the cosmology adopted.

4.3 Chandra data

For all the three targets are available X-ray observations of the Chandra X-ray telescope. The X-ray data reduction is carried out with the software CIAO v4.11[7] and with the calibration files contained in the Calibration DataBase CALDB v4.8.4.1. If more than one observation ID (obsID) could be retrieved for the target, we carried out the calibration and the imaging processes for each dataset separately and then we merged them with the `merge_obs` task.

Following the automatic procedures[8], the event data were recalibrated. The time interval affected by flares from soft protons were removed through the extraction and inspection of the light curves. These are created with the tool `dmextract` in the 0.5 - 7.0 keV energy range, from

[6] We assume the σ_{rms} as the average of flux density values taken in several background (that is free from discrete sources) areas.

[7] http://cxc.harvard.edu/ciao/

[8] http://cxc.harvard.edu/ciao/threads/createL2/

background regions (excluding sources). The flares and periods of anomalous levels of count rates were filter out with the `lc_clean` routine, designed by Maxim Markevitch.

In order to evaluate the proper background contribution, we adopted the blank-sky background data[9], re-scaling them to the current observation count-rates in the 9.0-12.0 keV band, where the effective area of the instrument is nearly zero, to take into account the changed particle background. The background templates are matched to the corresponding event files with the `reproject_events`. Images of the thermal emission are produced in the 0.5-2.0 keV band. To take into account the instrument effective area relative to each sky position, we corrected the images to the exposure map.

In the case of just one obsID available, we detected the point sources by running directly on this dataset the `wavedetect` tool. The selection was performed on the basis of a threshold, set to the default value of 10^{-6}. Furthermore, to characterize properly the discrete sources, the algorithm needs a point spread function (PSF) map, that is the size of the PSF at each pixel of an image. The output of `wavedetect` was inspected by eye to reject false detection and to add eventual sources which have not been identified by the software. The collected point-like emissions will be then excluded from the further analysis. In the cases of more obsID, the source detection was performed by using the combination of the PSF and exposure maps of each obsID to create an exposure-corrected PSF maps of the combined dataset. When the `wavedetect` runs on the merged images, it takes into account these maps. The missed discrete sources were identified by eye as before. All the sources were then removed to the final images.

The X-ray spectral analysis was performed with Xspec 12.10.1 (Arnaud 1996). The spectra were extracted within circular regions over the cluster emission. When possible, the radius of the extraction region was $\sim R_{500}$, which represents the ideal size for the our scientific analysis purpose (see Section 6.2.2). The spectral data were fitted in the 0.5-7.0 keV band with an absorbed thermal model for the ICM. We adopted the `PHABS` model to reproduce the galactic absorption at the source position, starting from the hydrogen column density averaged in the clusters direction. This has been retrieved with the tool[10] designed by Willingale et al. 2013. The thermal ICM is interpreted as a collisionally ionized and optically thin plasma, represented by the `APEC` model. This thermal bremsstrahlung emission model is defined by metallicity and temperature of the plasma, and by a normalization factor, which account for the angular distance to the source and the proton and electron number density of the gas. Initially we set the redshift and the hydrogen column density relative to each target, and the metallicity to a typical value of $0.3\,Z_{\odot}$, equal in the three cases. In a second fit, the latter was a free parameter and thus inferred from the spectral fit.

The temperature of the best-fit is adopted as global property of the plasma, under the assumption that it is constant within the region considered. Finally the X-ray luminosity is calculated from the best-fit model.

In addition to the spectral analysis we extracted surface brightness profiles. We use the software `PROFFIT v1.4`. Other than the calibrated (and merged) data images, the software requires the correspondent background and the exposure maps. The latter is necessary to correct the data for vignetting and to convert the surface brightness in physical units. The background maps allow to excluded from the data the background contribution.

The surface brightness profile was extracted within circular or elliptical regions through the `profile` or `ellipse` routine and it is given in photon/cm^2/s units. Once the profile was extracted, we re-bined the data to a minimum of 20 counts per bin in order to achieve a sufficient statistic in each bin. Then we fitted the data with a β-model, available in `PROFFIT`, described by (Cavaliere & Fusco-Femiano 1976):

[9] http://cxc.harvard.edu/ciao/threads/acisbackground/
[10] https:www.swift.ac.ukanalysisnhtotindex.php

$$S(r) = S_c[1 + (r/r_c)^2]^{-3\beta+0.5} + \text{const} \tag{4.2}$$

where the r_c is the core radius and S_c is the surface brightness within the r_c radius. A deprojected profile can be obtained through the `deproject` routine. The algorithm assumes spherical symmetry and calculates the 3D surface brightness on a series of concentric shells centered in the same pixel of the 2D profile. The deprojection step is preparatory to extract the 3D density profile starting from the surface brightness in each shell. It is achieved by the `density` task in units of proton number density profile. From the parameters of these, we easily deduce the electron one, since in a fully ionized plasma it is $n_e = 1.21 n_H$. Finally, under the assumption of isothermal ICM, it was performed the pressure density profile from:

$$P(r) = 2 n_e(r) kT.$$

Chapter 5

Targets selection and analysis of radio and X-ray observations

5.1 Targets selection

We selected a sample of clusters detected in SZ (Section 1.1.2) and already observed with LOFAR at the time of the Thesis. The reason for the SZ selection is related to fair the estimate of the cluster mass, available for the great majority of these clusters and which is an essential parameter in the physics of non-thermal components (Section 2.2.1). The selection started with the sample contained in the SZ Meta-Catalogue SZ-database[1] which consisting of 2690 clusters or candidates. The catalogue matches microwave observations of the South Pole Telescope (SPT), the Atacama Cosmology Telescope (ACT) and the Planck satellite Telescope (PT); in addition, minor contributions come from the Combined Array for Research in Millimeter-wave Astronomy (CARMA) and the Arcminute Microkelvin Imager (AMI). The clusters in the catalogue are detected through the SZ effect observed in the CMB spectrum. The cluster masses are derived following the $Y_{500} - M_{500}$ correlation (see Section 1.6).

The position of the SZ-detected clusters, downloaded from the website, was superimposed to the LoTSS observation through the software Aladin, an interactive visualization tool that allows to display multi-wavelength data. 164 clusters out of the initial 2690 ones in the sample fall in the region observed from the LoTSS at the time when the Thesis work started. Among these, we initially excluded those for which the SZ-catalogue did not provide redshift and mass measurements.

We verified the presence of VLA archival data at 1.4 GHz that could be useful to derive the spectral properties of the radio sources. We also checked if the GCs were already studied in the radio band and if the extended emission, possibly present, was classified as relic, RH or radio MH. To this, we employed a recent database, GalaxyClusters.com[2], designed at the Observatory of Hamburg, which collects the information of almost all the diffuse sources in galaxy clusters available in the literature.

The X-ray data of clusters have been searched in the High Energy Astrophysics Science Archive Research Center (HEASARC), which collects data of high energy observations carried out with different instruments. In our case, we restricted the search to observations performed with the Chandra, XMM-Newton and Rosat satellites. If there were no data for the candidates or, if the data are available, the exposure time is less than 5 ks, the GC have been excluded.

After the search, the final sample was reduced to less than 60 members with known mass and archived X-ray observations. 12 of them are high priority targets being in the HETDEX

[1] http:szcluster-db.ias.u-psud.frsitoolsclient-userSZCLUSTER_DATABASEproject-index.html
[2] https://galaxyclusters.hs.uni-hamburg.de/

Spring Field of the LoTSS. For this Thesis we selected 3 out of these targets (Table 5.1): two targets, Abell 1622 and RXCJ1115.2+5320, were never studied in the radio band while in Abell 1550 a radio halo was previously published in Govoni et al. 2012. All of them were observed through the Chandra X-ray telescope. Only for Abell 1550, VLA data at 1.4 GHz are available.

Table 5.1: Summary of the targets characteristics.

Name	z	M_{500}	Coordinates		kpc/″
		$(10^{14} M_{\odot})$	R.A.	Dec.	
Abell 1550	0.254	$5.88^{+0.38}_{-0.42}$	12h28m53.760s	47°36′44.283″	3.956
RXCJ1115.2+5320	0.4699	$7.55^{+0.49}_{-0.52}$	11h15m10.800s	53°19″38.998′	5.901
Abell 1622	0.283	$4.38^{+0.50}_{-0.52}$	12h49m41.279s	49°52′18.478″	4.276

Notes. The mass and the redshift are taken from the SZ-database (Planck Collaboration et al. 2016). The angular to linear conversion is obtained assuming a flat cosmology with $H_0 = 70\,\mathrm{kms}^{-1}\mathrm{Mpc}^{-1}$, $\Omega_M = 0.3$, $\Omega_\Lambda = 0.7$.

In the following we describe the three targets and main results obtained from the radio and X-ray measurements.

5.2 Abell 1550

Abell 1550 is a dynamically disturbed cluster located at $z = 0.254$. The X-ray observation of the cluster in the ROSAT All-Sky Survey (RASS) revealed a gas distribution which extends roughly in NS, but with some emission in perpendicular direction (Govoni et al. 2012, Figure 5.1). The X-ray luminosity measured in the 0.1 - 2.4 keV is 3.51×10^{44} erg/s (Bohringer et al. 2000).

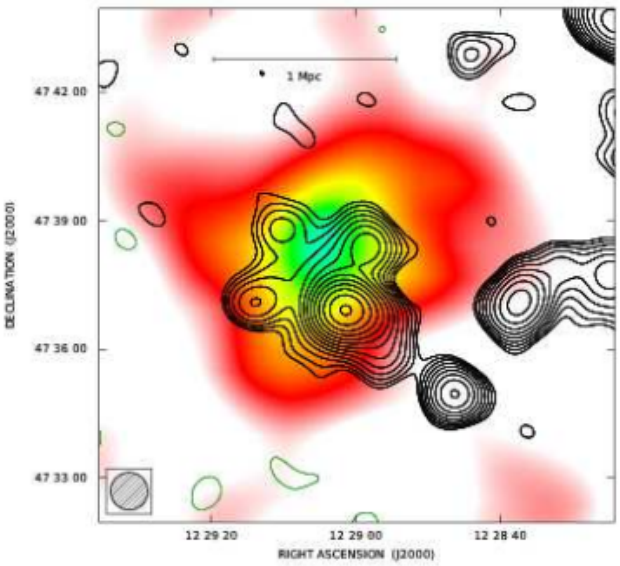

Figure 5.1: Abell 1550 X-ray image in 0.1-2.4 keV energy range from RASS, with overlaid the radio contours at 1.4 GHz from VLA in D configuration. The beam size of the radio image is $53'' \times 53''$. The X-ray image is smoothed to a resolution of $45''$ (From Govoni et al. 2012).

An extended low surface brightness radio emission in the central region of the cluster was discovered by Govoni et al. 2012 and classified as RH. A central radio galaxy contributes to a large fraction of the emission from the cluster making the definition of the properties of the

diffuse emission rather difficult. An optical image from the SDSS, shown in Figure 5.2, reveals the optical counterpart of the central radio source.

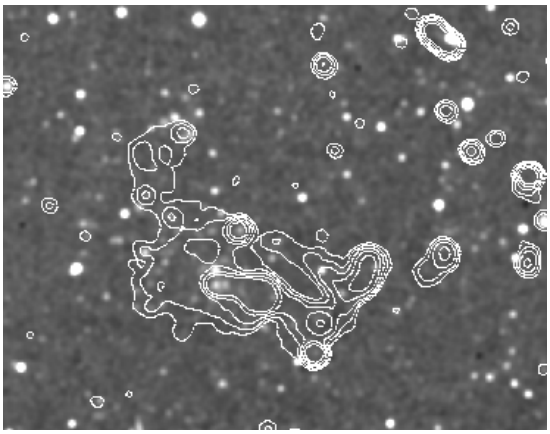

Figure 5.2: The SDSS image of the Abell 1550 field. The radio contours taken from the LOFAR image in Figure 5.4 are overlaid on the optical image (the radio image parameters are reported in Table 5.2).

In order to separate the contribution of discrete sources from the RH we reprocessed the VLA archived data at 1.4 GHz analyzed by Govoni et al. 2012. The main goal was the analysis of the cluster scale emission in the low frequency radio band with the 144 MHz LOFAR data from the LoTSS and its comparison with the higher frequency images. Further we analyzed the X-ray emission of the cluster observed with Chandra to study the radio to X-ray connection.

5.2.1 Radio data analysis

LOFAR The calibrated LOFAR datasets of Abell 1550 consists of 4 pointings. From the total area of the observation, a region of $\sim 43' \times 43'$ containing the cluster emission was extracted and re-calibrated as outlined in Section 4.1. Each LoTSS pointing consists in a 8hr observation bookended by 10 minutes scans on the flux density calibrator. Following the procedure described in Section 4.1, we first produced the total flux density images of the cluster at three resolutions. The imaging parameters adopted are reported in Table 5.2 and the relative images are shown in Figure 5.3, Figure 5.4 and Figure 5.5. The inner uv-cut of 80λ provides a largest angular scale of $43'$ at the cluster redshift and allows to reduce the sensitivity to the large-scale (foreground) Galaxy emission.

Table 5.2: Imaging parameters adopted for the Abell 1550 images.

Figure	Beam size ($'' \times ''$)	Im. size (pixel $\times$pixel)	Pixel size ($''$)	Robust	Taper ($''$)	σ_{rms} (μJy $\cdot$ beam^{-1})
Figure 5.3	27×23	560×560	5.0	-0.25	15	95
Figure 5.4	20×18	700×700	4.0	-0.25	10	140
Figure 5.5	10×6	1870×1870	1.5	-0.25	n.a.	73
Sources subtraction						
	27×23	560×560	5.0	-0.25	15	152
Figure 5.6	20×18	700×700	4.0	-0.25	10	121

Notes. N.a. is "not applied".

The second step of the imaging process consists of the discrete source subtraction. After producing the very high resolution image and subtracting the model of this to the original

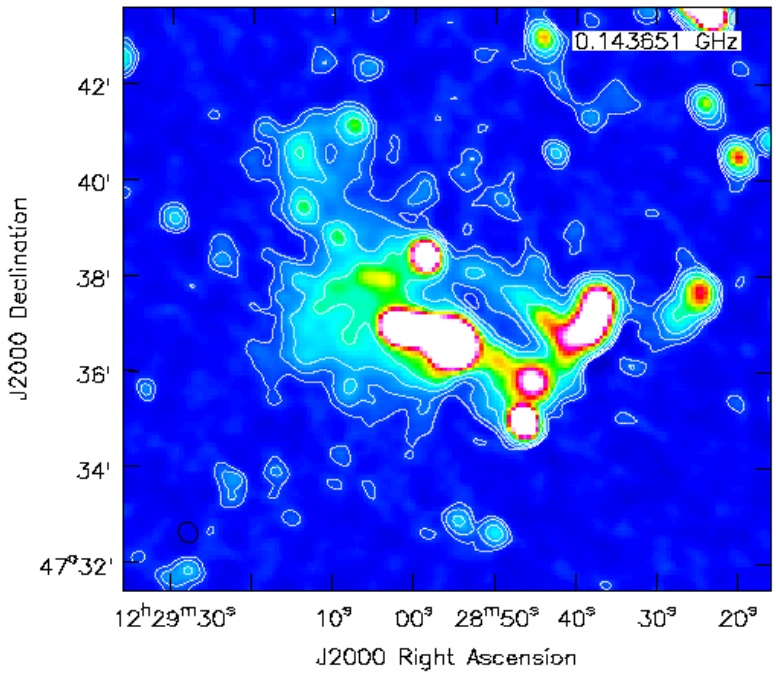

Figure 5.3: Abell 1550 LOFAR image at the low resolution. The contour levels are spaced of a factor 2 from $3\sigma_{rms}$. See Table 5.2 for the image parameters.

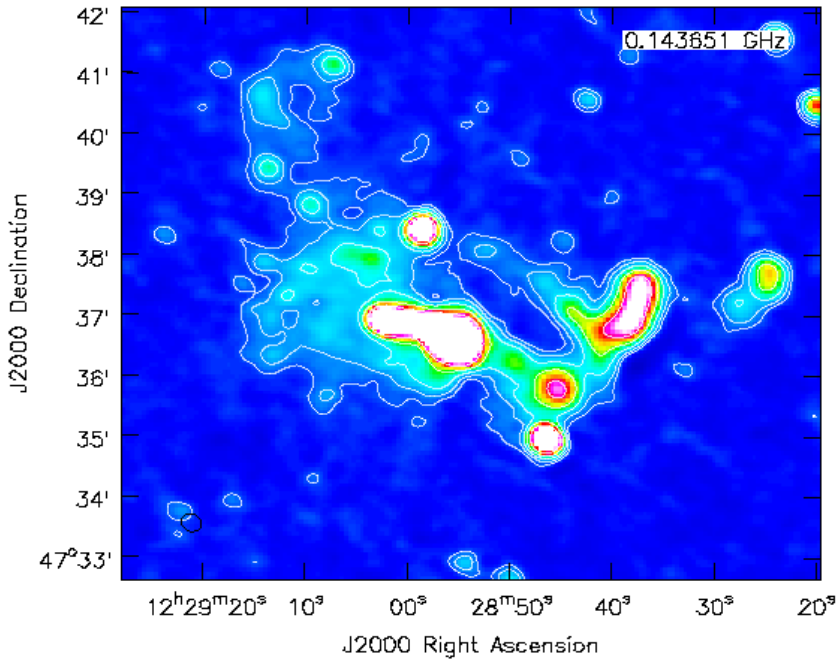

Figure 5.4: Abell 1550 LOFAR image at the medium resolution. The contour levels are spaced of a factor 2 from $3\sigma_{rms}$. See Table 5.2 for the image parameters.

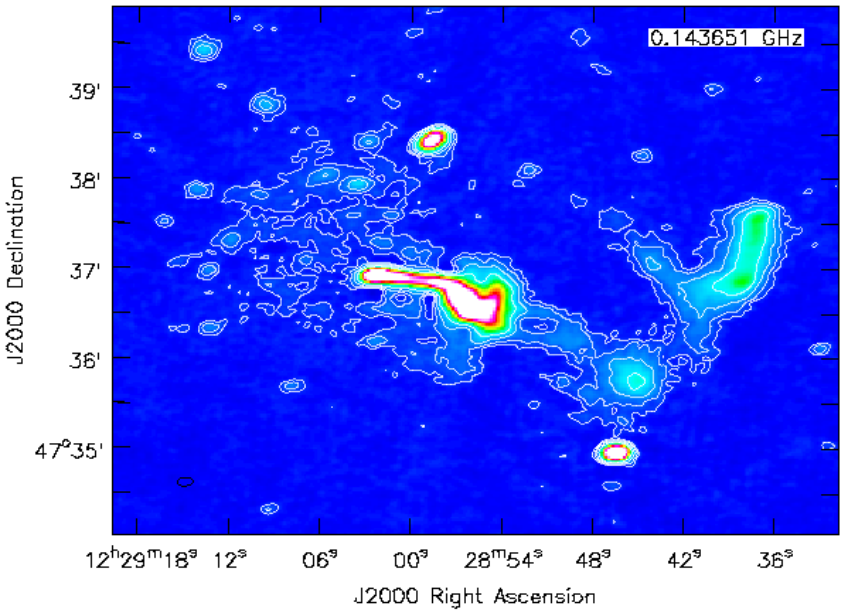

Figure 5.5: Abell 1550 LOFAR image at the high resolution. The contour levels are spaced of a factor 2 from $3\sigma_{rms}$. See Table 5.2 for the image parameters.

datasets (described in Section 4.1), we created the subtracted images. The first time we ran this procedure, both low and medium resolution image showed several artifacts, mostly in the central region of the FoV. This was due to the clean components of the central bright source that were initially subtracted out of the datasets. For this reason, we chose to include these components: the correspondent region was excluded in the mask with which we made the 3000λ image. When sources like the HT radio source in Figure 5.5 are in the field, the subtraction of point source is often difficult, since the emission continuously cover a very wide range of spatial frequencies in the visibility domain. Despite trying a number of combination of parameters for the source subtraction, we could not obtain a fair image, since sidelobes of the partially subtracted tail corrupted the quality of the final image. Therefore, we decide to preserve the HT emission in the point source subtracted dataset. This allowed to obtain a fair image. In the subsequent analysis, the sky region covered by the HT emission was masked out, and the contribution to the halo emission was corrected by extrapolating the surface brightness of adjacent regions.

The parameters of the imaging are defined in Table 5.2. We show in Figure 5.6 the sources-subtracted image at the medium resolution, which is taken as reference for the major part of the subsequent analysis.

VLA We re-analyzed the VLA archival data at 1.4 GHz. The observations have been carried out in C and D configurations. The two configurations differs in the distribution of the antennas in the interferometer: extended configurations (A, B) provide the highest resolution but are insensitive to diffuse emission while compact configurations (C, D) provide shorter baselines that are ideal to detect extended sources, although they have lower resolutions. The frequency range of both the observations are centered at 1.4 GHz (that is the L-band of the VLA interferometer) and involves the frequency range from 1.365 GHz to 1.435 GHz. The main characteristics of the observations are reported in the Table 5.3.

Following the procedure outlined in Section 4.2 we downloaded the dataset of target and calibrators pointings. The primary calibrator, common for both the observations, is 1331+305. The secondary calibrators are 1219+484 in the D dataset and 1400+621 in the C dataset . We

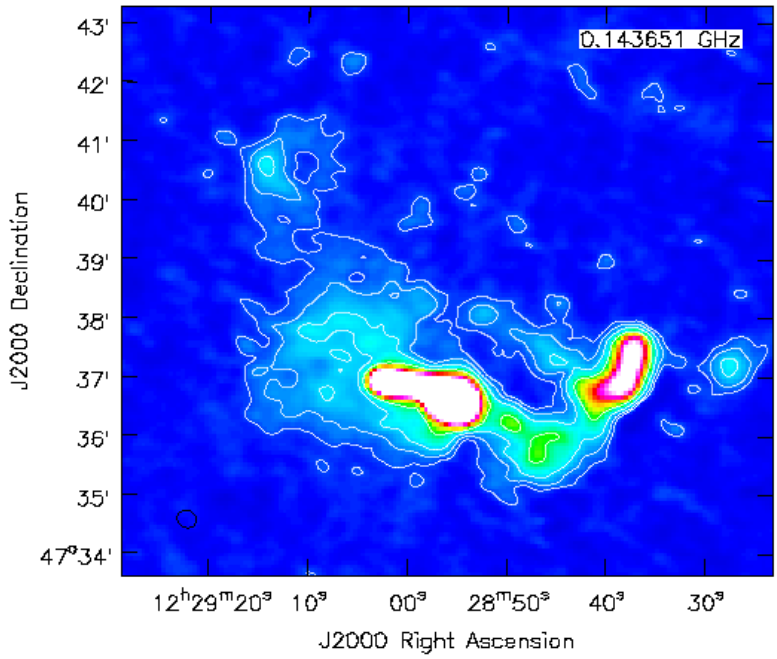

Figure 5.6: Abell 1550 radio emission subtracted at 144 MHz. The image has a beam size of $20'' \times 18''$. The contour levels are spaced of a factor 2 from $3\sigma_{rms}$ where $\sigma_{rms} = 121\,\mu\text{Jy} \cdot \text{beam}^{-1}$.

Table 5.3: Summary of the VLA observations at 1.4 GHz on the target Abell 1550.

Conf.	Obs.Time	Pointing center		Date	Program
	(min)	RA	DEC		
D	15	12h29m19.2s	47°37′58.0″	1995-Mar-15	AM0469
C	75	12h28m57.7s	47°37′58.0″	2003-Jan-03	AM0702

processed the data with the a-priori calibration, the self-calibration and a preliminary imaging for both the C and D datasets.

The data from the two array configurations were combined to achieve longer integration time and increase the sampling of the uv-plane that corresponds to gain sensitivity. Due to the offset between the pointing directions we did not run the task `DBCON` directly on the datasets. To bypass the displacement, we used another approach. For each dataset we imaged two exactly overlapping fields: in the first, the clean was performed in the central region only, while in the second field all the confusing sources were cleaned. The second image only was subtracted (with task `UVSUB`) out of each dataset. This allowed to overcome the different flux densities measured in the two datasets owing to different primary beam attenuation for sources out of the central region of the pointing, arising from the forementioned offset (see also Table 5.3). Once the subtraction has been performed, the two datasets were combined with the task `DBCOM`, applying in this phase the offset correction with the task `UVFIX`. In the resulting concatenated dataset, only the visibilities of the central field are stored. This box corresponds to the central observation region for both the array configuration. Since in this direction the instrument reaches its best performance, the correction of the offset does not cause significant lack of signal.

This dataset was used to create images of the diffuse emission only. The compact sources identified in C configuration data were subtracted. We produced the 3000λ image by manually selecting the boxes in which clean components have to be searched for. In order to accurately recognize all the sources which contaminate the halo emission, we took into account the optical SDSS and the high resolution LOFAR images of the same area. The tail of the central radio galaxy is also included in these boxes. The final subtracted image is shown in Figure 5.7.

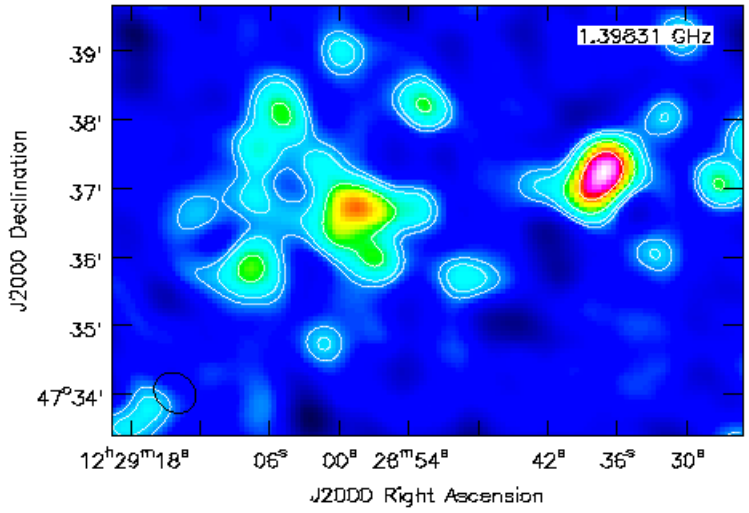

Figure 5.7: The Abell 1550 image at 1.4 GHz. The map has a σ_{rms} of $83\,\mu\text{Jy}\cdot\text{beam}^{-1}$ and a beam size of $40'' \times 33''$. The contours are drawn at 3σ, 6σ, 12σ spaced by a factor 2.

The flux density within $3\sigma_{rms}$ measured in the $20'' \times 18''$ LOFAR image (Figure 5.6) is $S_{144\,\text{MHz}} = 174 \pm 24\,\text{mJy}$ (calculated removing the bright sources contributes, see Section 4.1), while the one obtained from the VLA image is $S_{1.4\text{GHz}} = 4.95 \pm 1.3\,\text{mJy}$. From the latter we infer a power radio of $(8.54 \pm 2.77) \times 10^{23}$ W/Hz at 1.4 GHz. The spectral index α is easily deduced with:

$$\alpha = \frac{\log\left(\frac{S_1}{S_2}\right)}{\log\left(\frac{\nu_2}{\nu_1}\right)} \pm \left|\frac{1}{log\left(\frac{\nu_1}{\nu_2}\right)}\right| \sqrt{\left(\frac{\sigma_{S_1}}{S_1}\right)^2 + \left(\frac{\sigma_{S_2}}{S_2}\right)^2}$$

where ν_1 and ν_2 are 144 MHz and 1.4 GHz respectively. With the values of S_ν reported above it turns out that the extended emission has $\alpha = 1.6 \pm 0.2$. This qualifies Abell 1550 as a candidate ultra-steep spectrum RH. So far only about 10 RH with very steep spectrum are known (van Weeren et al. 2019). As discussed in Section 2.2.1 the discovery of RH with very steep spectrum is crucial because they are important tests for re-acceleration models. Indeed a radio spectrum $\alpha = 1.6$ would require a spectrum of the emitting electrons $\delta = 4.2$ implying that an untenable energy budget (dominated by electrons at lower energies) is associated with these particles. In order to circumvent this problem a break (at energies $\sim$ GeV) is required in the spectrum of electrons population and this is interpreted as the evidence for the interplay between radiative losses and turbulent re-acceleration (see Brunetti & Jones 2014 for a review). Re-acceleration models predict that a large fraction of the RH associated with clusters with $M_{500} = 4 - 7 \times 10^{14} M_\odot$ should be steep spectrum and indeed Abell 1550 has a mass in this range.

5.2.2 X-ray data analysis

The Chandra data of Abell 1550 (obsID 11766) were taken with ACIS-S operating in VFAINT mode. The ACIS-S configuration consists of one chip pointed in the direction of the cluster. Unfortunately the cluster emission covers a projected area larger than the CCD area then part of the cluster emission is undetected.

We calibrated the data and produced the image in the 0.5-2.0 keV band (Figure 5.8) following the prodecure outlined in Section 4.3.

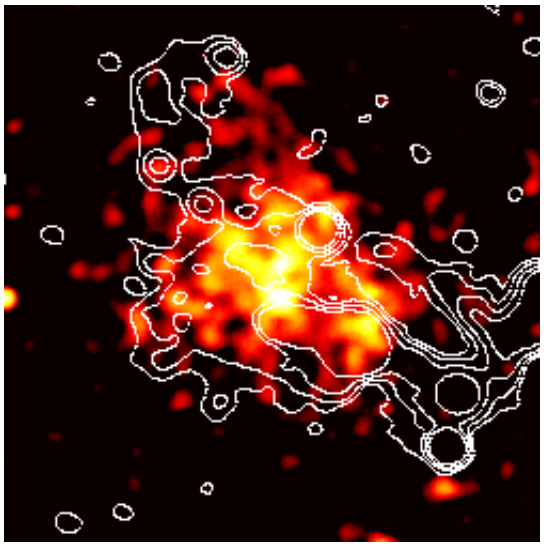

Figure 5.8: Abell 1550 LOFAR contours superposed on the Chandra 0.2-5.0 keV image. The X-ray image is convolved with a Gaussian of $\sigma = 15''$. The LOFAR image has a resolution of $20'' \times 18''$. Radio contour levels are distanced of a factor 2, starting from $3\sigma_{rms}$, where σ_{rms} is 121 μJy $\cdot$ beam^{-1}.

To infer the ICM properties, the spectrum was extracted in a region within a radius of 4 arcmin from the cluster center, that is the maximum area that can be reached with the size of the CCD. The radius of 4 arcmin corresponds to $\sim 0.8 R_{500}$ for Abell 1550 cluster, where R_{500} is ~ 1.24 Mpc (5.22 arcmin at the cluster redshift).

Following the method outlined in Section 4.3 we modeled the spectrum as an absorbed thermal plasma. The resulting best-fit parameters are reported in Table 5.4 and shown in Figure 5.17. For this cluster the measure of the metallicity from the spectral analysis have not been performed, given the poor statistics of the data.

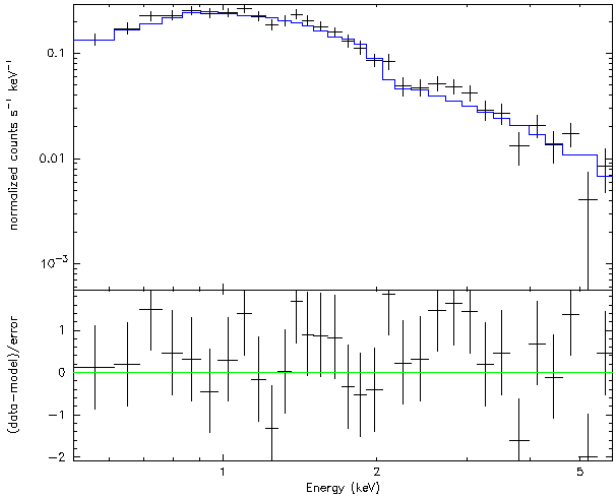

Figure 5.9: X-ray spectral fitting of Abell 1550 (the parameters are reported in Table 5.4). The best-fit model is shown with the blue lines. In the bottom panel are shown the residual.

Table 5.4: Best-fit parameters from the spectral analysis of Abell 1550 cluster.

	PHABS*APEC
$N_{\rm HI}$ (10^{-20} cm^{-2})	1.07
kT (keV)	$6.01^{+0.75}_{-0.68}$
Abundance	0.3
Redshift	0.254
norm (10^{-3})	$3.08^{+0.08}_{-0.08}$
L (10^{44} ergs^{-1})	$3.72^{+0.17}_{-0.06}$
χ^2/ d.o.f	0.98

Notes. The luminosity values are measured in the 0.1- 2.4 keV band. All the measures has a confidence level of the 68%.

We extracted the surface brightness profile from a circle with radius of 3.58 arcmin (850 kpc) from about the cluster center (RA=12°29′02.18″, DEC= 47°37′43.58″). In order to obtain a good statistics we rebined the data to 25 counts per bin. The surface brightness profile is fitted with a β-model defined by the Eq. (4.2). We found (with a 68% confidence level): $\beta = 0.80^{+0.26}_{-0.14}$, a central surface brightness of $2.13^{+0.69}_{-0.45}$ cts s^{-1}arcmin^2 and a core radius of $r_c = 1.059^{+0.054}_{-0.054}$ arcmin, the relative model is shown in Figure 5.10.

In order to determine the $P_{1.4} - L_X$ relation consistently with the previous studies, we need to infer the X-ray luminosity inside a radius of R_{500} (while we achieved the one within $0.8R_{500}$ from the spectral analysis). For the purpose, we extrapolated a flux estimation until R_{500} with the `flux` task of `PROFFIT`. This value is computed assuming a model (in our case the β-model) and it is given in counts/sec unit. To convert this flux in physical units and to report the value to the effective area of Chandra, (the one relative to the obsID 11766 was the cycle 11)[3] we used the PIMMS v4.9[4] tool. The resulting flux is given in erg/cm^2/s. Finally, the luminosity

[3]It is necessary to take into account the observation cycle number since the effective area and then the quantum efficiency of the CCD decrease with time due to sedimentation of material on the detector.

[4]http:cxc.harvard.edu/toolkit/pimms.jsp

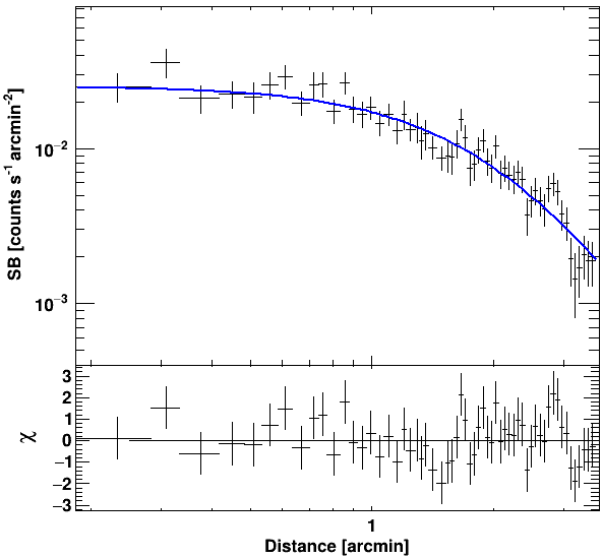

Figure 5.10: X-ray surface brightness profile of Abell 1550 in the 0.5 - 2.0 keV band. It is extracted in a circle with a radius of 3.58 arcmin. The fit has $\chi^2/\text{d.o.f} = 1.06$. The best-fit model is shown with the blue line. The bottom panel reports the residuals.

is $\sim 4.2 \times 10^{44}$ erg/s. Since the luminosity represents a global property of the cluster, the estimation derived from a detector unable to recover all the cluster emission may be inaccurate, and represent a lower limit.

5.3 RXC J1115.2+5320

No detailed studies of this cluster in the radio and X-rays have been published so far. It is located at a redshift $z = 0.4699$ and has a mass $M_{500} \sim 7.55 \times 10^{14} M_{\odot}$ (Planck Collaboration et al. 2016). In Figure 5.11 it is shown the SDSS image of the area covered by the cluster.

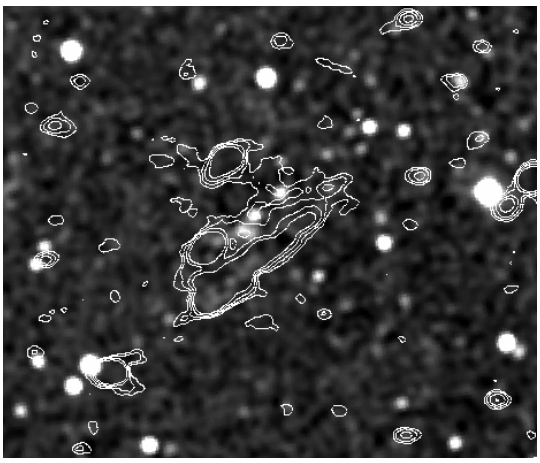

Figure 5.11: The RXC J1115.2+5320 optical image observed in the SDSS. The overlaid radio contours are taken from the medium resolution image (Figure 5.13, the image parameters are summarized in Table 5.5) .

5.3.1 Radio analysis

We carried out the imaging of RXC J1115.2+5320 following the procedures in Section 4.1. The target involves two pointings of the LoTSS. The extracted field covers a region of $\sim 43' \times 43'$. The survey operative mode provides 8 hr of observation for the target and 10 minutes for the calibrator. The central frequency of the observation is 144 MHz. The parameters indicated in Table 5.5 have been used for the final images. The resulting images are shown in Figure 5.12, Figure 5.13 and Figure 5.14. At the redshift of the cluster, the uv-cut set to 80λ determines a largest angular scale of $43'$ ensuring the exclusion of the contribution from the Galactic emission.

Table 5.5: Imaging parameters utilized for the RXC J1115.2+5320 images.

Figure	Beam size ($'' \times ''$)	Im. size (pixel ×pixel)	pixel size ($''$)	Robust	Taper ($''$)	rms (μJy · beam^{-1})
Figure 5.12	20×19	360×360	4.5	-0.25	10	167
Figure 5.13	15×10	540×540	3.0	-0.25	5	111
Figure 5.14	8×5	1080×1080	1.5	-0.5	n.a.	90
Sources subtraction						
Figure 5.15a	15×10	540×540	3.0	-0.25	5	104
Figure 5.15b	20×19	360×360	4.5	-0.25	10	150

Notes. N.a. is "not applied".

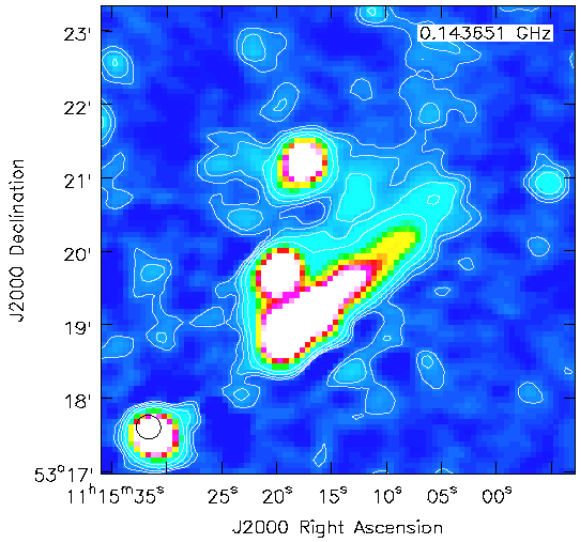

Figure 5.12: RXC J1115.2+5320 cluster 144 MHz image at the low resolution obtained with the imaging parameters reported in Table 5.5. The contours are spaced by a factor 2 starting from $3\sigma_{rms}$.

The very high resolution image produced to carry out the source subtraction has been obtained with an inner uv-cut of 5000λ corresponding to a recoverable scale of ~ 240 kpc at the cluster redshift, suitable for the detection of the discrete sources. The low and the medium resolution images after the subtraction are shown in Figure 5.15. The subsequent analysis of the radio emission is carried out on the medium resolution sources-subtracted image (Figure 5.15b). The 144 MHz images of the cluster reveal a low surface brightness source which extends on large scales. It embeds individual extended radio sources, like a HT emission whose projected linear size reaches about 700 kpc (inferred from the high resolution LOFAR image shown in Figure 5.14).

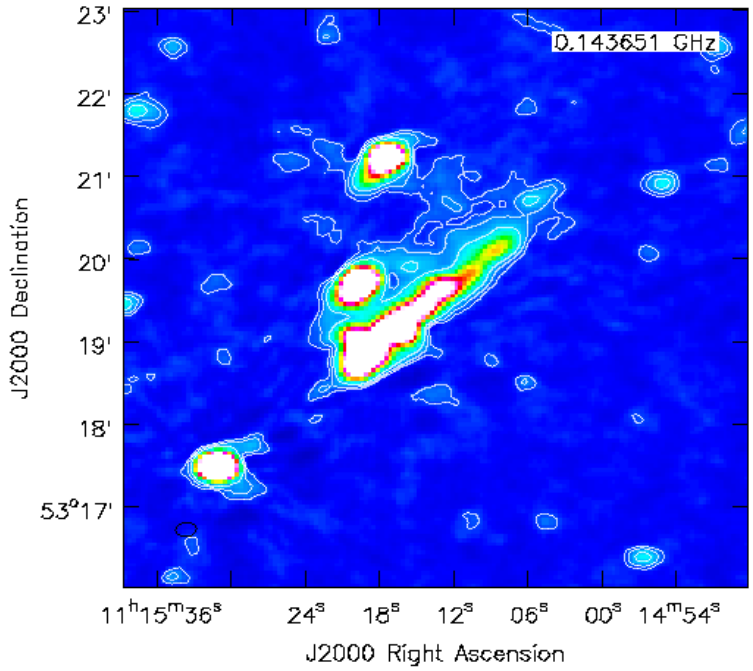

Figure 5.13: RXC J1115.2+5320 cluster 144 MHz image at the intermediate resolution obtained with the imaging parameters reported in Table 5.5. The contours are spaced by a factor 2 starting from $3\sigma_{rms}$.

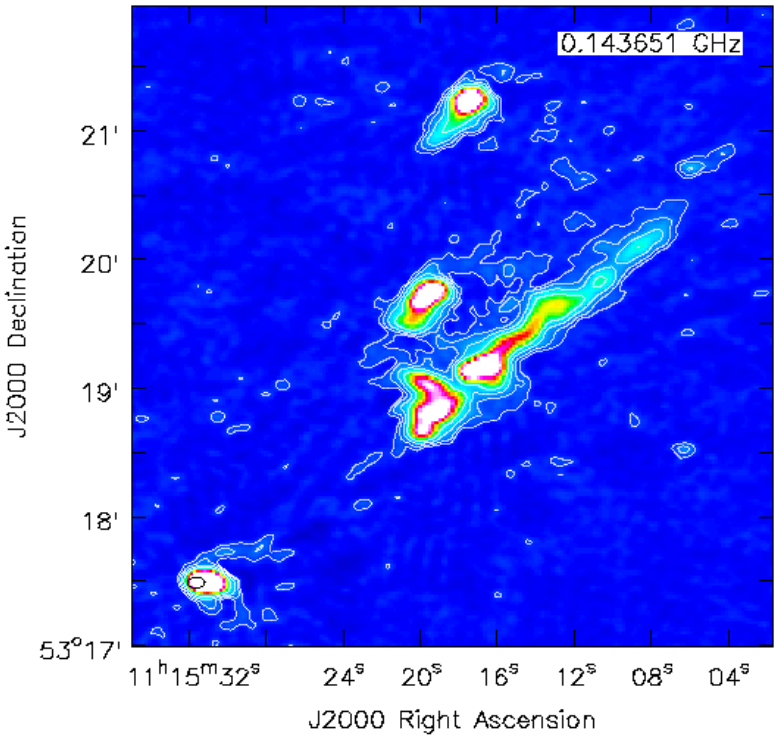

Figure 5.14: RXC J1115.2+5320 cluster 144 MHz image at the high resolution obtained with the imaging parameters reported in Table 5.5. The contours are spaced by a factor 2 starting from $3\sigma_{rms}$.

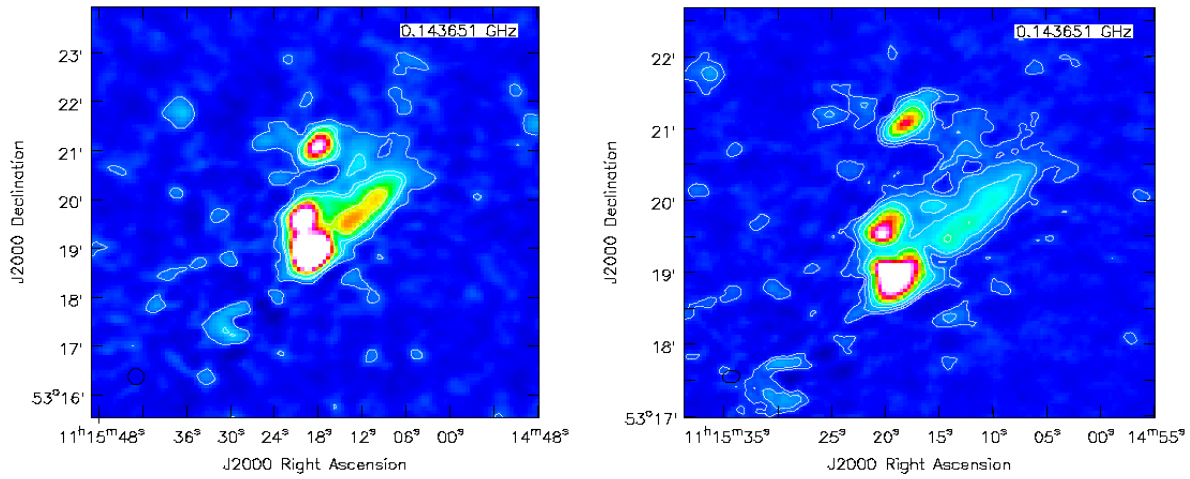

(a) (b)

Figure 5.15: The point sources-subtracted images of RXC J1115.2+5320. On the left the low resolution image and on the right the intermediate resolution image. The parameters are indicated in Table 5.5. The contour levels in both are drawn starting from $3\sigma_{rms}$ and spaced by a factor 2.

The flux density at 144 MHz of the diffuse emission measured from the $3\sigma_{rms}$ contour levels of the medium resolution image (Figure 5.15b) is $S_{144\,\mathrm{MHz}} = 63 \pm 5$ mJy. The presence of the bright central object was taken into account by masking its emission and replacing the flux density in this area with a mean flux density as outlined in Section 4.1. Since there are no literature studies about RXC J1115.2+5320 at other radio frequencies, we assumed a spectral index of $\alpha = 1.3$ to estimate the radio power at 1.4 GHz. This results $(2.87 \pm 0.97) \times 10^{24}$ W/Hz.

5.3.2 X-ray analysis

The archival Chandra data of RXC J1115.2+5320 consist of three observations ID (3253, 5008 and 5350). The target was observed for a total exposure time of 35 ks with the ACIS-I instrument in VFAINT mode. The datasets are processed as outlined in Section 4.3, and merged together to produce a single image of the cluster. From the images obtained in the X-band with the Chandra data (Figure 5.16) the cluster appears as a dynamically active system. The X-ray emitting gas presents a slightly elongated morphology in the SE-NW direction.

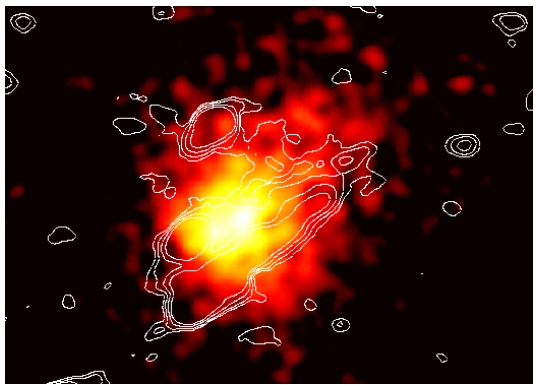

Figure 5.16: RXCJ1115.2+5320 Chandra smoothed image in the 0.2-5 keV band overlaid with the radio contours. The radio contours are taken from the medium resolution image with a beam size of $15'' \times 10''$, they are spaced of a factor 2 from $3\sigma_{rms}$, where σ_{rms} is 111 $\mu\mathrm{Jy} \cdot \mathrm{beam}^{-1}$.

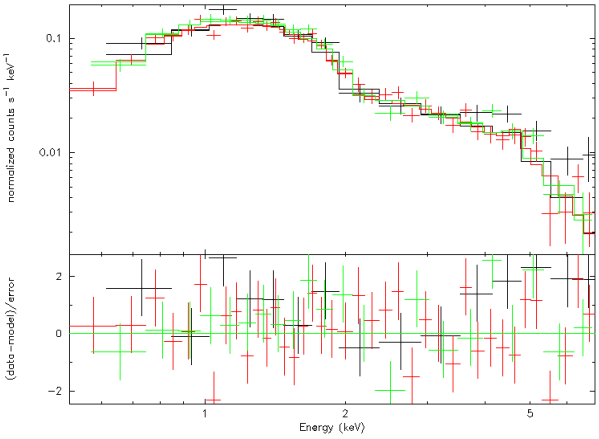

Figure 5.17: X-ray spectral fit of RXC J1115.2+5320. The spectral analysis is carried out on the three obsID simultaneously. The best-fit model and the data of each obsID dataset are highlighted in a different color. In the bottom panel are shown the residual.

We carried out the spectral analysis into a region of R_{500}, which extends over ~ 1.36 Mpc (3.84 arcmin) at the cluster redshift. The best-fit parameters of the model which characterize the ICM emission are reported in Table 5.6. A measure of the ICM temperature of the cluster have been previously inferred by Cavagnolo et al. 2009, who found an averaged temperature of ~ 8.03 keV from the same X-ray data analyzed in this work. We also infer a metallicity of the cluster gas, which turned out to be ~ 0.24.

Table 5.6: Best-fit spectral analysis parameters measured in the RXC J1115.2+5320 cluster.

	PHABS*APEC (1)	PHABS*APEC (2)
$N_{\rm HI}$ (10^{-20} cm^{-2})	0.888	0.888
kT (keV)	$9.48^{+0.83}_{-0.83}$	$9.55^{+0.85}_{-0.84}$
Abundance	0.3	$0.24^{+0.10}_{-0.10}$
Redshift	0.4699	0.4699
norm (10^{-3})	$3.13^{+0.05}_{-0.04}$	$3.16^{+0.07}_{-0.07}$
L (10^{44} ergs^{-1})	$8.04^{+0.23}_{-0.08}$	$8.050^{+0.101}_{-0.099}$
χ^2/ d.o.f	0.98	0.98

Notes. The luminosity is referred to the 0.1-2.4 keV energy range. The (2) best-fit is obtained with a free metallicity parameter. All the measures has a confidence level of the 68%.

We choose to extract the surface brightness profile within an elliptical region which seems to follow the gas distribution better than a circular region (Figure 5.18a). The best-fit parameters of the β-model are $\beta = 0.52^{+0.02}_{-0.01}$, the core radius $r_c = 0.51^{+0.054}_{-0.05}$ arcmin and a normalization of $0.076^{+0.006}_{-0.005}$ cts s^{-1}arcmin^2 (68% confidence level). This model has a χ^2/ d.o.f of 1.21.

5.4 Abell 1622

No radio and X-ray studies of this cluster have been published so far. The SDSS optical field is shown in Figure 5.19. The cluster is located at a redshift of 0.283.

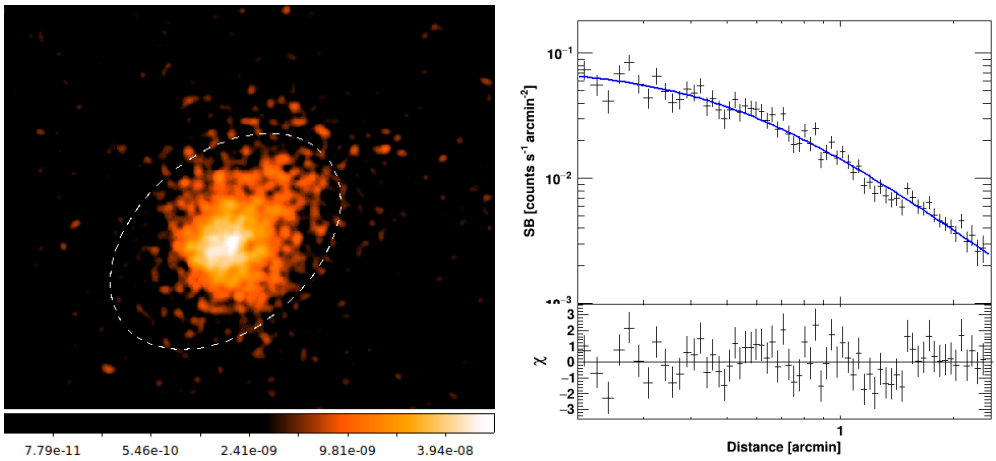

(a) (b)

Figure 5.18: *Left*: The elliptical region, drawn on the smoothed X-ray image, from which is extracted the surface brightness profile of RXC J1115.2+5320. The major axes is set at 800 kpc and the minor one is set at 600 kpc. *Right* The surface brightness profile fitted with a β-model (best-fit in blue line). The bottom panel shows the residuals.

5.4.1 Radio analysis

The dataset of Abell 1622 includes 2 pointings. We produced three images from the LOFAR data with the parameters in Table 5.7 adopting the procedures in Section 4.1. In the images no diffuse emission is detected at the cluster center. However, several discrete bright sources are observed in the cluster environment. The most remarkable feature in the radio images is a luminous HT radio galaxy in the cluster outskirts. We decided to examine in more detail the ICM dynamical interaction on such object, taking advantage from the high resolution LOFAR image (Figure 5.20). Since the large scale emission is absent, the imaging was carried out without performing the discrete sources subtraction to the dataset. The images obtained are shown in Figure 5.20, Figure 5.21a and Figure 5.21b.

Table 5.7: Imaging parameters for the Abell 1622 cluster.

Figure	Beam size ($'' \times ''$)	Im. size (pixel $\times$pixel)	Pixel size ($''$)	Robust	Taper ($''$)	rms (μJy $\cdot$ beam^{-1})
Figure 5.21a	22×19	540×540	4.0	-0.5	15	150
Figure 5.21b	17×13	618×618	3.5	-0.5	10	120
Figure 5.20	8×5	1800×1800	1.2	-0.5	n.a.	74

Notes. N.a. is "not applied".

5.4.2 X-ray analysis

Abell 1622 was observed twice (obsID 11763 and 17154) with Chandra ACIS-I for a total exposure time of 26.78 ks. Following the procedure outlined in Section 4.3 we obtained the X-ray image in the 0.5-2.0 keV band (Figure 5.22).

The field in which Abell 1622 is detected appears as a lively environment in the X-ray band. Different X-ray clumps of emission are detected (labelled as A1622-1, A1622-2, and A1622-3 from the larger one to the smaller one, respectively, Figure 5.23). The predominant system, A1622-1, can be distinguished among these as the most massive clump which represents the principal

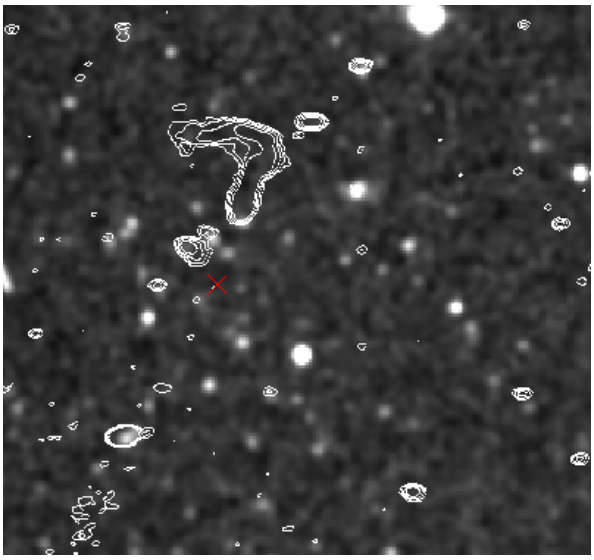

Figure 5.19: Radio contours from the LOFAR image of Abell 1622 overlaid on the SDSS optical observation. The red cross indicates approximately the center of cluster (RA=12°49′41.067″; DEC=49°52′24.250′).

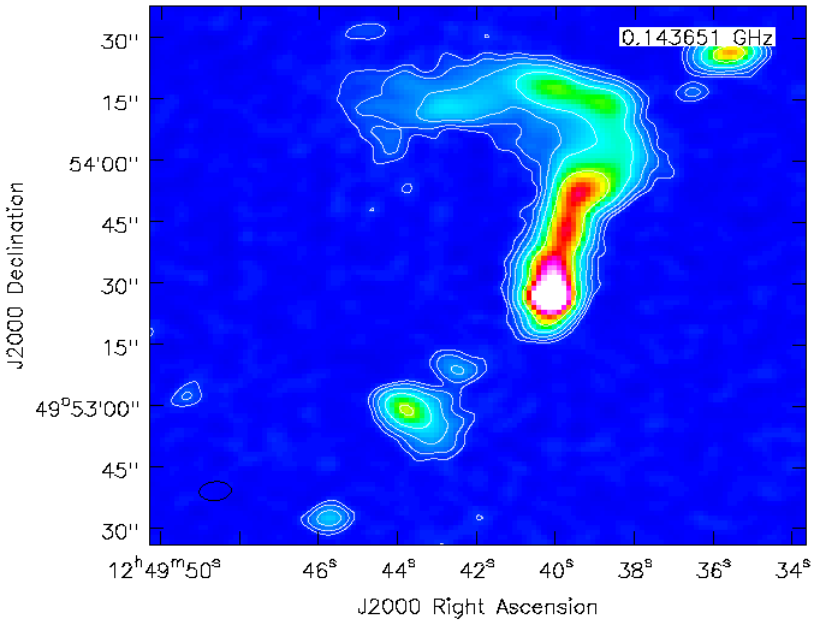

Figure 5.20: The bent radio source observed in Abell 1622 cluster, shown in the high resolution ($8'' \times 5''$) LOFAR image. Radio contours are spaced of a factor 2 starting from $3\sigma_{rms}$, where σ_{rms} is 74 $\mu\text{Jy} \cdot \text{beam}^{-1}$.

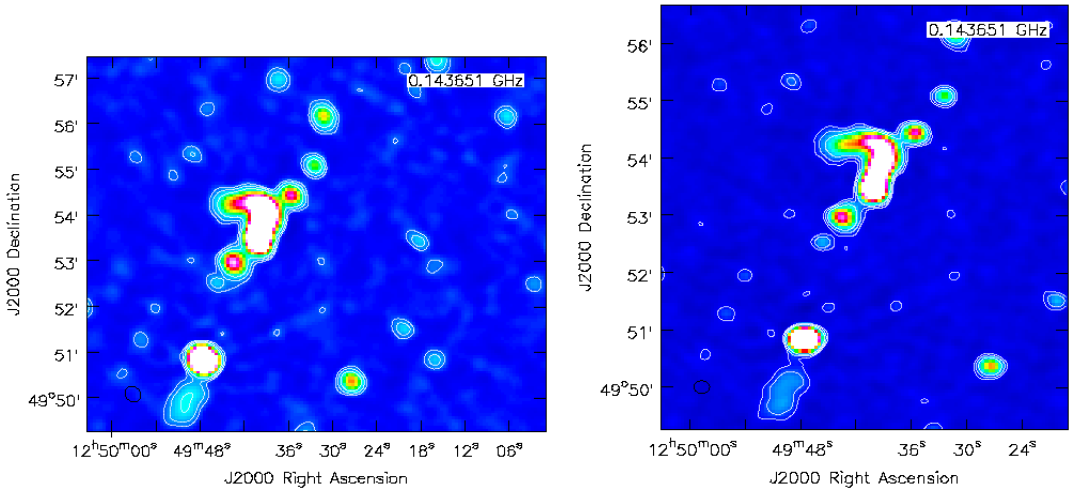

(a) (b)

Figure 5.21: The low (*left*) and the medium (*rigth*) resolution images of Abell 1622 from the LOFAR data. The contour levels are separated by a factor 2 starting from $3\sigma_{rms}$. The images parameter are indicated in Table 5.7.

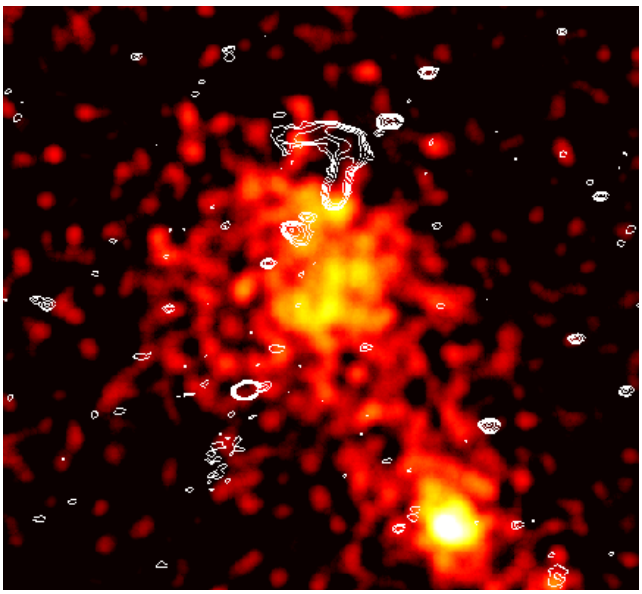

Figure 5.22: LOFAR contours of Abell 1622 overplotted on the smoothed Chandra image in the 0.2-5.0 keV band. Radio contours of the $8'' \times 5''$ image are spaced of a factor 2 from $3\sigma_{rms}$, where σ_{rms} is 74 $\mu\text{Jy} \cdot \text{beam}^{-1}$.

contribution to the cluster emission and mass. In the next Chapter we will refer to A1622-1 as Abell 1622. We focused the X-ray analysis on this; however we inferred the temperature of the gas also for A1622-2 and A1622-3 clumps.

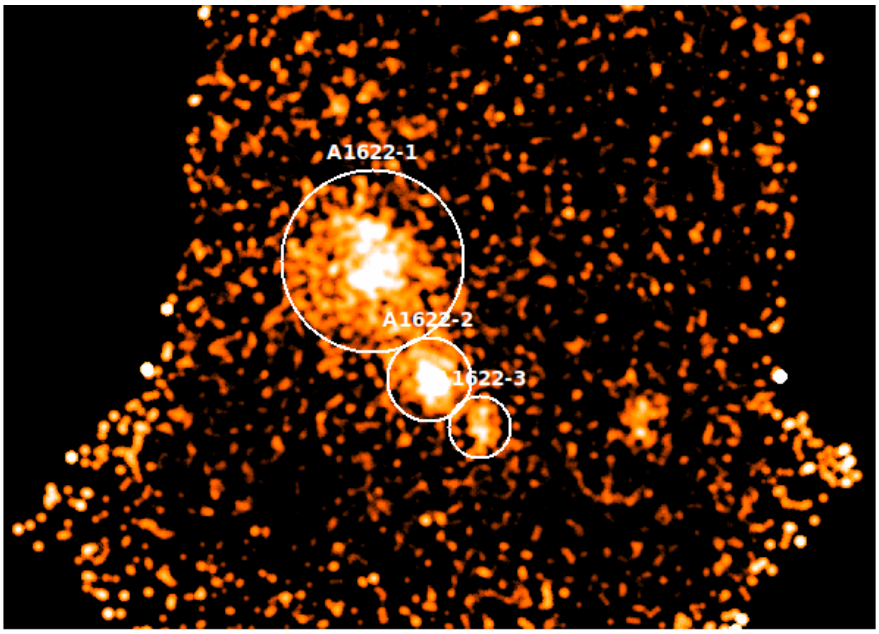

Figure 5.23: Chandra X-ray image of Abell 1622. The image is realized in the 0.5-2.0 keV band and convoluted with a Gaussian of $\sigma = 10''$. The white regions highlighting the clump of the field are set for the energy spectrum extraction. These main X-ray clumps are labelled.

The spectra have been extracted within a region of about 650 kpc (corresponding to 2.53 arcmin) for the A1622-1, and inside $\sim$ 300 kpc (1.17 armin) and $\sim$ 260 kpc (1 arcmin) for A1622-2 and A1622-3, respectively (Figure 5.23). A model of absorbed thermal ICM (see Section 4.3) applied on A1622-2 and A1622-3 provides temperatures of the gas of $\sim$ 2.83 keV and $\sim$ 2.16 keV respectively. The best-fit parameters of A1622-1 spectral fitting are reported in Table 5.8. For this cluster we found a metallicity value of $\sim$ 0.32 which is a value typically observed in the ICM of clusters.

Table 5.8: Best-fit parameters for the A1622-1 spectral analysis.

	`PHABS*APEC` (1)	`PHABS*APEC` (2)
$N_{\rm HI}$ (10^{-20} cm^{-2})	1.15	1.15
kT (keV)	$5.20^{+0.63}_{-0.53}$	$5.17^{+0.63}_{-0.53}$
Abundance	0.30	$0.32^{+0.19}_{-0.17}$
Redshift	0.283	0.283
norm (10^{-3})	$1.06^{+0.04}_{-0.04}$	$1.05^{+0.06}_{-0.06}$
L (10^{44} ergs^{-1})	$1.23^{+0.07}_{-0.07}$	$1.16^{+0.11}_{-0.10}$
χ^2/ d.o.f	1.04	1.05

Notes. The luminosity value are taken in the 0.1-2.4 keV band. The (2) column is referred to the case in which the metallicity parameter is not set by us but inferred from the fitting. The measures are reported with a confidence level of 68 %.

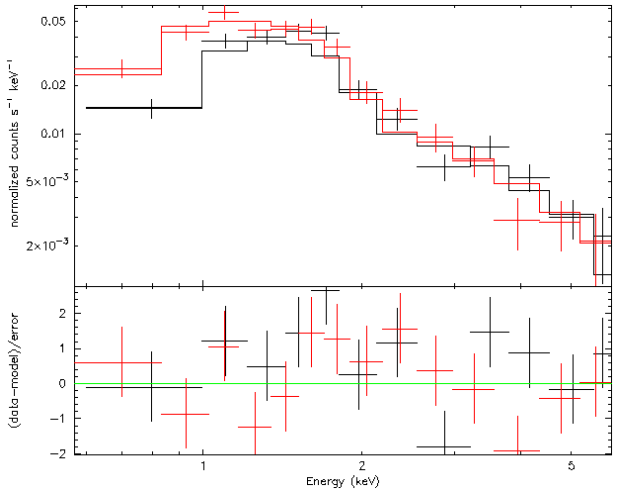

Figure 5.24: Spectral best-fit model obtained for Abell 1622 (main cluster). Two different colors are referred to the two obsID data. The bottom panel reports the residuals.

In order to be consistent with the previous studies on the $L_X - P_{1.4}$ correlation, the X-ray luminosity of A1622-1 within a radius of R_{500} is measured. Contrary to the case of Abell 1550, the FoV of the Chandra observation of Abell 1622 recover an area which includes the R_{500} of A1622-1, that is $\sim$ 1.02 Mpc (correspondent to $3.9'$ at the redshift of the cluster). Then we extracted the spectrum from a region of such radius and inferred the X-ray luminosity, which resulted of $1.78^{+0.20}_{-0.15} \times 10^{44}\,\mathrm{ergs}^{-1}$. Since in this region is also included part of the emission of A1622-2, we subtracted its contribution from the A1622-1 X-ray luminosity. To this we measured an X-ray luminosity of $3.67^{+0.23}_{-0.13} \times 10^{43}\,\mathrm{ergs}^{-1}$ in A1622-2. Then the X-ray luminosity of A1622-1 results $1.41^{+0.22}_{+0.16} \times 10^{44}\,\mathrm{ergs}^{-1}$.

We extracted the A1622-1 surface brightness profile within a circular region of 500 kpc. This region includes the entire cluster emission reaching the peripheral HT. So this radius size represents a suitable choice for the analysis of the interplay between the HT and the external gas (discussed in Section 6.3). The β-value from the best-fit is $0.76^{+0.52}_{-0.19}$, the core radius r_c is $1.44^{+0.80}_{-0.40}$ arcmin and the central surface brightness is $8.78^{+0.88}_{-0.78} \times 10^{-3}$ cts s^{-1}arcmin^2 (all of them has a confidence level of 68 %). The model has a $\chi^2/$ d.o.f of 0.98.

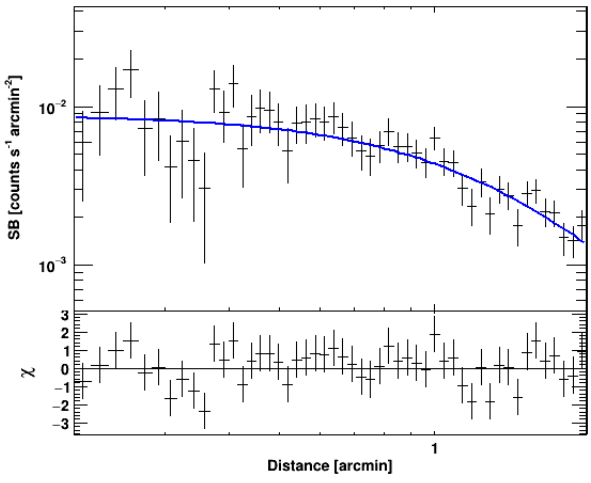

Figure 5.25: The β-model best-fit of the Abell 1622 surface brightness profile. The blue line shows the best-fit model. Bottom are shown the residuals.

In the analysis of this target, we used the deprojected density and the β-model fit of the data to extract the electron density profile. From this we obtained the pressure profile assuming an isothermal ICM. All the procedures are outlined in the Section 4.3. This profile will be used in the comparison between the thermal and the non-thermal pressure comparison in the HT.

Chapter 6

Connection between thermal and non-thermal plasma in galaxy clusters

As discussed in Section 2.2.1 non-thermal particles and magnetic fields in galaxy clusters show a connection with the thermal ICM. The morphology of RHs broadly follows that of the underlying thermal ICM and several scaling relations exist between the non-thermal emission of RH and several thermal properties of the hosting GC including mass, temperature and X-ray luminosity. The thermal - non-thermal connection provides important information on the origin of the non-thermal components in GCs. In this Chapter we explore the connection between thermal and non-thermal emission in our clusters and compare them with other RHs in the literature.

6.1 Point to Point analysis

The RHs emission is generally found to spatially follow the spatial distribution of the thermal ICM emission, suggesting a connection between these two components. In order to quantify this correlation Govoni et al. 2001 and Feretti et al. 2001 performed the combined analysis of the radio and X-ray surface brightness on of clusters with RHs. These studies and their follow-up found that RHs have in general a sub-linear scaling between radio and X-ray brightness, in the form $I_R \propto I_X^b$ with $b \leq 1$. This behavior has been interpreted against a secondary origin of RHs (Section 2.2.1).

Following their idea we carried out a "point-to-point" analysis on the two targets showing RH emission, Abell 1550 and RXC J1115.2+5320. In Table 6.1 are reported the properties of these clusters.

Table 6.1: Observations properties of the RH hosting clusters.

	Radio			X-ray
Cluster name	Frequency (MHz)	Beam size ($'' \times ''$)	σ_{rms} (μJy $\cdot$ beam^{-1})	Tot. exposure time (ks)
Abell 1550	144	20×18	121	7
RXC J1115.2+5320	144	15×10	104	35

Basically the idea consists in measuring the radio surface brightness, I_R, and the X-ray surface brightness, I_X, in each point of the region covered by the RH emission. The surface brightness measurements were done on the Chandra X-ray images in the 0.5 - 2.0 keV band and on the LOFAR radio images at 144 MHz. The images used in the procedure should be

source-subtracted in order to avoid contamination from discrete sources. Alternatively discrete sources should be masked. For the analysis is adopted a Python script designed by relying on the CASA software (Ignesti et al. in prep.; Ignesti et al. 2018).

Procedure A grid is generated on the images selecting regions where the radio flux density results higher of a certain threshold (2-3σ that is the region including the halo). The grid is designed to avoid emission from the central bright source (examples of grids are shown in Figure 6.1a and Figure 6.2a). The cell size of the mesh has to be larger than the beam size of the radio image. The Chandra images have resolution of $\sim 0.5''$ then the limit is set always on the basis of the radio images which have lower resolution.

The radio and X-ray surface brightness are calculated in each cell with the relative errors. The I_X is measured by subtracting the background emission and correcting for the exposure map and the error is computed assuming that the counts are Poisson-distributed. In the radio images the error is assumed as equal to Eq. (4.1). The measurements allow to search for radio - X-ray correlations in the form $I_R \propto I_X^k$. In the code used in this Thesis the correlation is computed with the BCES (Bivariate Correlated Errors and intrinsic Scatter) method (Akritas & Bershady 1996).

The presence of correlation is also checked with a Spearman test. This is a statistical test which analyzes a rank correlation coefficient, ρ_s, of data arrays. The ρ_s value can span from 0, when there is any correlation to 1, in the case of a perfect correlation.

To avoid statistical biases due to the particular structure and position of the grids, we also carried out Monte Carlo simulations. This procedure generates a set of random grids (avoiding discrete sources) that are used to re-evaluate the index of the correlation and the Spearman coefficient in an iterative way. The k_{MC} and its dispersion $\sigma_{k_{MC}}$ are evaluated at each cycle and a value of k_{MC} is extracted from a Gaussian distribution using a bootsraping procedure. Finally the index of the relation is given by $k = \bar{k}_{MC} \pm \sigma_{k_{MC}}$ where $\bar{k}_{MC}$ and $\sigma_{k_{MC}}$ are the mean and the standard deviation of the distribution of bootstrapped k obtained at the end of each cycle.

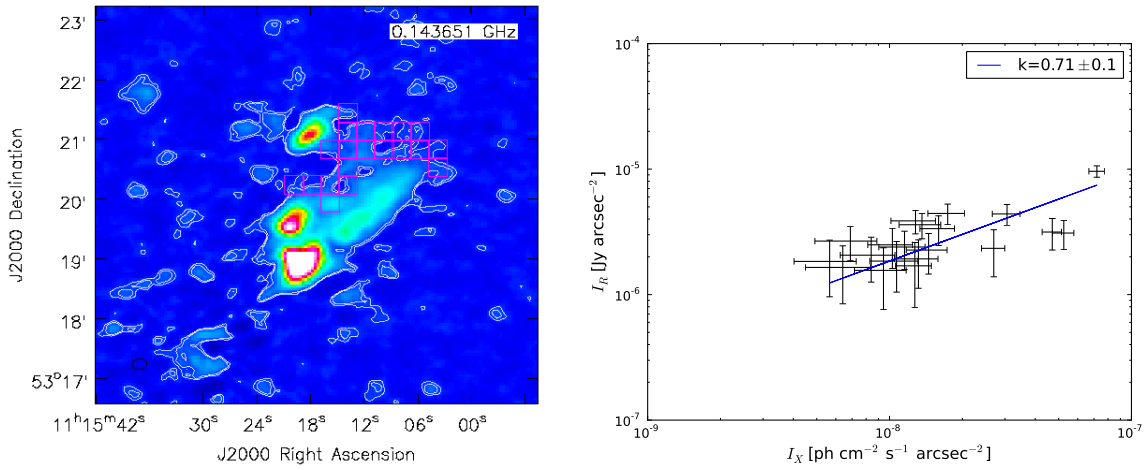

(a) (b)

Figure 6.1: *Left:* The 144 MHz image of RXC J1115.2+5320 with superimposed the mesh adopted for a single point-to-point analysis. The contour levels of the image are drawn at 2 and 3 times σ_{rms}. The cell size of the mesh is $18'' \times 18''$ and it is obtained with a threshold of $2\sigma_{rms}$. *Right:* The correlation found with the sampling of the halo emission shown on the left. Each point of the correlation corresponds to a cell of the grid. The blue line represent the best-fit power-law. The analysis gives a $k = 0.71 \pm 0.1$ and a $\rho_s = 0.69$.

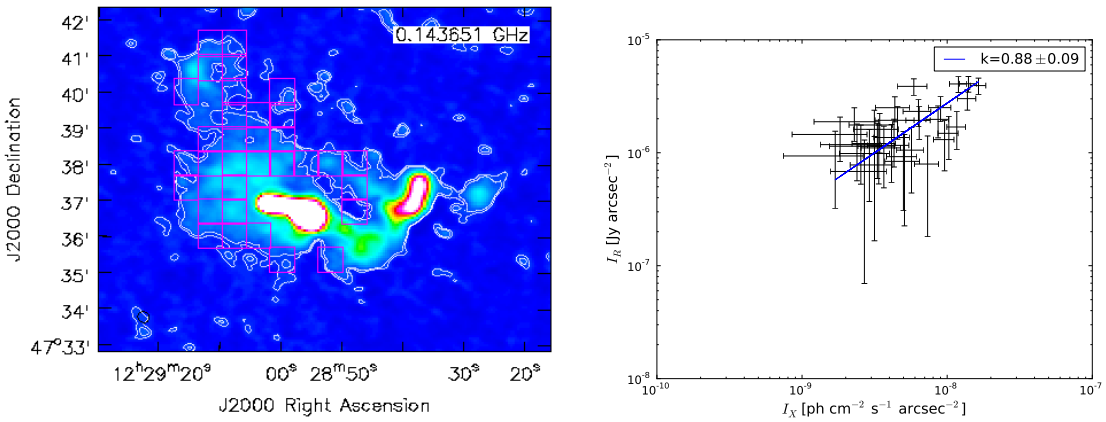

(a) (b)

Figure 6.2: *Left:* The LOFAR image of the Abell 1550 cluster sampled with the mesh built giving a threshold of $2\sigma_{rms}$ and a cell size of $40'' \times 40''$. The contour levels are referred to 2 and 3 σ_{rms}. *Right:* The best-fit power-law obtained with the mesh on the left. It is found a correlation index of $k = 0.88 \pm 0.09$. The best-fit has a Spearman coefficient of 0.56.

Analysis on the targets and results We performed simulations with 100 iterations of the single point-to-point analysis in Abell 1550 and RXC J1115.2+5320.

Two example of single analysis for each cluster are shown in Figure 6.1 and Figure 6.2. The histograms which summarize the results of the Monte Carlo simulations are shown in Figure 6.3 and Figure 6.4. The values of k and the Spearman coefficients, ρ_s, are reported in Table 6.2, together with the parameters employed in the analysis.

We found clear trends between the radio and X-ray brightness in both clusters. Specifically the radio brightness scales linearly with the X-ray brightness in Abell 1550, whereas a sub-linear trend is observed in the case of RXC J1115.2+5320.

The trends show a significant dispersion that is likely contributed by intrinsic dispersion. This is clear also from the analysis of the Spearman tests that find evidence for correlations that are not particularly strong ($\rho_s \sim 0.5$) although higher values $\rho_s \sim 0.7$ are obtained in single trials of the Monte Carlo.

We tested different cell size in the sampling of the images, in order to find a good compromise between the signal-to-noise ratio in each cell and the number of the cells. Larger cell size gives higher constrained value of surface brightness but lower points available for the fitting. Specifically, we used squared cell of sides of 15, 18 and 21 arcseconds for RXC J1115.2+5320 (the radio image has a beam size of $15'' \times 10''$), and 28 and 40 arcseconds for Abell 1550 (the radio image has a beam size of $20'' \times 18''$). Even the threshold used to create the mesh is varied from 2 to 3 times the σ_{rms} for each Monte Carlo analysis with different cell size. The resulting values for k are always consistent with the ones in Table 6.2.

Table 6.2: Best-fit parameters of the Monte Carlo analysis.

Cluster name	k	ρ_s	Mesh cell size ($''$)	Mesh threshold (σ_{rms})
Abell 1550	0.97 ± 0.08	0.43 ± 0.08	40	2
RXC J1115.2+5320	0.52 ± 0.13	0.45 ± 0.16	18	2

Radio to X-ray brightness in giant RH are generally linear or sub-linear (Figure 6.5).
In general, a connection between thermal and non-thermal radio emission is expected in the

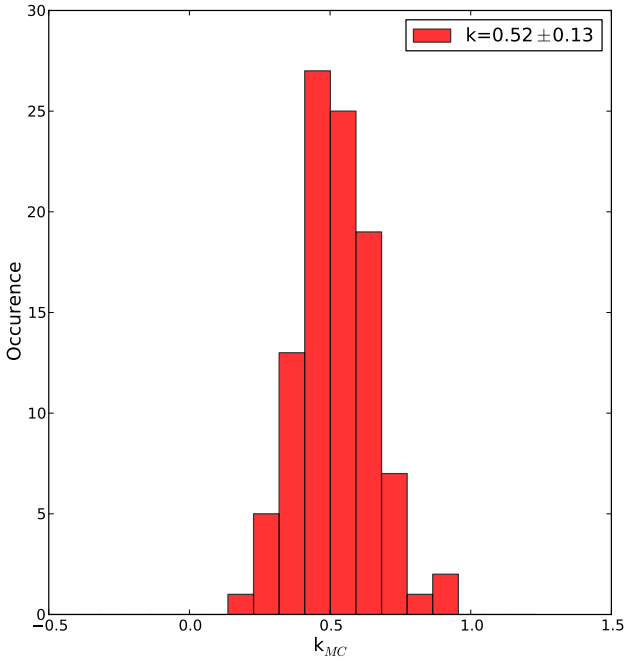

Figure 6.3: The histogram showing the distribution of the k_{MC} for RXC J1115.2+5320 found with the Monte Carlo simulation. The k of the correlation $I_R \propto I_X^k$ is shown in the legend, other details of the simulation are reported in Table 6.2.

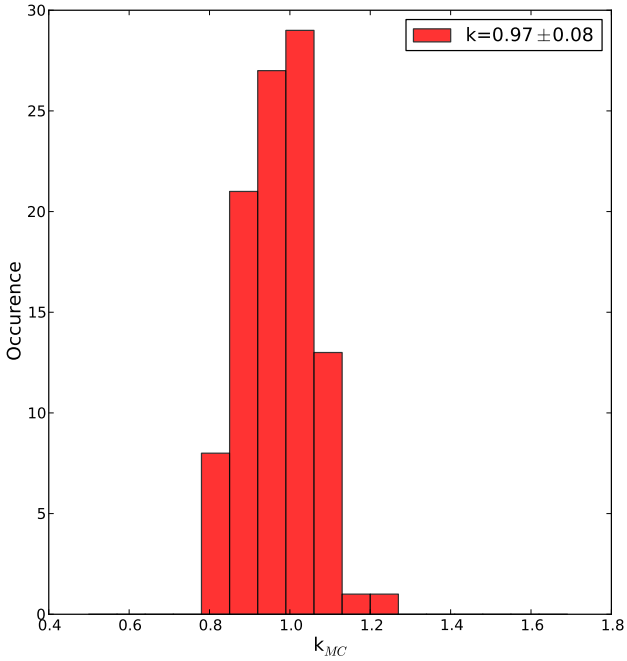

Figure 6.4: The k_{MC} occurrence in a Monte Carlo simulation of the Abell 1550 point-to-point analysis. The k of the $I_R \propto I_X^k$ correlation is shown in the legend, other details of the simulation are reported in Table 6.2.

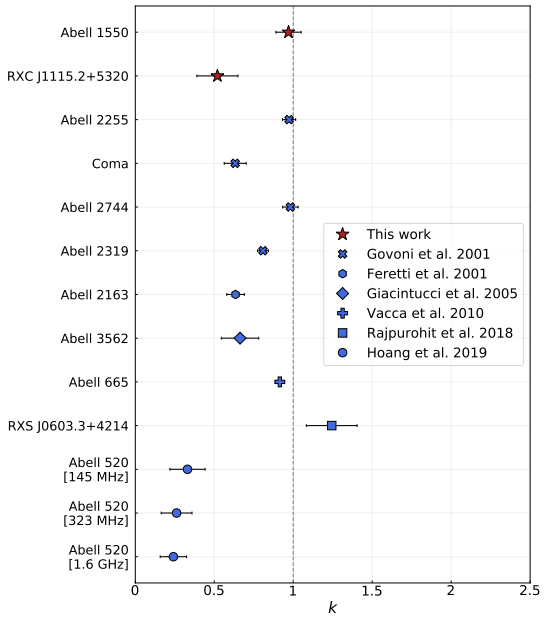

Figure 6.5: Observed scalings k of the RHs analyzed in this work (red) compared with the values observed in previous works (blue).

scenario in which the dark matter driven kinetic energy in mergers is dissipated on both the thermal ICM (heating) and non-thermal electrons (acceleration). For this reason the connection of radio and X-ray brightness provides important information on theoretical models.

In particular the surface brightness I_X and I_R correspond to the emissivity in that band of line-of-sight. The thermal emissivity is described by $j_X \propto n_e^2 (kT_e)^{1/2}$, where n_e and T_e are density and temperature, respectively, of the electrons in ICM. Assuming an isothermal gas, the emissivity is proportional to the energy density squared, given by $\varepsilon_{th} = 3 n_e k T_e$, so it becomes $j_X \propto \varepsilon_{th}^2 (kT_e)^{-3/2}$.

Assuming that the relativistic particles energy is distributed according to $N(\varepsilon)\,\mathrm{d}\varepsilon = N_0 \varepsilon^{-\delta}\,\mathrm{d}\varepsilon$, the radio emissivity results: $j_R \propto N_0 B^{(\delta+1)/2} \nu^{-(\delta-1)/2}$, where ν is the emission frequency and B the magnetic field in the ICM.

Assuming for simplicity a spectral index $\alpha \sim 1$ (i.e. $\delta \sim 3$), $j_R \propto \varepsilon_{CRe} \varepsilon_B \nu^{-1}$, where $\varepsilon_{CRe} = \int \varepsilon N(\varepsilon)\,\mathrm{d}\varepsilon$ is the energy density of relativistic electrons and $\varepsilon_B = B^2/8\pi$ is the magnetic field energy density. In the case where the temperature of the plasma in the region where correlations are extracted to be the same, a scaling $\varepsilon_{CRe}\varepsilon_B \propto \varepsilon_{th}$ implies a linear scaling between the synchrotron and X-ray brightness, whereas a sub-linear scaling between brightness implies that the spatial distribution of electrons and/or the magnetic field is broader than that of the thermal plasma.

In the case of hadronic models (see Section 2.2.1) is valid $\epsilon_{CRe} \propto \epsilon_{CRp} \epsilon_{th}$, where ϵ_{CRp} is the energy density of primary relativistic protons in the ICM. It implies that linear correlations between radio and X-ray brightness in these models can be explained under the assumption that the energy density of magnetic field B and CR in the cluster does not decline with radius; sub-linear correlations require that the energy density of CR increases with radius. Both these assumptions are not physical and for this reason finding linear or sub-linear scalings between radio and X-ray brightness challenges these models (Brunetti & Jones 2014).

6.2 Cluster dynamical state-RH connection

6.2.1 Morphological parameters

Over the past years, several studies confirm the tight connection between clusters dynamical activity and the occurrence of RHs within them (D. Buote 2001; Venturi et al. 2008; Govoni et al. 2005).

Cassano et al. 2010b carried out the first statistical analysis of the correlation between cluster dynamics and RH. They studied 32 clusters with and without RHs, demonstrating that systems in a disturbed dynamical state generally host a RH while the RH is absent in relaxed clusters.

Follow-up studies in this direction basically confirmed these findings with different samples and approaches (e.g. Kale 2013; Cuciti et al. 2015; Birzan et al. 2019), with only few cases of systems with more relaxed morphology hosting a RH (e.g., Bonafede et al. 2014b). The statistical connection between dynamics (mergers) and RH supports the re-acceleration scenario where mergers inject the energy that power relativistic plasma, for example via turbulent acceleration (Brunetti et al. 2009).

The dynamical activity imprinting in the cluster gas can be detected in the X-ray surface brightness analysis. This has been investigated also through numerical simulations where the impact of mergers on the X-ray morphology of clusters can be studies (Poole et al. 2006).

A method widely adopted to recognize the merger activity consists in the measure of morphological parameters. This approach was utilized by Cassano et al. 2010b in their study. They measured the degree of disturbance of a sample of clusters through three parameters: the power ratios (e.g. D. A. Buote & Tsai 1995; Tesla E. Jeltema et al. 2005), the centroid shift of X-ray emitting gas (e.g. Mohr et al. 1993; Poole et al. 2006), and the surface brightness concentration (e.g. Santos et al. 2008). As mentioned in Section 2.2.1, higher values of the concentration parameter (c) and lower of the centroid shift (w) are found in relaxed clusters and the opposite is seen for unrelaxed clusters. The main result of Cassano et al. 2010b was that RHs are observed exclusively in merging clusters (with low c and high w) as shown in Figure 2.8. We studied the morphological parameters of our 3 targets and compared them with the observed radio properties and with the statistical behaviors observed in other clusters samples. The morphological analysis was carried out on the X-ray images in 0.5-2.0 keV band. The parameters are defined as follows.

- **The centroid shift**, **w**, is defined as the standard deviation of the projected separation, Δ, between the surface brightness peak and the centroid taken from circular aperture of radius R_{ap}. It is indicated in unit of R_{ap} (Poole et al. 2006; Maughan et al. 2008):

$$w = \left[\frac{1}{N-1}\Sigma(\Delta_i - \langle\Delta\rangle)^2\right]^{1/2} \times \frac{1}{R_{ap}}.$$

  The centroid is comupted starting from $R_{ap} = 500\,\mathrm{kpc}$ decreasing each time of 5% until $0.05R_{ap}$ (following Cassano et al. 2010b). The Δ_i is referred to the distance between the peak and the centroid in the the i-*th* aperture. Since it is measured a projected surface brightness, the centroid shift method is poorly sensitive to the presence of substructures (and thus mergers) along the line of sight.

- **The concentration parameter**, **c**, is defined as the ratio between the central region ($r < 100\,\mathrm{kpc}$) surface brightness and the larger region surface brightness ($r < 500\,\mathrm{kpc}$) (Santos et al. 2008):

$$c = \frac{S(r < 100\,\mathrm{kpc})}{S(r < 500\,\mathrm{kpc})}.$$

This parameter provides an indication of recent merger activity which spreads the gas concentrated in the compact core over larger area.

Following Cassano et al. 2010b, we deduced the cluster dynamical state by computing the w an c parameters and by finding their position in the $c - w$ diagram. In Cassano et al. 2010b the representation of the segregation between cool-core and merging systems is defined by the following values: $w = 0.012$ and $c = 0.2$. Merging clusters have $w > 0.012$ and $c < 0.2$ and relaxed clusters (without RHs) show $w < 0.012$ and $c > 0.2$. We used these as reference.

Results The parameters obtained for the targets are reported in Table 6.3. The three clusters sit in the "disturbed region" of the $c - w$ diagram, shown in Figure 6.6. The presence of a RH in Abell 1550 and RXC J1115.2+5320 is thus not surprising. On the other hand Abell 1622 is an example of dynamically disturbed system without RHs and deserve further consideration in next Section.

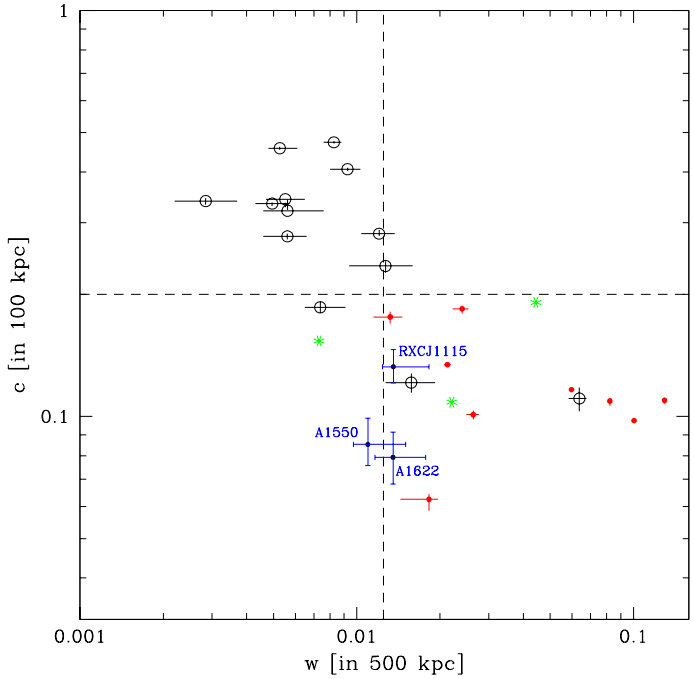

Figure 6.6: The distribution in the $c - w$ plane of a sample of clusters from the Cassano et al. 2013 work. They are included Abell 1550, RXC J1115.2+5320 and Abell 1622 clusters (in blue). Clusters hosting giant RH and USSRH are marked with red points and green asterisks, respectively while clusters without RH are shown with black open dots. The vertical and horizontal dashed lines are referred to $c = 0.2$ and $w = 0.012$, following Cassano et al. 2010b.

6.2.2 RH scaling relations

The scaling relations between the radio power of RHs in clusters and the gas properties, are important to constrain the origin and evolution of these sources. Cassano et al. 2007 proposed a simple scenario in which, in a quasi-stationary condition, the turbulence energy is dissipated accelerating particles that in turn reradiate the energy via synchrotron and IC mechanisms. The turbulence generated during a merger in the RH volume is injected with a rate estimated as: $\dot{\varepsilon}_{turb} \propto \rho_H \cdot v_i^2/\tau_{cross}$, where ρ_H is the ICM mean density within the RH, v_i is the impact velocity

Table 6.3: Morphological parameters of the clusters.

Cluster	c-parameter	w-parameter
Abell 1550	$0.085^{+0.011}_{-0.012}$	$0.011^{+0.003}_{-0.003}$
RXC J1115.2+5320	$0.133^{+0.013}_{-0.012}$	$0.014^{+0.003}_{-0.004}$
Abell 1622	$0.079^{+0.011}_{-0.058}$	$0.014^{+0.003}_{-0.003}$

Notes. The measures are reported within the 68% confidence level.

between the systems, and τ_{cross} is the cluster crossing time. Under the assumption that the ratio between the energy densities in thermal and non-thermal components is independent from cluster (hosting RH) mass, the synchrotron radio power of the emitting particles results $\nu P_\nu \propto (M\sigma^3)/F(z, M, B_H)$, where M is the cluster total mass, σ is its velocity dispersion and B_H^2 is the average magnetic field strength within the RH size while $F(z, M, B_H) = [1 + (3.2(1+z)^2/B_H)^2]$ is a function constant for $B_H^2 \gg B_{cmb}^2$. These conditions lead to the relation between the radio power and the cluster mass. According to the relations $M \propto R_H^{2.17}$, where R_H is the RH size and $R_H \propto R_{500}^{3.1}$ (derived by Cassano et al. 2007 and Basu 2012 respectively) the relation can be expressed in terms of M_{500}:

$$\nu P_\nu \propto M_{500}^4. \tag{6.1}$$

The re-acceleration is expected to produce a significant dispersion around the scaling relation due to a variety of spectral shapes of RH and the different type of mergers (major or a sequence of smaller mergers) that inject the energy in the ICM. Current observations find a relation between the mass of the hosting clusters and radio luminosity of the RH in the form:

$$\log\left(\frac{P_{1.4}}{10^{24.5}\,\mathrm{WHz^{-1}}}\right) = B\log\left(\frac{M_{500}}{10^{14.9}M_\odot}\right) + A. \tag{6.2}$$

The best-fit slope is $B = 3.77 \pm 0.57$ adopting a BCES-bisector method and $B = 4.51 \pm 0.78$ with the BCES- orthogonal method (Cassano et al. 2013). Similar to the correlation with mass also a correlation with the X-ray luminosity is found (Cassano et al. 2013) in the form:

$$\log\left(\frac{P_{1.4}}{10^{24.5}\,\mathrm{WHz^{-1}}}\right) = B\log\left(\frac{L_X}{10^{45}\,\mathrm{ergs^{-1}}}\right) + A. \tag{6.3}$$

The best-fit slope is $B = 2.1 \pm 0.2$ adopting a BCES-bisector method and $B = 2.2 \pm 0.2$ with the BCES- orthogonal method. In the context of the re-acceleration scenario a radio bi-modality is also expected. Mergers generate RHs that follow the correlation (6.2 or 6.3) and more relaxed systems are underluminous in radio. Clusters evolve between the two populations as a result of the hierarchical grow of these systems and from the separation between the two classes of clusters it is possible to infer crucial information on the time scale of RHs, on the physics of particle acceleration, and more in general on the way energy is transported from large scales to the micro-scales in the ICM. The relation are widely confirmed by the observations (as described in Chapter 2) and they can be explained by admitting that the RHs are transient phenomenons linked to the merging events. Massive clusters undergoing merger events populate the $P_{1.4} - L_X$ correlation during the turbulence dissipation over the merger development. When the cluster reaches a relaxed state, it migrates in the upper limit region of the plane.

Results We obtained radio and X-ray luminosities of our clusters following the Chapther 5. These properties are reported in Table 6.4 with the masses of Abell 1550 and RXC J1115.2+5320 taken from the SZ-catalogue (Planck Collaboration et al. 2016). In the case of Abell 1622 we faced a problem for the measure of the mass. The mass obtained from Planck is contributed by the complex chain of subclusters that is observed in the X-rays (see Section 5.4). In order to separate this contribution from the mass of the main cluster (A1622-1) we used the $M_{500} - T$ relation of GCs found by Lovisari et al. 2015. More specifically we scaled the mass ratio of the different components with the temperature ratio obtained from our X-ray analysis and obtained a mass of $3.2^{+0.5}_{-0.7} \times 10^{14} M_{\odot}$ for Abell 1622 cluster.

The $P_{1.4}$ is inferred starting from the flux at 144 MHz and assuming $\alpha = 1.3$ for RXC J1115.2+5320 while the value of Abell 1550 is measured directly from the image at 1.4 GHz. In the case of Abell 1622, it is reported an upper limit to the radio luminosity (derived and discussed below). The X-ray luminosity are measured in the 0.1-2.4 keV energy range within R_{500}, coherently with the Cassano et al. 2013. In the case of Abell 1550 the luminosity is obtained assuming the β-model for the surface brightness profile.

Table 6.4: Thermal and non-thermal properties of the clusters.

Cluster	$P_{1.4}$ $(10^{23}\,\mathrm{WHz^{-1}})$	M_{500} $(10^{14} M_{\odot})$	L_{500} $(10^{44}\,\mathrm{ergs^{-1}})$
Abell 1550	8.54 ± 2.77	$5.88^{+0.38}_{-0.42}$	> 4.2
RXC J1115.2+5320	28.7 ± 2.3	$7.55^{+0.49}_{-0.52}$	$8.04^{+0.23}_{-0.08}$
Abell 1622	< 0.89	$3.2^{+0.5}_{-0.7}$	$1.41^{+0.22}_{+0.16}$

Notes. The $P_{1.4}$ reported for Abell 1622 represent the upper limit inferred by us.

The positions of our clusters in the Cassano et al. 2013 diagram are shown in Figure 6.7a and Figure 6.7a. Both RXC J1115.2+5320 and Abell 1550 are consistent with the scaling relations. The case of the upper limit in Abell 1622 is discussed in more details.

Upper limit for Abell 1622

We did not find a RH in the cluster Abell 1622. The question is wether this is due to the lack of sensitivity of our LOFAR observations (the cluster has a mass significantly smaller than the other two clusters) or because the radio emission from this system is intrinsically underluminous (no RH or fainter RH). We thus attempted to obtain a reliable upper limit to the RH emission in Abell 1622. We followed the approach adopted by Hoang et al. 2018.

We assumed that a putative RH in Abell 1622 extends like the RH in Abell 1550. Then following Hoang et al. 2018 we estimated a flux upper limit from $S = A \times \sigma_{rms}$, where A is the area of the diffuse emission and $\sigma_{rms} \sim 150\,\mu\mathrm{Jy \cdot beam^{-1}}$. The corresponding limit at 1.4 GHz (assuming $\alpha = 1.3$) is 8.9×10^{22} $\mathrm{WHz^{-1}}$. We also note that this limit is conservative. According to Cassano et al. 2007 and Murgia et al. 2009, the size of RHs scales with cluster mass with smaller halos being in less massive systems. If we had assumed a size of the halo in Abell 1622 taken from Cassano et al. 2007 scalings ($R_H \sim 310$ kpc) the limit would have been about 2 times deeper (i.e. about 5.3×10^{22} $\mathrm{WHz^{-1}}$). We concluded that the RH in A1622 is likely underluminous or absent.

This result is interesting for a number of reasons. First of all it should be stressed that the observation of RH in clusters with mass $< 3.5 - 4 \times 10^{14} M_{\odot}$ was challenging with previous instruments. Thus LOFAR is entering into a poorly explored territory. From a theoretical point

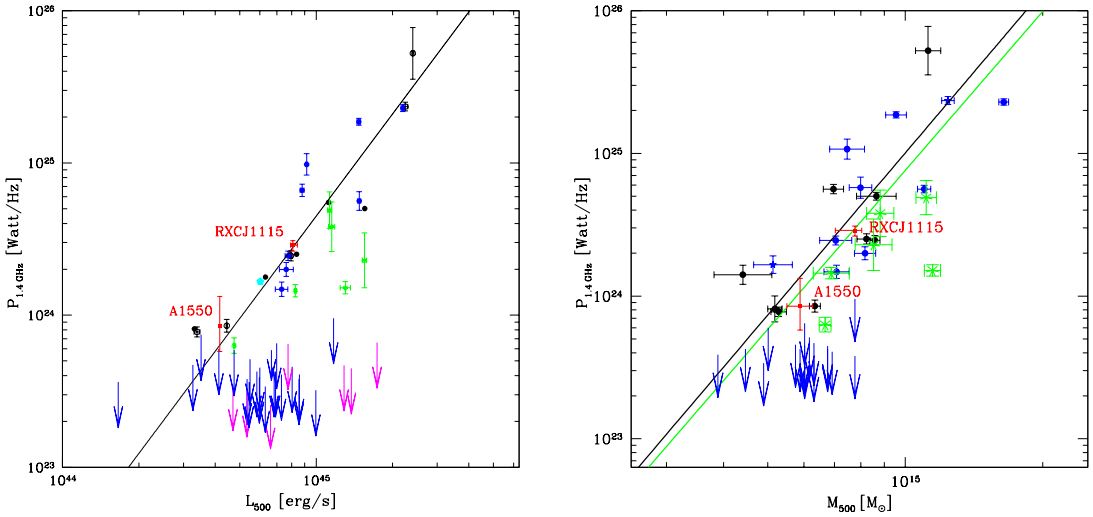

(a) (b)

Figure 6.7: The RH scaling relations reported in Cassano et al. 2013 in which are added the clusters analyzed in this Thesis work (red points). The Abell 1622 upper limit lies under the correlation. In both the diagram black and blue dots rapresent clusters from the Cassano et al. 2013 sample and from literature, respectively. With the green dots are marked USSRHs or candidate USSRHs. *Left*: The $P_{1.4} - L_X$ plane. The best fit for the giant RHs only is outlined with the black line. *Right*: The $P_{1.4} - M_{500}$ plane. The best-fit relations are referred to giant RHs only with the black line and the shadowed area (95% confidence region), and to all RHs (including USSRH) with the green line.

it is clear that the occurrence of RHs in clusters depends on cluster mass (and dynamics) because the mass actually sets the energy budget that becomes available to the acceleration of particles and amplification of magnetic fields in the ICM. In Figure 6.8 we show the expectation of RH occurrence from re-acceleration models (from Cassano et al. 2010a) as a function of virial mass (that is essentially $2\times M_{500}$ for our clusters). At virial masses $< 6\times10^{14} M_\odot$ ($M_{500} < 3\times10^{14} M_\odot$) the occurrence of RHs becomes very small also at low frequencies. As a consequence we might speculate that the absence of a RH in Abell 1622 is due to the smaller amount of energy that is available in these less massive systems.

6.3 The head-tail confinement

The interplay between the ICM and the non-thermal plasma in GC is a fundamental task with strong consequences on the feedback mechanisms in the ICM and on the physics of the non-thermal plasma, including radio galaxy. The asymmetric radio galaxies indeed are likely shaped by the ICM thermal action on non-thermal components of relativistic particles and magnetic field. A simple consideration is that radio plasma in radio galaxies and the ICM should be in pressure balance. From this balance it is possible to infer important information on the composition of radio lobes and on the energy of the ICM (e.g. Feretti et al. 1992). The available method to deduce the non-thermal pressure in a synchrotron emitting source is through the energy equipartition condition (described in details in 2). According to this, it is assumed that relativistic particles (protons and electrons) and magnetic field contribute with approximately the same amount of energy to the total budget of the source. The ICM pressure can be constrained from X-ray observations that measure density and temperature.

In this contest Abell 1622 represents an ideal case of study. An HT source is indeed detected

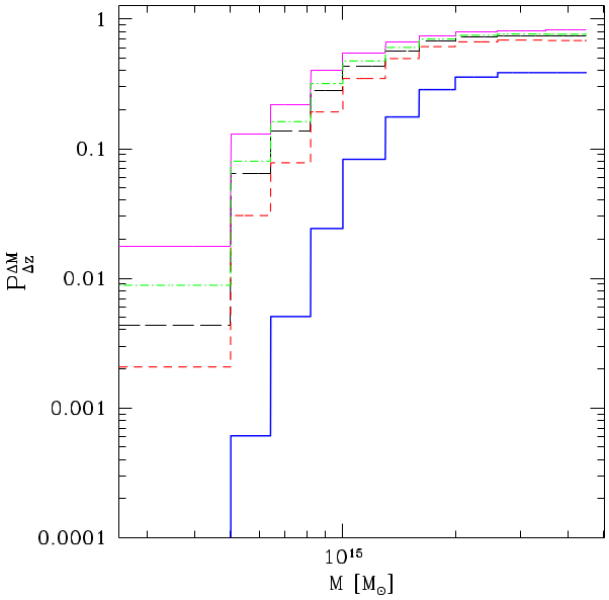

Figure 6.8: The fraction of RH hosting clusters as a function of the cluster virial mass. The RHs have a spectra steepening at frequency higher than the observation frequency. The simulation is carried out within a redshift range of 0 - 0.1. The different color lines are referred to the observation frequencies. These are 1.4 GHz, 240 MHz, 150 MHz, 120 MHz and 74 MHz, from bottom to top (from Cassano et al. 2010a).

in this cluster outskirts. The high resolution image in the radio band and the X-ray image allow to infer the non-thermal and thermal pressure profiles, respectively.

According to equipartition the internal pressure is (Feretti et al. 1992):

$$P_{eq} = (13/21)u_{min}.$$

where u_{min} is:

$$u_{min}\left[\frac{\text{erg}}{\text{cm}^3}\right] = \xi(\alpha,\nu_1,\nu_2)(1+k)^{4/7}(1+z)^{(12+4\alpha)/7}(\nu_{0[\text{MHz}]})^{4\alpha/7}(I_{0_{[\frac{mJy}{arcsec^2}]}})^{4/7}(d_{[\text{Mpc}]})^{-4/7}$$

where z is the redshift, d is the source depth and I_0 is its brightness inferred in the radio image at the observational frequency ν_0. The $\xi(\alpha,\nu_1,\nu_2)$ is a constant dependent by the frequency range and the synchrotron spectral index. For the u_{min} calculation we set the filling factor, ϕ, and k equal to 1 while the $\xi(\alpha,\nu_1,\nu_2)$ is taken in the 10 MHz and 100 GHz range with a spectral index of the HT of 0.9. To assume this frequency range implies find the minimum energy density with the classical approach (Chapter 2).

Additionally, we carry out the analysis with the "revised" method, making use of the relations described in Chapter 2. In this approach it is assumed a energy particles cut-off instead of the limits in the frequency range. In our revised analysis we assume $\gamma_{min} = 100$.

The radio surface brightness, I_0, along the tail and the depth of this, d, are obtained from the LOFAR 144 MHz high resolution ($8'' \times 5''$) image managed with the viewer of CASA. The head of the radio galaxy is not included in the pressure profile because it is expected that only the tail is in equilibrium with the environment. I_0 and d are calculated in two different way, explained above.

1. we divide the tail in polygonal regions approximately involving all the tail emission (Figure 6.10a). In each region it is measured a mean value of the surface brightness, given

by the total flux divided for the area from which it is taken. Unknowing the shape of the radio galaxy, we assumed a cylindrical morphology, where the depth d is equal to the longitudinal side of the polygons.

2. we measure the surface brightness from the peaks across the tail (Figure 6.11a). Each surface brightness measurement is spaced by about 1.5-2 pixels. The flux in each pixel is divided for the beam area of the image. The depth of the source d is taken equal to the longitudinal extension of the tail within 3σ contours correspondent to that pixel.

   This method provides more reliable values of the surface brightness compared to the mean value of the method 1) which can underestimate the actual emission of the tail.

In Figure 6.9 it is shown the P_{eq} profile measured with the 2) method assuming the classical equipartition. The profile is obtained along the tail, and it is plotted against the distance from the head. The non-thermal pressure decrease moving away from the head which likely represents the source of acceleration for the particles. In the most external part is detected a clump of higher flux density (and then surface brightness) which provides a slight growth of the pressure in that region. At large distance from the head, the lower surface brightness could be due to the aging of the emitting particles. Further the projection effect are not taken into account in this study. We indeed consider that the entire structure is perpendicular to the line of sight, which can lead to an inaccurate estimation of the source pressure.

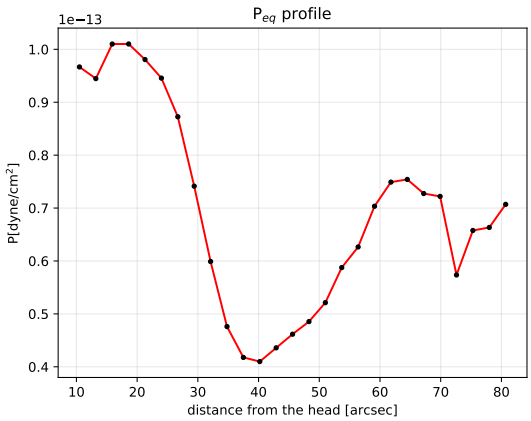

Figure 6.9: The non-thermal pressure profile inferred assuming the equipartition of the energy between particles and magnetic field. In this case it is adopted the classical equipartition approach.

The comparison between the thermal and non-thermal pressure profiles leads to an unbalanced condition. In this case the X-ray pressure results about 10 times higher, by adopting the revised expressions to infer the energy density, and 20-30 times higher assuming a classical approach. This is consistent with what is found by several studies (Feretti et al. 1992, Killeen et al. 1988, Morganti et al. 1988).

The possible explanations of such ratio between the two components pressure can be found in the deviance from the equipartition conditions. In particular higher or lower magnetic field strength would imply a regime where the internal energy (magnetic or particles dominated) is much larger than that in equipartition conditions providing a balance with the external ICM. However this scenario is challenged by the fact that inverse Compton emission in radio galaxies in general agrees with quasi-equipartition conditions and rule out strong departures from this condition (e.g. Hardcastle et al. 2002). Another possibility is the presence of a dominant component of relativistic protons in radio lobes. The poor knowledge about the actual content

of protons in the source can add an important factor of uncertainty on the non-thermal properties estimation, reminding that $P_{eq} \propto (k+1)^{4/7}$ (where k is the ratio between protons and electrons energy). We adopted the ratio between proton and electron equal to 1 but there are not observed evidences to justify this condition. The source can be lie in the gas with a certain angle respect to the line of sight. Feretti et al. 1992 carried out a statistical study of the radio tails confinement in the cluster hot gas and they found that neglecting projection effects results in underestimation of the radio pressure of factors between 5-10. A final argument is the possibility of entrainment of part of the ICM within the radio structure due to fluid instabilities that form at the boundary of radio galaxies and jets. In this cases a significant part of the internal pressure is also contributed by thermal gas (e.g. Croston 2007).

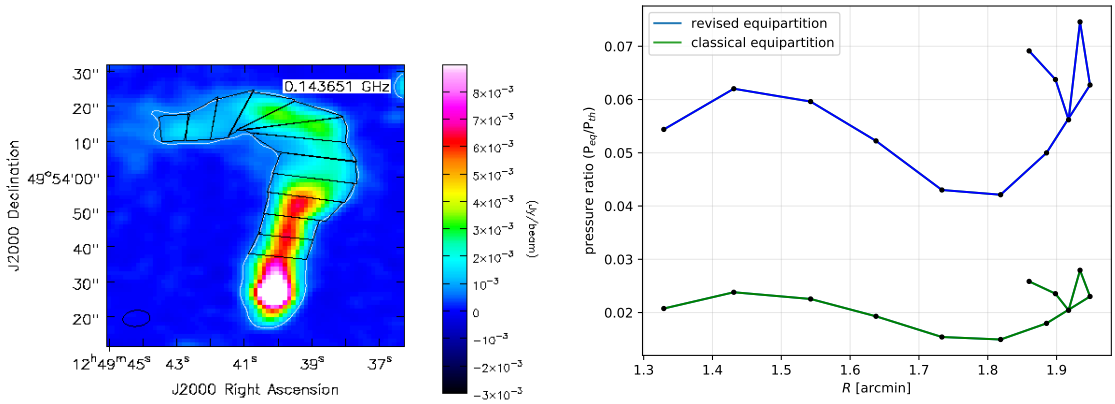

Figure 6.10: *Left*: The tail in Abell 1622 sampled with polygonal regions, They are drawn the 10σ contours level to highlight the tail morphology. *Right*: The ratio between non-thermal and thermal pressure as seen from the distances of the cluster center. They are reported both the cases in which the non-thermal pressure is obtained with the classical and revised equipartition condition.

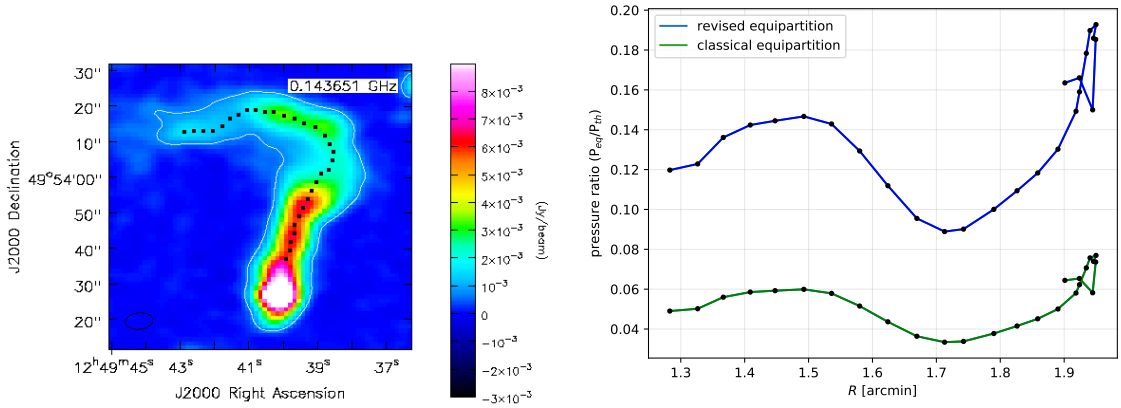

Figure 6.11: *Left*: The surface brightness measurement along the tail in Abell 1622. In this approach the flux density is taken in the pixel and divided for the beam area. *Right*: The ratio between non-thermal and thermal pressure as seen from the distances of the cluster center. They are reported both the cases in which the non-thermal pressure is obtained with the classical and revised equipartition condition.

Chapter 7

Conclusions

RHs in GCs are Mpc-scale diffuse synchrotron sources which prove the presence of non-thermal components, namely relativistic electrons and magnetic fields, spread over the whole cluster volume. The existence of non-thermal components in GCs raises important questions on their origin and on their impact on the microphysics of the ICM and, further, on the evolution of the hosting clusters themselves. The energy involved in clusters mergers is dissipated in shocks and turbulent motions in the ICM. This merger events thus can provide the energy to produce magnetized relativistic plasma and then trigger the observed non-thermal phenomena. To date the widely accepted scenario on the RHs origin is given by the re-acceleration models, in which the RH emission is lighting up by (seed) relativistic particles in GCs and magnetic fields, re-accelerated in merger events (see e.g. Brunetti & Jones 2014 for a review). The connection between the occurrence of RHs and the cluster dynamics is testified by the fact that RHs are statistically found in merging systems.

In order to understand the circumstances of the RH phenomenon in GCs it is thus crucial to constrain the connection of RHs with the X-ray emitting gas. Since the mechanism underlying the microphysics of the particles re-acceleration in merger events is largely unknow yet, significant observational test of the theoretical predictions are provided by a statistical study on RHs. Scaling relations have been found between the X-ray and the radio properties of the RH hosting clusters, suggesting a connection between their thermal and non-thermal components. Moreover, the discovery of a growing number of ultra steep spectrum (USSRH) in less massive GCs supports the predictions of the re-acceleration scenario. These sources are expected to be found in relatively low-mass merging systems as the lower energy involved in these events generate particle distributions with steep spectra. Due to their steep spectrum, the USSRH are more easly found in the low-frequency end of the radio band.

In this prospective the LOFAR interferometer represents a turning point for the study of the clusters in the radio band. This radio telescope allows high resolution and high sensitivity observations of RH in a still poorly explored low-frequency window, providing new and/or more stringent constrains for theoretical models.

The present work is bringing a contribution to the progress in the understanding of RH phenomenon and its link with the dynamics and evolution of relativistic plasma in GCs.

Results

We analyzed three targets from the LoTSS survey at 144 MHz, together with their X-ray and 1.4 GHz band follow-up. The results of analysis can be summarized as follows:

- For Abell 1550 we combined the observation from the VLA and LOFAR interferometers, at 1.4 and 0.144 GHz respectively, in order to provide the spectral behavior of the hosted RH. The integrated radio spectrum between the two frequencies turned out to be $\alpha = 1.6 \pm 0.2$

suggesting that this RH can be classified in the USSRH class. The discovery of RH with spectrum significantly steeper than the typical $\alpha = 1.2-1.3$ support reacceleration models. The RH scaling relations $P_{1.4} - L_X$ and $P_{1.4} - M_{500}$, and the dynamical state (inferred by the X-ray morphological parameters) of the Abell 1550 cluster are in line with the previous studies that prove the link between merging systems and the RH occurrence (Cassano et al. 2010b).

- In RXC J1115.2+5320 we discovered a new RH. Its linear size exceeds the Mpc, and its structure is partially contaminated by the presence of a HT radio galaxy. No other radio data are available for this cluster, and therefore the radio spectrum of the RH could not be determined. The RH scaling relations between the X-ray emitting gas and the non-thermal components of this clusters follow the trend of previous results (Cassano et al. 2013). Also for this cluster we derived the X-ray morphological parameters confirming that this is a dynamically active/merging system as in the great majority of clusters hosting RH (Cassano et al. 2010b).

- In Abell 1622 the morphological parameters of the X-ray emitting gas reveal that the cluster is a dynamically active system. Abell 1622 is the less massive system in our sample, with a mass of about $3.2 \times 10^{14} M_{\odot}$. In the Abell 1622 no evidence of extended emission could be found in the LOFAR observation. On the basis of the sensitivity of the observation studied here, we could set only an upper limit to the RH emission at 144 MHz, which is translated to a radio power at 1.4 GHz assuming a spectral index of $\alpha = 1.3$ (conservative approach). This cluster lies below the correlations. Following the current theoretical picture we propose that the absence of a RH in this cluster (or the possible presence of underluminous cluster scale radio emission) is due to the lower energy budget available to electrons and magnetic fields in these lower mass systems.

- We performed the point-to-point correlation between the X-ray and radio surface brightness for the Abell 1550 and RXC J1115.2+5320 RH. The analysis in the clusters confirms a spatial connection between the non-thermal and thermal emission in GCs hosting RHs. This result is in agreement with previous studies (e.g., Govoni et al. 2001; Feretti et al. 2001).

- In the outskirts of Abell 1622 we found an extended and distorted HT, presumably disturbed by external gas dynamics. We studied the confinement of the tail under the action of the ICM by testing the equilibrium between the internal and external pressure. The X-ray thermal pressure resulted unbalanced by the radio non-thermal one. The same behavior was found by previous studies on HT sources in GCs (e.g., Feretti et al. 1992). This fact can be due to the assumption underlying the equipartition condition, adopted to infer the non-thermal pressure. Furthermore, projection effects play a very relevant role and the 3-D geometry of the radio plasma along the tails is difficult to establish. Finally a significant contribution to the internal pressure can be provided by thermal material accumulated in the radio lobes and jets via entrainment from the surrounding ICM. The thermal material due to instabilities at the boundary of the HT would provide a dominant contribution to the internal pressure.

The USSRH sources represent a crucial support to the turbulent re-acceleration models. After the discovery of the prototype in Abell 521 (Brunetti et al. 2008), the number of USSRHs is continuously growing, thanks to the availability of low frequency surveys, like the one carried out with LOFAR. In this respect, the USSRH found in Abell 1550 is a further step in this

direction. Further radio observations at decimetric wavelenght are necessary to determine the spectrum of RXC j1115.2+5320.

More in general, LOFAR observations reach a sensitivity that is much better than that of other radio telescopes. Our results on Abell 1622 provide a clear example of that. The radio upper limit derived for the RH is a factor 5 deeper than those obtained with VLA or GMRT for clusters at similar redshift. This allows to explore the occurrence of RH in galaxy clusters with masses that are significantly smaller than those explored so far with the potential to carry out clear tests of the theoretical models.

The work carried out for this Thesis is part of a major project, termed HETDEX field, which is a strip of sky, surveyed by the LOFAR telescope and in which several clusters have been investigated. The results are currently analyzed and a paper is planned to appear very soon (van Weeren et al. in preparation). Within this Science Key Project, papers are published for individual clusters in case new discoveries are made. This is the case for Abell 1550, for which a paper is in preparation, based on the results obtained during this Thesis work.

Bibliography

Abolfathi, B. et al. (Apr. 2018). "The Fourteenth Data Release of the Sloan Digital Sky Survey: First Spectroscopic Data from the Extended Baryon Oscillation Spectroscopic Survey and from the Second Phase of the Apache Point Observatory Galactic Evolution Experiment". In: *Astrophysical Journal, Supplement* 235, 42, p. 42.

Akamatsu, Hiroki & Hajime Kawahara (Feb. 2013). "Systematic X-Ray Analysis of Radio Relic Clusters with Suzaku". In: *Publications of the ASJ* 65, 16, p. 16.

Akritas, Michael G. & Matthew A. Bershady (Oct. 1996). "Linear Regression for Astronomical Data with Measurement Errors and Intrinsic Scatter". In: *The Astrophysical Journal* 470, p. 706.

Arnaud, K. A. (1996). "XSPEC: The First Ten Years". In: *Astronomical Data Analysis Software and Systems V*. Ed. by G. H. Jacoby & J. Barnes. Vol. 101. Astronomical Society of the Pacific Conference Series, p. 17.

Atwood, W. B. et al. (June 2009). "The Large Area Telescope on the Fermi Gamma-Ray Space Telescope Mission". In: *The Astrophysical Journal* 697, pp. 1071–1102.

Bagchi, J., F. Durret, G. B. L. Neto & S. Paul (Nov. 2006). "Giant Ringlike Radio Structures Around Galaxy Cluster Abell 3376". In: *Science* 314, pp. 791–794.

Bartelmann, M. (2003). "Strong and Weak Lensing by Galaxy Clusters". In: *Matter and Energy in Clusters of Galaxies, ASP Conference Proceedings, Vol. 301. Held 23-27 April 2002 at National Central University, Chung-Li, Taiwan. Edited by Stuart Bowyer and Chorng-Yuan Hwang. San Francisco: Astronomical Society of the Pacific, 2003. ISBN: 1-58381-149-4, p.255*. Ed. by Stuart Bowyer & Chorng-Yuan Hwang. Vol. 301. Astronomical Society of the Pacific Conference Series, p. 255.

Basu, Kaustuv (Mar. 2012). "A Sunyaev-Zel'dovich take on cluster radio haloes - I. Global scaling and bi-modality using Planck data". In: *Monthly Notices of the Royal Astronomical Society* 421.1, pp. L112–L116.

Baum, S. A. & C. P. O'Dea (June 1991). "Multifrequency VLA observations of PKS 0745 - 191 - The archetypal 'cooling flow' radio source?" In: *Monthly Notices of the Royal Astronomical Society* 250, pp. 737–749.

Bell, A. R. (Jan. 1978). "The acceleration of cosmic rays in shock fronts. I". In: *Monthly Notices of the Royal Astronomical Society* 182, pp. 147–156.

Berezinsky, V. S., P. Blasi & V. S. Ptuskin (Oct. 1997). "Clusters of Galaxies as Storage Room for Cosmic Rays". In: *The Astrophysical Journal* 487, pp. 529–535.

Best, P. N., A. von der Linden, G. Kauffmann, T. M. Heckman & C. R. Kaiser (Aug. 2007). "On the prevalence of radio-loud active galactic nuclei in brightest cluster galaxies: implications for AGN heating of cooling flows". In: *Monthly Notices of the Royal Astronomical Society* 379, pp. 894–908.

Birzan, L. et al. (Aug. 2019). "A massive cluster at z = 0.288 caught in the process of formation: The case of Abell 959". In: *Monthly Notices of the Royal Astronomical Society* 487.4, pp. 4775–4789.

Blasi, P. & S. Colafrancesco (Nov. 1999). "Cosmic rays, radio halos and nonthermal X-ray emission in clusters of galaxies". In: *Astroparticle Physics* 12, pp. 169–183.

Bliton, M., E. Rizza, J. O. Burns, F. N. Owen & M. J. Ledlow (Dec. 1998). "Cluster-subcluster mergers and the formation of narrow-angle tailed radio sources". In: *Monthly Notices of the Royal Astronomical Society* 301, pp. 609–625.

Bohringer, H. et al. (Nov. 2000). "VizieR Online Data Catalog: NORAS galaxy cluster survey. I. (Bohringer+, 2000)". In: *VizieR Online Data Catalog*, J/ApJS/129/435, J/ApJS/129/435.

Böhringer, H. et al. (Oct. 2004). "The ROSAT-ESO Flux Limited X-ray (REFLEX) Galaxy cluster survey. V. The cluster catalogue". In: *Astronomy and Astrophysics* 425, pp. 367–383.

Bonafede, A., M. Brüggen, R. van Weeren, F. Vazza, G. Giovannini, H. Ebeling, A. C. Edge, M. Hoeft & U. Klein (Oct. 2012). "Discovery of radio haloes and double relics in distant MACS galaxy clusters: clues to the efficiency of particle acceleration". In: *Monthly Notices of the Royal Astronomical Society* 426, pp. 40–56.

Bonafede, A., H. T. Intema, M. Brüggen, M. Girardi, M. Nonino, N. Kantharia, R. J. van Weeren & H. J. A. Röttgering (Apr. 2014a). "Evidence for Particle Re-acceleration in the Radio Relic in the Galaxy Cluster PLCKG287.0+32.9". In: *The Astrophysical Journal* 785.1, 1, p. 1.

Bonafede, A. et al. (Sept. 2009). "Revealing the magnetic field in a distant galaxy cluster: discovery of the complex radio emission from MACS J0717.5 +3745". In: *Astronomy and Astrophysics* 503, pp. 707–720.

Bonafede, A. et al. (Oct. 2014b). "A giant radio halo in the cool core cluster CL1821+643." In: *Monthly Notices of the Royal Astronomical Society* 444, pp. L44–L48.

Borgani, S. & A. Kravtsov (Feb. 2011). "Cosmological Simulations of Galaxy Clusters". In: *Advanced Science Letters* 4.2, pp. 204–227.

Borgani, S., G. Murante, V. Springel, A. Diaferio, K. Dolag, L. Moscardini, G. Tormen, L. Tornatore & P. Tozzi (Mar. 2004). "X-ray properties of galaxy clusters and groups from a cosmological hydrodynamical simulation". In: *Monthly Notices of the Royal Astronomical Society* 348.3, pp. 1078–1096.

Boschin, W., M. Girardi, R. Barrena, A. Biviano, L. Feretti & M. Ramella (Mar. 2004). "Internal dynamics of the radio-halo cluster A2219: A multi-wavelength analysis". In: *Astronomy and Astrophysics* 416, pp. 839–851.

Botteon, A., F. Gastaldello, G. Brunetti & D. Dallacasa (July 2016a). "A shock at the radio relic position in Abell 115". In: *Monthly Notices of the Royal Astronomical Society* 460.1, pp. L84–L88.

Botteon, A., F. Gastaldello, G. Brunetti & R. Kale (Dec. 2016b). "A M $\lesssim$ 3 shock in 'El Gordo' cluster and the origin of the radio relic". In: *Monthly Notices of the Royal Astronomical Society* 463, pp. 1534–1542.

Boylan-Kolchin, Michael, Volker Springel, Simon D. M. White, Adrian Jenkins & Gerard Lemson (Sept. 2009). "Resolving cosmic structure formation with the Millennium-II Simulation". In: *Monthly Notices of the Royal Astronomical Society* 398.3, pp. 1150–1164.

Briel, U. G. et al. (Jan. 2001). "A mosaic of the Coma cluster of galaxies with XMM-Newton". In: *Astronomy and Astrophysics* 365, pp. L60–L66.

Brown, S. & L. Rudnick (Mar. 2011). "Diffuse radio emission in/around the Coma cluster: beyond simple accretion". In: *Monthly Notices of the Royal Astronomical Society* 412, pp. 2–12.

Brown, Shea & Lawrence Rudnick (Mar. 2011). "Diffuse radio emission in/around the Coma cluster: beyond simple accretion". In: *Monthly Notices of the Royal Astronomical Society* 412.1, pp. 2–12.

Brunetti, G., P. Blasi, O. Reimer, L. Rudnick, A. Bonafede & S. Brown (Oct. 2012). "Probing the origin of giant radio haloes through radio and γ-ray data: the case of the Coma cluster". In: *Monthly Notices of the Royal Astronomical Society* 426.2, pp. 956–968.

Brunetti, G., R. Cassano, K. Dolag & G. Setti (Nov. 2009). "On the evolution of giant radio halos and their connection with cluster mergers". In: *Astronomy and Astrophysics* 507, pp. 661–669.

Brunetti, G. & Jones (Mar. 2014). "Cosmic Rays in Galaxy Clusters and Their Nonthermal Emission". In: *International Journal of Modern Physics D* 23.4, 1430007-98, pp. 1430007–98.

Brunetti, G., G. Setti & A. Comastri (Sept. 1997). "Inverse Compton X-rays from strong FRII radio-galaxies." In: *Astronomy and Astrophysics* 325, pp. 898–910.

Brunetti, G., G. Setti, L. Feretti & G. Giovannini (Feb. 2001). "Particle injection and reacceleration in clusters of galaxies and the EUV excess: the case of Coma". In: *New Astronomy* 6, pp. 1–15.

Brunetti, G., T. Venturi, D. Dallacasa, R. Cassano, K. Dolag, S. Giacintucci & G. Setti (Nov. 2007). "Cosmic Rays and Radio Halos in Galaxy Clusters: New Constraints from Radio Observations". In: *The Astrophysical Journal Letters* 670, pp. L5–L8.

Brunetti, G., S. Zimmer & F. Zandanel (Dec. 2017). "Relativistic protons in the Coma galaxy cluster: first gamma-ray constraints ever on turbulent reacceleration". In: *Monthly Notices of the Royal Astronomical Society* 472.2, pp. 1506–1525.

Brunetti, G. et al. (Oct. 2008). "A low-frequency radio halo associated with a cluster of galaxies". In: *Nature* 455, pp. 944–947.

Buote, D. A. (May 2001). "On the Origin of Radio Halos in Galaxy Clusters". In: *The Astrophysical Journal Letters* 553, pp. L15–L18.

Buote, David A. & John C. Tsai (Oct. 1995). "Quantifying the Morphologies and Dynamical Evolution of Galaxy Clusters. I. The Method". In: *The Astrophysical Journal* 452, p. 522.

Carlstrom, J. E., G. P. Holder & E. D. Reese (2002). "Cosmology with the Sunyaev-Zel'dovich Effect". In: *Annual Review of Astron and Astrophys* 40, pp. 643–680.

Cassano, R. & G. Brunetti (Mar. 2005). "Cluster mergers and non-thermal phenomena: a statistical magneto-turbulent model". In: *Monthly Notices of the Royal Astronomical Society* 357, pp. 1313–1329.

Cassano, R., G. Brunetti, H. J. A. Röttgering & M. Brüggen (Jan. 2010a). "Unveiling radio halos in galaxy clusters in the LOFAR era". In: *Astronomy and Astrophysics* 509, A68, A68.

Cassano, R., G. Brunetti, G. Setti, F. Govoni & K. Dolag (July 2007). "New scaling relations in cluster radio haloes and the re-acceleration model". In: *Monthly Notices of the Royal Astronomical Society* 378, pp. 1565–1574.

Cassano, R., G. Brunetti, T. Venturi, G. Setti, D. Dallacasa, S. Giacintucci & S. Bardelli (Mar. 2008). "Revised statistics of radio halos and the reacceleration model". In: *Astronomy and Astrophysics* 480, pp. 687–697.

Cassano, R., S. Ettori, G. Brunetti, S. Giacintucci, G. W. Pratt, T. Venturi, R. Kale, K. Dolag & M. Markevitch (Nov. 2013). "Revisiting Scaling Relations for Giant Radio Halos in Galaxy Clusters". In: *The Astrophysical Journal* 777, 141, p. 141.

Cassano, R., S. Ettori, S. Giacintucci, G. Brunetti, M. Markevitch, T. Venturi & M. Gitti (Oct. 2010b). "On the Connection Between Giant Radio Halos and Cluster Mergers". In: *The Astrophysical Journal Letters* 721, pp. L82–L85.

Cavagnolo, Kenneth W., Megan Donahue, G. Mark Voit & Ming Sun (May 2009). "Intracluster Medium Entropy Profiles for a Chandra Archival Sample of Galaxy Clusters". In: *Astrophysical Journal, Supplement* 182.1, pp. 12–32.

Cavaliere, A. & R. Fusco-Femiano (May 1976). "X-rays from hot plasma in clusters of galaxies". In: *Astronomy and Astrophysics* 49, pp. 137–144.

Coles, P. & F. Lucchin (1995). *Cosmology. The origin and evolution of cosmic structure.*

Condon, J. J., W. D. Cotton, E. W. Greisen, Q. F. Yin, R. A. Perley, G. B. Taylor & J. J. Broderick (May 1998). "The NRAO VLA Sky Survey". In: *Astronomical Journal* 115, pp. 1693–1716.

Croston, Judith (Oct. 2007). *Resolving the mystery of FRI particle content.* XMM-Newton Proposal.

Cuciti, V., R. Cassano, G. Brunetti, D. Dallacasa, R. Kale, S. Ettori & T. Venturi (Aug. 2015). "Occurrence of radio halos in galaxy clusters. Insight from a mass-selected sample". In: *Astronomy and Astrophysics* 580, A97, A97.

Dallacasa, D., G. Brunetti, S. Giacintucci, R. Cassano, T. Venturi, G. Macario, N. E. Kassim, W. Lane & G. Setti (July 2009). "Deep 1.4 GHz Follow-up of the Steep Spectrum Radio Halo in A521". In: *The Astrophysical Journal* 699, pp. 1288–1292.

Dalton, Gavin et al. (Sept. 2012). "WEAVE: the next generation wide-field spectroscopy facility for the William Herschel Telescope". In: vol. 8446. Society of Photo-Optical Instrumentation Engineers (SPIE) Conference Series, 84460P.

Davies, R. D. & B. M. Lewis (1973). "Neutral hydrogen in Virgo cluster galaxies." In: *Monthly Notices of the Royal Astronomical Society* 165, pp. 231–244.

de Gasperin, F., H. T. Intema, T. W. Shimwell, G. Brunetti, M. Brüggen, T. A. Enßlin, R. J. van Weeren, A. Bonafede & H. J. A. Röttgering (Oct. 2017). "Gentle reenergization of electrons in merging galaxy clusters". In: *Science Advances* 3.10, e1701634.

de Gasperin, F., R. J. van Weeren, M. Brüggen, F. Vazza, A. Bonafede & H. T. Intema (Nov. 2014). "A new double radio relic in PSZ1 G096.89+24.17 and a radio relic mass-luminosity relation". In: *Monthly Notices of the Royal Astronomical Society* 444, pp. 3130–3138.

de Gasperin, F. et al. (Feb. 2019). "Systematic effects in LOFAR data: A unified calibration strategy". In: *Astronomy and Astrophysics* 622, A5, A5.

De Lucia, G. & J. Blaizot (Feb. 2007). "The hierarchical formation of the brightest cluster galaxies". In: *Monthly Notices of the Royal Astronomical Society* 375, pp. 2–14.

Dennison, B. (Aug. 1980). "Formation of radio halos in clusters of galaxies from cosmic-ray protons". In: *The Astrophysical Journal Letters* 239, pp. L93–L96.

Dolag, K., D. Grasso, V. Springel & I. Tkachev (Jan. 2005). "Constrained simulations of the magnetic field in the local Universe and the propagation of ultrahigh energy cosmic rays". In: *Journal of Cosmology and Astroparticle Physics* 1, 009, p. 009.

Dressler, A. (Mar. 1980). "Galaxy morphology in rich clusters - Implications for the formation and evolution of galaxies". In: *The Astrophysical Journal* 236, pp. 351–365.

Duncan, K. J. et al. (Feb. 2019). "The LOFAR Two-metre Sky Survey. IV. First Data Release: Photometric redshifts and rest-frame magnitudes". In: *Astronomy and Astrophysics* 622, A3, A3.

Ebeling, H., A. C. Edge, S. W. Allen, C. S. Crawford, A. C. Fabian & J. P. Huchra (Oct. 2000). "The ROSAT Brightest Cluster Sample - IV. The extended sample". In: *Monthly Notices of the Royal Astronomical Society* 318, pp. 333–340.

Ebeling, H., A. C. Edge, H. Bohringer, S. W. Allen, C. S. Crawford, A. C. Fabian, W. Voges & J. P. Huchra (Dec. 1998). "The ROSAT Brightest Cluster Sample - I. The compilation of the sample and the cluster log N-log S distribution". In: *Monthly Notices of the Royal Astronomical Society* 301, pp. 881–914.

Enßlin, T. A. & H. Röttgering (Dec. 2002). "The radio luminosity function of cluster radio halos". In: *Astronomy and Astrophysics* 396, pp. 83–89.

Ensslin, Torsten A., Peter L. Biermann, Ulrich Klein & Sven Kohle (Apr. 1998). "Cluster radio relics as a tracer of shock waves of the large-scale structure formation". In: *Astronomy and Astrophysics* 332, pp. 395–409.

Fabian, A. C. (1994). "Cooling Flows in Clusters of Galaxies". In: *Annual Review of Astron and Astrophys* 32, pp. 277–318.

Fanaroff, B. L. & J. M. Riley (May 1974). "The morphology of extragalactic radio sources of high and low luminosity". In: *Monthly Notices of the Royal Astronomical Society* 167, 31P–36P.

Feretti, L. (2003). "Radio Observations of Clusters of Galaxies". In: *Matter and Energy in Clusters of Galaxies*. Ed. by S. Bowyer & C.-Y. Hwang. Vol. 301. Astronomical Society of the Pacific Conference Series, p. 143.

Feretti, L., G. Brunetti, G. Giovannini, F. Govoni & G. Setti (2000). "Non Thermal Emission from Galaxy Clusters: Radio Halos". In: *Constructing the Universe with Clusters of Galaxies*.

Feretti, L., R. Fusco-Femiano, G. Giovannini & F. Govoni (July 2001). "The giant radio halo in Abell 2163". In: *Astronomy and Astrophysics* 373, pp. 106–112.

Feretti, L., G. Giovannini, F. Govoni & M. Murgia (May 2012). "Clusters of galaxies: observational properties of the diffuse radio emission". In: *Astronomy and Astrophysics Reviews* 20, 54, p. 54.

Feretti, L., G. C. Perola & R. Fanti (Nov. 1992). "Tailed radio sources as probes of the intergalactic medium pressure." In: *Astronomy and Astrophysics* 265, pp. 9–18.

Ferrari, C., S. Maurogordato, A. Cappi & C. Benoist (Mar. 2003). "Multiple merging events in Abell 521". In: *Astronomy and Astrophysics* 399, pp. 813–828.

Gabici, S. & P. Blasi (Feb. 2003). "Nonthermal Radiation from Clusters of Galaxies: The Role of Merger Shocks in Particle Acceleration". In: *The Astrophysical Journal* 583, pp. 695–705.

Giacintucci, S., M. Markevitch, R. Cassano, T. Venturi, T. E. Clarke & G. Brunetti (June 2017). "Occurrence of Radio Minihalos in a Mass-limited Sample of Galaxy Clusters". In: *The Astrophysical Journal* 841.2, 71, p. 71.

Giovannini, G., A. Bonafede, L. Feretti, F. Govoni, M. Murgia, F. Ferrari & G. Monti (Dec. 2009). "Radio halos in nearby (z < 0.4) clusters of galaxies". In: *Astronomy and Astrophysics* 507.3, pp. 1257–1270.

Giovannini, G., L. Feretti, T. Venturi, K.-T. Kim & P. P. Kronberg (Apr. 1993). "The halo radio source Coma C and the origin of halo sources". In: *The Astrophysical Journal* 406, pp. 399–406.

Giovannini, G., M. Tordi & L. Feretti (Mar. 1999). "Radio halo and relic candidates from the NRAO VLA Sky Survey". In: *New Astronomy* 4.2, pp. 141–155.

Girardi, M., D. Fadda, G. Giuricin, F. Mardirossian, M. Mezzetti & A. Biviano (Jan. 1996). "Velocity Dispersions and X-Ray Temperatures of Galaxy Clusters". In: *The Astrophysical Journal* 457, p. 61.

Girardi, M. et al. (Mar. 2016). "A multiwavelength view of the galaxy cluster Abell 523 and its peculiar diffuse radio source". In: *Monthly Notices of the Royal Astronomical Society* 456, pp. 2829–2847.

Gitti, M., F. Brighenti & B. R. McNamara (2012). "Evidence for AGN Feedback in Galaxy Clusters and Groups". In: *Advances in Astronomy* 2012, 950641, p. 950641.

Gitti, M., G. Brunetti & G. Setti (May 2002). "Modeling the interaction between ICM and relativistic plasma in cooling flows: The case of the Perseus cluster". In: *Astronomy and Astrophysics* 386, pp. 456–463.

Govoni, F., T. A. Enßlin, L. Feretti & G. Giovannini (Apr. 2001). "A comparison of radio and X-ray morphologies of four clusters of galaxies containing radio halos". In: *Astronomy and Astrophysics* 369, pp. 441–449.

Govoni, F. & L. Feretti (Jan. 2004). "Magnetic Fields in Clusters of Galaxies". In: *International Journal of Modern Physics D* 13.8, pp. 1549–1594.

Govoni, F., C. Ferrari, L. Feretti, V. Vacca, M. Murgia, G. Giovannini, R. Perley & C. Benoist (Sept. 2012). "Detection of diffuse radio emission in the galaxy clusters A800, A910, A1550, and CL 1446+26". In: *Astronomy and Astrophysics* 545, A74, A74.

Govoni, F., M. Murgia, L. Feretti, G. Giovannini, D. Dallacasa & G. B. Taylor (Jan. 2005). "A2255: The first detection of filamentary polarized emission in a radio halo". In: *Astronomy and Astrophysics* 430, pp. L5–L8.

Hardcastle, M. J., M. Birkinshaw, R. A. Cameron, D. E. Harris, L. W. Looney & D. M. Worrall (Dec. 2002). "Magnetic Field Strengths in the Hot Spots and Lobes of Three Powerful Fanaroff-Riley Type II Radio Sources". In: *The Astrophysical Journal* 581.2, pp. 948–973.

Hasselfield, Matthew et al. (July 2013). "The Atacama Cosmology Telescope: Sunyaev-Zel'dovich selected galaxy clusters at 148 GHz from three seasons of data". In: *Journal of Cosmology and Astroparticle Physics* 2013.7, 008, p. 008.

Heald, G. H. et al. (Oct. 2015). "The LOFAR Multifrequency Snapshot Sky Survey (MSSS). I. Survey description and first results". In: *Astronomy and Astrophysics* 582, A123, A123.

Hill, G. J. et al. (Oct. 2008). "The Hobby-Eberly Telescope Dark Energy Experiment (HETDEX): Description and Early Pilot Survey Results". In: *Panoramic Views of Galaxy Formation and Evolution*. Ed. by T. Kodama, T. Yamada & K. Aoki. Vol. 399. Astronomical Society of the Pacific Conference Series, p. 115.

Hitomi Collaboration et al. (July 2016). "The quiescent intracluster medium in the core of the Perseus cluster". In: *Nature* 535, pp. 117–121.

Hoang, D. N. et al. (Aug. 2018). "Radio observations of the double-relic galaxy cluster Abell 1240". In: *Monthly Notices of the Royal Astronomical Society* 478.2, pp. 2218–2233.

Ignesti, Alessandro, Gianfranco Brunetti, Myriam Gitti & Simona Giacintucci (July 2018). "Thermal and non-thermal connection in radio mini-halos". In: *arXiv e-prints*, arXiv:1807.11579, arXiv:1807.11579.

Intema, H. T., P. Jagannathan, K. P. Mooley & D. A. Frail (Feb. 2017). "The GMRT 150 MHz all-sky radio survey. First alternative data release TGSS ADR1". In: *Astronomy and Astrophysics* 598, A78, A78.

Jaffe, W. J. (Feb. 1977). "Origin and transport of electrons in the halo radio source in the Coma cluster". In: *The Astrophysical Journal* 212, pp. 1–7.

Jeltema, T. E. & S. Profumo (Feb. 2011). "Implications of Fermi Observations For Hadronic Models of Radio Halos in Clusters of Galaxies". In: *The Astrophysical Journal* 728, 53, p. 53.

Jeltema, Tesla E., Claude R. Canizares, Mark W. Bautz & David A. Buote (May 2005). "The Evolution of Structure in X-Ray Clusters of Galaxies". In: *The Astrophysical Journal* 624.2, pp. 606–629.

Jones, C. & W. Forman (Jan. 1984). "The structure of clusters of galaxies observed with Einstein". In: *The Astrophysical Journal* 276, pp. 38–55.

Kaiser, N. (Sept. 1986). "Evolution and clustering of rich clusters". In: *Monthly Notices of the Royal Astronomical Society* 222, pp. 323–345.

Kale, R. (Apr. 2013). "Radio observations of Planck clusters". In: *Astronomische Nachrichten* 334.4-5, p. 338.

Kang, Hyesung, Dongsu Ryu & T. W. Jones (Sept. 2012). "Diffusive Shock Acceleration Simulations of Radio Relics". In: *The Astrophysical Journal* 756.1, 97, p. 97.

Killeen, N. E. B., G. V. Bicknell & R. D. Ekers (Feb. 1988). "The Thermally Confined Radio Source in NGC 1399". In: *The Astrophysical Journal* 325, p. 180.

King, I. (Oct. 1962). "The structure of star clusters. I. an empirical density law". In: *Astronomical Journal* 67, p. 471.

Krymskii, G. F. (June 1977). "A regular mechanism for the acceleration of charged particles on the front of a shock wave". In: *Soviet Physics Doklady* 22, p. 327.

Landau, L. D. & E. M. Lifshit's (1959). *Theory of elasticity.*

Lane, W. M., W. D. Cotton, J. F. Helmboldt & N. E. Kassim (Jan. 2012). "VLSS redux: Software improvements applied to the Very Large Array Low-Frequency Sky Survey". In: *Radio Science* 47.3, RS0K04, RS0K04.

Large, M. I., D. S. Mathewson & C. G. T. Haslam (June 1959). "A High-Resolution Survey of the Coma Cluster of Galaxies at 408 Mc./s." In: *Nature* 183, pp. 1663–1664.

Lin, Yen-Ting & Joseph J. Mohr (Dec. 2004). "K-band Properties of Galaxy Clusters and Groups: Brightest Cluster Galaxies and Intracluster Light". In: *The Astrophysical Journal* 617.2, pp. 879–895.

Lindner, Robert R. et al. (May 2014). "The Radio Relics and Halo of El Gordo, a Massive z = 0.870 Cluster Merger". In: *The Astrophysical Journal* 786.1, 49, p. 49.

Lovisari, L., T. H. Reiprich & G. Schellenberger (Jan. 2015). "Scaling properties of a complete X-ray selected galaxy group sample". In: *Astronomy and Astrophysics* 573, A118, A118.

Macario, G., T. Venturi, G. Brunetti, D. Dallacasa, S. Giacintucci, R. Cassano, S. Bardelli & R. Athreya (July 2010). "The very steep spectrum radio halo in Abell 697". In: *Astronomy and Astrophysics* 517, A43, A43.

Markevitch, M., F. Govoni, G. Brunetti & D. Jerius (July 2005). "Bow Shock and Radio Halo in the Merging Cluster A520". In: *The Astrophysical Journal* 627.2, pp. 733–738.

Markevitch, M., C. L. Sarazin & A. Vikhlinin (Aug. 1999). "Physics of the Merging Clusters Cygnus A, A3667, and A2065". In: *The Astrophysical Journal* 521.2, pp. 526–530.

Markevitch, M. & A. Vikhlinin (May 2007). "Shocks and cold fronts in galaxy clusters". In: *Physics Reports* 443.1, pp. 1–53.

Maughan, B. J., C. Jones, W. Forman & L. Van Speybroeck (Jan. 2008). "Images, Structural Properties, and Metal Abundances of Galaxy Clusters Observed with Chandra ACIS-I at 0.1 < z < 1.3". In: *Astrophysical Journal, Supplement* 174.1, pp. 117–135.

Mazzotta, P. & S. Giacintucci (Mar. 2008). "Do Radio Core-Halos and Cold Fronts in Non-Major-Merging Clusters Originate from the Same Gas Sloshing?" In: *The Astrophysical Journal Letters* 675, p. L9.

McNamara, B. R. & P. E. J. Nulsen (Sept. 2007). "Heating Hot Atmospheres with Active Galactic Nuclei". In: *Annual Review of Astron and Astrophys* 45.1, pp. 117–175.

Melrose, D. B. (1980). *Plasma astrophysics: Nonthermal processes in diffuse magnetized plasmas. Volume 1 - The emission, absorption and transfer of waves in plasmas.*

Mernier, F. et al. (Dec. 2018). "Enrichment of the Hot Intracluster Medium: Observations". In: *Space Science Reviews* 214.8, 129, p. 129.

Mihos, J. C. (2004). "Interactions and Mergers of Cluster Galaxies". In: *Clusters of Galaxies: Probes of Cosmological Structure and Galaxy Evolution*, p. 277.

Miley, G. (1980). "The structure of extended extragalactic radio sources". In: *Annual Review of Astron and Astrophys* 18, pp. 165–218.

Miley, G. K., G. C. Perola, P. C. van der Kruit & H. van der Laan (June 1972). "Active Galaxies with Radio Trails in Clusters". In: *Nature* 237.5353, pp. 269–272.

Miniati, F. (Feb. 2014). "The Matryoshka Run: A Eulerian Refinement Strategy to Study the Statistics of Turbulence in Virialized Cosmic Structures". In: *The Astrophysical Journal* 782.1, 21, p. 21.

Mittal, R., A. Hicks, T. H. Reiprich & V. Jaritz (Aug. 2011). "The L_X - T_{vir} relation in galaxy clusters: effects of radiative cooling and AGN heating". In: *Astronomy and Astrophysics* 532, A133, A133.

Mohan, Niruj & David Rafferty (Feb. 2015). *PyBDSF: Python Blob Detection and Source Finder.*

Mohapatra, Rajsekhar & Prateek Sharma (Apr. 2019). "Turbulence in the intracluster medium: simulations, observables, and thermodynamics". In: *Monthly Notices of the Royal Astronomical Society* 484.4, pp. 4881–4896.

Mohr, Joseph J., Daniel G. Fabricant & Margaret J. Geller (Aug. 1993). "An X-Ray Method for Detecting Substructure in Galaxy Clusters: Application to Perseus, A2256, Centaurus, Coma, and Sersic 40/6". In: *The Astrophysical Journal* 413, p. 492.

Moore, Ben, Neal Katz, George Lake, Alan Dressler & Augustus Oemler (Feb. 1996). "Galaxy harassment and the evolution of clusters of galaxies". In: *Nature* 379.6566, pp. 613–616.

Morganti, R., R. Fanti, I. M. Gioia, D. E. Harris, P. Parma & H. de Ruiter (Jan. 1988). "Low luminosity radio galaxies : effects of gaseous environment." In: *Astronomy and Astrophysics* 189, pp. 11–26.

Murgia, M., F. Govoni, M. Markevitch, L. Feretti, G. Giovannini, G. B. Taylor & E. Carretti (June 2009). "Comparative analysis of the diffuse radio emission in the galaxy clusters A1835, A2029, and Ophiuchus". In: *Astronomy and Astrophysics* 499, pp. 679–695.

Navarro, J. F., C. S. Frenk & S. D. M. White (Dec. 1997). "A Universal Density Profile from Hierarchical Clustering". In: *The Astrophysical Journal* 490, pp. 493–508.

O'Dea, C. P. et al. (July 2008). "An Infrared Survey of Brightest Cluster Galaxies. II. Why are Some Brightest Cluster Galaxies Forming Stars?" In: *The Astrophysical Journal* 681, pp. 1035–1045.

Oemler, A. (Apr. 1973). "The cluster of galaxies Abell 2670." In: *The Astrophysical Journal* 180.

Offringa, A. R., J. J. van de Gronde & J. B. T. M. Roerdink (Mar. 2012). "A morphological algorithm for improving radio-frequency interference detection". In: *Astronomy and Astrophysics* 539, A95, A95.

Offringa, A. R. et al. (Oct. 2014). "WSCLEAN: an implementation of a fast, generic wide-field imager for radio astronomy". In: *Monthly Notices of the Royal Astronomical Society* 444.1, pp. 606–619.

Spatial tessellations : concepts and applications of voronoi diagrams (Jan. 2000).

Ostriker, J. P. & M. A. Hausman (Nov. 1977). "Cannibalism among the galaxies - Dynamically produced evolution of cluster luminosity functions". In: *The Astrophysical Journal Letters* 217, pp. L125–L129.

Owen, F. N., C. P. O'Dea, M. Inoue & J. A. Eilek (July 1985). "VLA observations of the multiple jet galaxy 3C 75". In: *The Astrophysical Journal Letters* 294, pp. L85–L88.

Pacholczyk, A. G. (1970). *Radio astrophysics. Nonthermal processes in galactic and extragalactic sources.*

Penzias, A. A. & R. W. Wilson (July 1965). "A Measurement of Excess Antenna Temperature at 4080 Mc/s." In: *The Astrophysical Journal* 142, pp. 419–421.

Peterson, J. R. & A. C. Fabian (Apr. 2006). "X-ray spectroscopy of cooling clusters". In: *Physics Reports* 427.1, pp. 1–39.

Petrosian, V. (Aug. 2001). "On the Nonthermal Emission and Acceleration of Electrons in Coma and Other Clusters of Galaxies". In: *The Astrophysical Journal* 557, pp. 560–572.

Pfrommer, C. & T. A. Enßlin (Dec. 2004). "The Quest for Cosmic Ray Protons in Galaxy Clusters". In: *Journal of Korean Astronomical Society* 37, pp. 455–460.

Pfrommer, C., V. Springel, T. A. Enßlin & M. Jubelgas (Mar. 2006). "Detecting shock waves in cosmological smoothed particle hydrodynamics simulations". In: *Monthly Notices of the Royal Astronomical Society* 367, pp. 113–131.

Planck Collaboration et al. (Dec. 2011). "Planck early results. XI. Calibration of the local galaxy cluster Sunyaev-Zeldovich scaling relations". In: *Astronomy and Astrophysics* 536, A11, A11.

Planck Collaboration et al. (Nov. 2014). “Planck 2013 results. XXIX. The Planck catalogue of Sunyaev-Zeldovich sources”. In: *Astronomy and Astrophysics* 571, A29, A29.

Planck Collaboration et al. (Sept. 2016). “Planck 2015 results. XXVII. The second Planck catalogue of Sunyaev-Zeldovich sources”. In: *Astronomy and Astrophysics* 594, A27, A27.

Poole, Gregory B., Mark A. Fardal, Arif Babul, Ian G. McCarthy, Thomas Quinn & James Wadsley (Dec. 2006). “The impact of mergers on relaxed X-ray clusters - I. Dynamical evolution and emergent transient structures”. In: *Monthly Notices of the Royal Astronomical Society* 373.3, pp. 881–905.

Rajpurohit, K. et al. (Jan. 2018). “Deep VLA Observations of the Cluster 1RXS J0603.3+4214 in the Frequency Range of 1-2 GHz”. In: *The Astrophysical Journal* 852, 65, p. 65.

Reichardt, C. L. et al. (Feb. 2013). “Galaxy Clusters Discovered via the Sunyaev-Zel’dovich Effect in the First 720 Square Degrees of the South Pole Telescope Survey”. In: *The Astrophysical Journal* 763.2, 127, p. 127.

Rengelink, R. B., Y. Tang, A. G. de Bruyn, G. K. Miley, M. N. Bremer, H. J. A. Roettgering & M. A. R. Bremer (Aug. 1997). “The Westerbork Northern Sky Survey (WENSS), I. A 570 square degree Mini-Survey around the North Ecliptic Pole”. In: *Astronomy and Astrophysics, Supplement* 124, pp. 259–280.

Roettiger, K., J. O. Burns & J. M. Stone (June 1999). “A Cluster Merger and the Origin of the Extended Radio Emission in Abell 3667”. In: *The Astrophysical Journal* 518.2, pp. 603–612.

Roettiger, K., C. Loken & J. O. Burns (Apr. 1997). “Numerical Simulations of Merging Clusters of Galaxies”. In: *Astrophysical Journal, Supplement* 109, pp. 307–332.

Rottgering, H. J. A., M. H. Wieringa, R. W. Hunstead & R. D. Ekers (Sept. 1997). “The extended radio emission in the luminous X-ray cluster A3667”. In: *Monthly Notices of the Royal Astronomical Society* 290, pp. 577–584.

Rybicki, G. B. & A. P. Lightman (June 1986). *Radiative Processes in Astrophysics*, p. 400.

Ryu, D., H. Kang, E. Hallman & T. W. Jones (Aug. 2003). “Cosmological Shock Waves and Their Role in the Large-Scale Structure of the Universe”. In: *The Astrophysical Journal* 593.2, pp. 599–610.

Sakelliou, Irini & Michael R. Merrifield (Jan. 2000). “The origin of wide-angle tailed radio galaxies”. In: *Monthly Notices of the Royal Astronomical Society* 311.3, pp. 649–656.

Santos, J. S., P. Rosati, P. Tozzi, H. Böhringer, S. Ettori & A. Bignamini (2008). “Cool Core Clusters at Redshift z > 0.7”. In: *Panoramic Views of Galaxy Formation and Evolution ASP Conference Series, Vol. 399, proceedings of the conference held 11-16 December, 2007, at Shonan Village Center, Hayama, Japan. Edited by Tadayuki Kodama, Toru Yamada, and Kentaro Aoki. San Francisco: Astronomical Society of the Pacific, 2008., p.375*. Ed. by T. Kodama, T. Yamada & K. Aoki. Vol. 399. Astronomical Society of the Pacific Conference Series, p. 375.

Sarazin, C. L. (Jan. 1986). “X-ray emission from clusters of galaxies”. In: *Rev. Mod. Phys.* 58 (1), pp. 1–115.

Sarazin, C. L. (Aug. 1999). “The Energy Spectrum of Primary Cosmic-Ray Electrons in Clusters of Galaxies and Inverse Compton Emission”. In: *The Astrophysical Journal* 520.2, pp. 529–547.

Sarazin, C. L. (June 2002). “The Physics of Cluster Mergers”. In: *Merging Processes in Galaxy Clusters*. Ed. by L. Feretti, I. M. Gioia & G. Giovannini. Vol. 272. Astrophysics and Space Science Library, pp. 1–38.

Savini, F. et al. (Aug. 2018). “First evidence of diffuse ultra-steep-spectrum radio emission surrounding the cool core of a cluster”. In: *Monthly Notices of the Royal Astronomical Society* 478.2, pp. 2234–2242.

Scaife, Anna M. M. & George H. Heald (June 2012). "A broad-band flux scale for low-frequency radio telescopes". In: *Monthly Notices of the Royal Astronomical Society* 423.1, pp. L30–L34.
Schechter, P. (Jan. 1976). "An analytic expression for the luminosity function for galaxies." In: *The Astrophysical Journal* 203, pp. 297–306.
Shimwell, T. W. et al. (June 2016). "A plethora of diffuse steep spectrum radio sources in Abell 2034 revealed by LOFAR". In: *Monthly Notices of the Royal Astronomical Society* 459.1, pp. 277–290.
Shimwell, T. W. et al. (Feb. 2017). "The LOFAR Two-metre Sky Survey. I. Survey description and preliminary data release". In: *Astronomy and Astrophysics* 598, A104, A104.
Shimwell, T. W. et al. (Feb. 2019). "The LOFAR Two-metre Sky Survey. II. First data release". In: *Astronomy and Astrophysics* 622, A1, A1.
Smith, D. J. B. et al. (Dec. 2016). "The WEAVE-LOFAR Survey". In: *SF2A-2016: Proceedings of the Annual meeting of the French Society of Astronomy and Astrophysics*, pp. 271–280.
Springel, Volker et al. (June 2005). "Simulations of the formation, evolution and clustering of galaxies and quasars". In: *Nature* 435.7042, pp. 629–636.
Sunyaev, R. A. & Y. B. Zeldovich (Nov. 1972). "The Observations of Relic Radiation as a Test of the Nature of X-Ray Radiation from the Clusters of Galaxies". In: *Comments on Astrophysics and Space Physics* 4, p. 173.
Sutherland, R. S. & M. A. Dopita (Sept. 1993). "Cooling functions for low-density astrophysical plasmas". In: *Astrophysical Journal, Supplement* 88, pp. 253–327.
Taylor, G. B., N. E. Gugliucci, A. C. Fabian, J. S. Sanders, G. Gentile & S. W. Allen (June 2006). "Magnetic fields in the centre of the Perseus cluster". In: *Monthly Notices of the Royal Astronomical Society* 368, pp. 1500–1506.
Thierbach, M., U. Klein & R. Wielebinski (Jan. 2003). "The diffuse radio emission from the Coma cluster at 2.675 GHz and 4.85 GHz". In: *Astronomy and Astrophysics* 397, pp. 53–61.
van Haarlem, M. P. et al. (Aug. 2013). "LOFAR: The LOw-Frequency ARray". In: *Astronomy and Astrophysics* 556, A2, A2.
van Weeren, R. J., F. de Gasperin, H. Akamatsu, M. Brüggen, L. Feretti, H. Kang, A. Stroe & F. Zandanel (Feb. 2019). "Diffuse Radio Emission from Galaxy Clusters". In: *Space Science Reviews* 215.1, 16, p. 16.
van Weeren, R. J., Huub J. A. Röttgering, Marcus Brüggen & Matthias Hoeft (Oct. 2010). "Particle Acceleration on Megaparsec Scales in a Merging Galaxy Cluster". In: *Science* 330.6002, p. 347.
van Weeren, R. J. et al. (Mar. 2016). "LOFAR Facet Calibration". In: *Astrophysical Journal, Supplement* 223.1, 2, p. 2.
van Weeren, R. J. et al. (Jan. 2017). "The case for electron re-acceleration at galaxy cluster shocks". In: *Nature Astronomy* 1, 0005, p. 0005.
Vazza, F., M. Angelinelli, T. W. Jones, D. Eckert, M. Brüggen, G. Brunetti & C. Gheller (Nov. 2018). "The turbulent pressure support in galaxy clusters revisited". In: *Monthly Notices of the Royal Astronomical Society* 481.1, pp. L120–L124.
Vazza, F., G. Brunetti & C. Gheller (May 2009). "Shock waves in Eulerian cosmological simulations: main properties and acceleration of cosmic rays". In: *Monthly Notices of the Royal Astronomical Society* 395, pp. 1333–1354.
Vazza, F., G. Tormen, R. Cassano, G. Brunetti & K. Dolag (June 2006). "Turbulent velocity fields in smoothed particle hydrodymanics simulated galaxy clusters: scaling laws for the turbulent energy". In: *Monthly Notices of the Royal Astronomical Society* 369, pp. L14–L18.
Venturi, T., S. Giacintucci, R. Cassano, G. Brunetti, D. Dallacasa, G. Macario, G. Setti, S. Bardelli & R. Athreya (Sept. 2009). "The GMRT Radio Halo Survey and Low Frequency

Follow–up". In: *The Low-Frequency Radio Universe*. Ed. by D. J. Saikia, D. A. Green, Y. Gupta & T. Venturi. Vol. 407. Astronomical Society of the Pacific Conference Series, p. 232.

Venturi, T., S. Giacintucci, D. Dallacasa, R. Cassano, G. Brunetti, S. Bardelli & G. Setti (June 2008). "GMRT radio halo survey in galaxy clusters at z = 0.2-0.4. II. The eBCS clusters and analysis of the complete sample". In: *Astronomy and Astrophysics* 484, pp. 327–340.

Venturi, T., S. Giacintucci, D. Dallacasa, R. Cassano, G. Brunetti, G. Macario & R. Athreya (Mar. 2013). "Low frequency follow up of radio haloes and relics in the GMRT Radio Halo Cluster Survey". In: *Astronomy and Astrophysics* 551, A24, A24.

Venturi, T. et al. (July 2017). "The two-component giant radio halo in the galaxy cluster Abell 2142". In: *Astronomy and Astrophysics* 603, A125, A125.

Vikhlinin, A., W. Forman & C. Jones (Nov. 1999). "Outer Regions of the Cluster Gaseous Atmospheres". In: *The Astrophysical Journal* 525, pp. 47–57.

Vogelsberger, Mark, Shy Genel, Volker Springel, Paul Torrey, Debora Sijacki, Dandan Xu, Greg Snyder, Dylan Nelson & Lars Hernquist (Oct. 2014). "Introducing the Illustris Project: simulating the coevolution of dark and visible matter in the Universe". In: *Monthly Notices of the Royal Astronomical Society* 444.2, pp. 1518–1547.

Wayth, R. B. et al. (June 2015). "GLEAM: The GaLactic and Extragalactic All-Sky MWA Survey". In: *Publications of the Astron. Soc. of Australia* 32, e025, e025.

Wilber, A. et al. (Jan. 2018). "LOFAR discovery of an ultra-steep radio halo and giant head-tail radio galaxy in Abell 1132". In: *Monthly Notices of the Royal Astronomical Society* 473.3, pp. 3536–3546.

Williams, W. L. et al. (Feb. 2019). "The LOFAR Two-metre Sky Survey. III. First data release: Optical/infrared identifications and value-added catalogue". In: *Astronomy and Astrophysics* 622, A2, A2.

Willingale, R., R. L. C. Starling, A. P. Beardmore, N. R. Tanvir & P. T. O'Brien (May 2013). "Calibration of X-ray absorption in our Galaxy". In: *Monthly Notices of the Royal Astronomical Society* 431, pp. 394–404.

Wilman, R. J. et al. (Aug. 2008). "A semi-empirical simulation of the extragalactic radio continuum sky for next generation radio telescopes". In: *Monthly Notices of the Royal Astronomical Society* 388.3, pp. 1335–1348.

York, Donald G. et al. (Sept. 2000). "The Sloan Digital Sky Survey: Technical Summary". In: *Astronomical Journal* 120.3, pp. 1579–1587.

Zandanel, Fabio & Shin'ichiro Ando (May 2014). "Constraints on diffuse gamma-ray emission from structure formation processes in the Coma cluster". In: *Monthly Notices of the Royal Astronomical Society* 440.1, pp. 663–671.

ZuHone, J. A., M. Markevitch, G. Brunetti & S. Giacintucci (Jan. 2013). "Turbulence and Radio Mini-halos in the Sloshing Cores of Galaxy Clusters". In: *The Astrophysical Journal* 762.2, 78, p. 78.

Zwicky, F. (Oct. 1937). "On the Masses of Nebulae and of Clusters of Nebulae". In: *The Astrophysical Journal* 86, p. 217.